INVESTIGATION ON COMBUSTION IN POROUS INERT BURNERS USING GASEOUS AND LIQUID FUELS

Snehasish Panigrahy
Roll No: 146103036

DEPARTMENT OF MECHANICAL ENGINEERING
INDIAN INSTITUTE OF TECHNOLOGY GUWAHATI
July, 2018

INVESTIGATION ON COMBUSTION IN POROUS INERT BURNERS USING GASEOUS AND LIQUID FUELS

A Thesis Submitted

in Partial Fulfillment of the Requirements

for the Degree of

Doctor of Philosophy

by

Snehasish Panigrahy

to the

DEPARTMENT OF MECHANICAL ENGINEERING

INDIAN INSTITUTE OF TECHNOLOGY GUWAHATI

July, 2018

C E R T I F I C A T E

It is certified that the work contained in the thesis entitled **Investigation on Combustion in Porous Inert Burners Using Gaseous and Liquid Fuels**, by Snehasish Panigrahy, a student in the Department of Mechanical Engineering, Indian Institute of Technology Guwahati, India, for the award of the degree of the Doctor of Philosophy has been carried out under my supervision, and that this work has not been submitted elsewhere for a degree.

Late Dr. Subhash C. Mishra
Professor
Department of Mechanical Engineering
Indian Institute of Technology Guwahati
Guwahati, Assam-781039, India
July, 2018

Dr. Gautam Biswas
Professor
Department of Mechanical Engineering
Indian Institute of Technology Guwahati
Guwahati, Assam-781039, India
July, 2018

To

The memories of my supervisor Late Prof. Subhash C. Mishra (1964-2017)

Acknowledgments

It is a wonderful opportunity to display my acknowledgment of gratitude to many prominent personalities of my life, without whom this thesis would not have been possible.

This dissertation is dedicated to my supervisor, Late Professor Subhash C. Mishra. I sorely missed him, who had been an immense support at the beginning of my thesis and introduced me to scientific research of high quality. I could not ask for a better role model. I would like to express my indebtedness to Professor Gautam Biswas who kindly agreed to act as my supervisor after the unfortunate demise of Prof. Mishra. Despite his extreme responsibilities as the Director of IIT Guwahati, he always offered unconditional support and showed a great confidence in me. He provided me the moral support and freedom I needed to finish this thesis. It has been a privilege to learn from such great professors.

I would like to give my sincere gratitude and appreciation to my doctoral committee members, Prof. Manmohan Pandey, Prof. Dipankar Bandopadhyay and Dr. Pranab Kumar Mondal for their valuable time and effort in reviewing my works. I am grateful to the Department of Mechanical Engineering at IIT Guwahati, especially my sincere thanks go to Dr. Vinayak Kulkarni, Prof. Uday S. Dixit and Prof. Amaresh Dalal for their invaluable advice and encouragement. I also want to acknowledge Prof. Pinakeswar Mahanta for his generous support and helping me in the DME burner setup.

Successful completion of this thesis would not have been possible without the backing and support of my good friends, Saurabh, Rahul, Niraj, and Rupesh. I really appreciate the technical assistance of Lav Kumar and Gyan Sagar in conducting the experiments. Special mention should go to Shuvayan, Sumit, and Siddesh in making my Ph.D. experience more enjoyable. I wish them all continuous success in their future careers.

Finally and most importantly, I owe my loving thanks to my parents, and my brother, for encouraging me and letting me to be as ambitious as I wanted. Without their unconditional love and understanding, I would not have been able to complete this journey. Towards the end, I thank the God for all of the blessings.

List of Publications

International Journal

1. **S. Panigrahy** and S.C. Mishra, The combustion characteristics and performance evaluation of DME (dimethyl ether) as an alternative fuel in a two-section porous burner for domestic cooking application, Energy 150 (2018) 176-189.
2. **S. Panigrahy**, Suppression of soot formation in premixed ethylene flame within SiC based porous inert burner, Fuel (2018) (Under review).
3. **S. Panigrahy** and S.C. Mishra, Effect of dimethyl ether as an additive to liquefied petroleum gas flame in SiC-Al_2O_3-based porous inert burner, Energy Fuels 31 (11) (2017) 12721-12740.
4. **S. Panigrahy** and S.C. Mishra, Analysis of combustion of liquefied petroleum gas in a porous radiant burner, Int. J. Heat Mass Transfer 95 (2017) 488-498.
5. **S. Panigrahy**, N.K. Mishra, S.C. Mishra, P. Muthukumar, Numerical and experimental analyses of LPG (liquefied petroleum gas) combustion in a domestic cooking stove with a porous radiant burner, Energy 95 (2016) 404-414.
6. S.C. Mishra, **S. Panigrahy**, V.J. Ghatage, Analysis of combined mode heat transfer in a porous medium using the lattice Boltzmann method, Numer. Heat Transfer, Part A 69 (10) (2016) 1092-1105.

International Conference

1. **S. Panigrahy,** Soot formation in premixed C_2H_4 flame within highly conducting and radiating porous burner, Proceedings of the International Conference on Sustainable Energy and Environmental Challenges, IISC, January 01-03, 2018.
2. **S. Panigrahy** and S.C. Mishra, Kinetic analysis of premixed DME/LPG/air combustion within a two-layer porous radiant burner, 24th National and 2nd International ISHMT-ASTFE Heat and Mass Transfer Conference, BITS-Pilani, December 27-30, 2017.
3. **S. Panigrahy**, Nirmal M.S., S.C. Mishra, Performance characteristics of biogas combustion with various compositions inside PIB based domestic cooking stoves,

12th International Conference on Flow Dynamics, Sendai, Japan, 27-29 October 2015.

4. **S. Panigrahy** and S.C. Mishra, Modelling of heat transfer in a kerosene fired pressure cooking stove**,** 12th International Conference on Flow Dynamics, Sendai, Japan, 27-29 October 2015.
5. **S. Panigrahy**, N.K. Mishra, P. Muthukumar, S.C. Mishra, Analysis of LPG combustion in a domestic cooking stove with a porous radiant burner, 23rd National and 1st International ISHMT-ASTFE Heat and Mass Transfer Conference, Trivandrum, Kerala, India, 17-20 December 2015.
6. V.J. Ghatage, **S. Panigrahy,** S.C. Mishra, Analysis of combined mode conduction and radiation in a porous matrix using lattice Boltzmann method, 23rd National and 1st International ISHMT-ASTFE Heat and Mass Transfer Conference, Trivandrum, Kerala, India, 17-20 December 2015.

SYNOPSIS

Name of the student: **Snehasish Panigrahy**	Roll No.: **146103036**
Degree for which submitted: **PhD**	Department: **Mechanical Engineering**
Thesis Title: **Investigation on Combustion in Porous Inert Burners Using Gaseous and Liquid Fuels**	
Name of the Supervisor: **Late Prof. Subhash C. Mishra and Prof. Gautam Biswas**	
Month & Year of Submission: **July, 2018**	

Combustion of gaseous as well as liquid fuels in conventional burners used in thermal devices such as boilers, domestic stoves and furnaces takes place in gaseous environment. Combustion of fuels in the gaseous environment is termed free-flame (FF) combustion. Thermal efficiencies of these devices operating on the FF mode are low, and emissions of CO and NOx are high. Household cooking stove running on liquefied petroleum gas (LPG) or kerosene is one such device that falls into this category.

To meet the requirements of higher thermal efficiency and reduced emissions, over last two decades, many studies have been made to improve the existing LPG and kerosene cooking stoves. In this regard, some researchers have extended the use of porous inert burner (PIB) to the cooking stoves to recirculates the lost heat from burned hot combustion products towards unburned incoming fuel-air mixtures. To further improve the performance of these stoves, two-layered PIB has been used by many researchers. The CO and NOx emissions are significantly low in the two-layered PIB than the conventional cooking stoves, and the thermal efficiency is also higher.

A critical review of previous literature reveals that the experimental investigations of the PIB-based cooking stoves reported in various studies were not guided by numerical analysis, and therefore, studies needed extensive experimental trials for stable combustion in the PIB. Thus, towards improving the performance of the PIB integrated cooking stove, computational modeling for combustion of the fuel-air mixture in these burners is required, which potentially lead to develop more effective burners. The proposed work is, therefore, to develop a numerical tool and validate the solver considering detailed multistep mechanisms with the experimentally measured results. In addition, based on the

analysis of experimental data and numerical predictions, the most appropriate burner considering various burner thickness, equivalence ratios, thermal efficiency and CO emissions with respect to the World Health Organization (WHO) emission standard limits is proposed in this thesis.

The present work aims at the numerical and experimental analyses of the combustion of gaseous and liquid fuels inside the PIB. The experiments are performed in a two-layer PIB comprising of silicon carbide (SiC) matrix and aluminum oxide (Al_2O_3) balls. Towards validation of the developed solver, the numerical model is compared to the experimental data from the present work. Volumetric radiative source term in the form of the divergence of radiative heat flux is accounted in the solid phase energy equation. With divergence of radiative heat flux calculated using the finite volume method (FVM), the coupled continuity, species conservation equation, ideal gas equation, energy equations for gas and solid phases are solved using the finite difference method. Species production rates, equation of state variables, transport and thermodynamic properties are calculated using open source software Cantera.

Because of increasing concern about stringent emission requirements and energy conservation, in recent years many researchers have paid significant attention to alternative fuels. As a promising renewable energy source, dimethyl ether (DME) is known as a leading alternative fuel additive. However, when DME is used in the conventional burners, difficulties associated with flame sustainability and low flammability limit arises due to its lower calorific value. Therefore, towards enhancing the fuel flexibility of the existing domestic stoves, the present work utilizes the heat recirculation mechanism of the PIB to these burners offering greater fuel compatibility for both LPG and DME. Furthermore, to analyze the complex kinetics and reaction pathways of LPG/DME combustion inside the burner, a comprehensive modeling of the PIB is studied through a detailed kinetic mechanism. The reaction pathway studies are performed using an extended kinetic model developed by adding various sub mechanisms taken from literature.

The results of the present work are of great importance, not only for providing high efficient and low emission burner fully compatible for both DME and LPG, but also for providing a solution to the limitations and challenges faced by current DME stove

market. In the present work, it has been found that with the addition of DME in the LPG-air mixture the peak radical pool concentration increases, which enhances the filtration velocity and thus the operating limit of the PIB. Moreover, with the use of DME instead of LPG, following the guideline of WHO, the maximum allowable equivalence ratio can be extended from 0.4 to 0.5 and the thermal load from 4.0 kW to 5.0 kW. Towards reducing the dependence on the petroleum product LPG, the results from the present study show excellent performance of the PIB-based stove with an improvement in radiant efficiency as well as a reduction in CO emission by the use of DME instead of LPG.

Despite the substantial research on the porous media combustion (PMC) involving both experimental and numerical investigations, to date, there is no study available in the literature addressing the formation and growth process of soot aerosols within the PIB. Thus, in this thesis, the effect of PMC on the formation of soot and its components inside the PIB is examined. The formation of soot due to the combustion of the fuel-rich ethylene-air mixture inside the PIB is assessed by using a detailed soot mechanism based on discrete sectional method (DSM). The results in this work show that the PIB not only reduces the CO emission but also can suppress the soot formation and delay the particle inception as compared to the premixed laminar FF combustion. The soot volume fractions at the PIB exit are predicted to be in the range of 10^{-12} - 1.5×10^{-7} which is very much lower than that of FF (10^{-7} - 10^{-6}) under all the input conditions examined in this study. In case of PIB, the maximum soot particle diameter is found to be 20 nm smaller than those formed in the FF condition. A brief discussion of the Chapter wise details of this Ph.D. thesis is provided below:

The present thesis contains 8 Chapters. The introductory Chapter provides a literature survey about the state-of-the-art of the PIB technology. Working principle and importance of the PMC for various application are discussed. Following the analysis of the available literature, the motivation and objectives of the present doctoral study are discussed for the research work.

The present study is an effort towards the feasibility of employing the concept of PIB in the domestic cooking burners. In order to study the complex combustion process inside the PIB, the complete non-equilibrium model to solve the macroscopic transport equations is presented in Chapter 2. The basic mathematical formulation and solution

procedure for solving the quasi-steady radiative transfer equation for the volumetric radiation source term of the porous medium using FVM are also described in detail. To compare the advantage of gaseous fuel combustion in the PIB over its combustion in the FF mode, in terms of both heat output and emissions, multistep chemical kinetics and detailed reaction mechanism are considered.

The third Chapter of the thesis reports the numerical and experimental analyses of LPG combustion within a two-layer PIB-based cooking stove. Numerical results of temperature distributions, flammability limits and pollutant emissions for various equivalence ratios and thermal loads are found to have a good agreement with the experimental data. Towards improving the thermal performance of the stove, effects of burner thickness, preheater thickness, solid-phase conductivity and scattering albedo on CO emissions and radiative flux are also studied.

To establish the applicability of DME as an alternative fuel additive to LPG for enhancing combustion and reducing hazardous emissions, in Chapter 4, the flame behavior of LPG-air mixture blended with DME is studied within the PIB under excess enthalpy combustion condition. New filtration velocity data are found for the stable combustion of LPG-DME-air mixtures inside the PIB. The effect of various DME volume fractions in the LPG-DME blends on temperature distribution, radical pool concentration, reaction zone thickness and syngas production are investigated. In Chapter 5, the performance of the DME fired PIB in terms of radiative efficiency, CO emissions and stable operating ranges for various input conditions are compared with the results for LPG combustion. Furthermore, the numerical model is used to investigate the dynamics of DME flame in the PIB through reaction path analyses.

Chapter 6 investigates the effect of PMC on the sooting behavior of premixed fuel-rich ethylene-air flame inside the PIB. In an effort to elucidate soot evolution processes, a DSM based soot kinetic mechanism comprising of 156 chemical species and 5600 reactions is used. Chapter 7 deals with the investigation of combustion of kerosene in a PIB integrated pressure cooking stove. The results show that with the incorporation of the porous matrix in the kerosene pressure stove, soot emissions go drastically down. Finally, the conclusions and recommendations of the future work are outlined in Chapter 8.

CONTENTS

LIST OF FIGURES

LIST OF TABLES

NOMENCLATURE

A_c	cross-sectional area (m^2)
C	specific heat (J/kg·K)
d_p	pore diameter (m)
E	experimental measurement uncertainty
G	emissive power (W/m^2)
h_V	volumetric heat transfer coefficient ($W/m^3 \cdot K$)
I	radiative intensity ($W/m^2 \cdot sr$)
LHV	lower heating value (J/kg)
m	mass flow rate (kg/s)
M	total number of intensities
P	pressure (Pa)
Q_{th}	thermal load input (W)
q_R	radiative heat flux (W/m^2)
R	universal gas constant (J/K·kmol)
t	time (s)
T	temperature (K)
$THRR$	total heat release rate ($J/m^3 \cdot s$)
u	velocity (m/s)
V_i	species diffusion velocity (m/s)
V_0	filtration velocity (m/s)
V_{0L}	free flame velocity (m/s)
W	molecular weight (kg/kmol)

x	space variable
Y	species mass fraction

Greek symbols

β	temperature exponent
ε	emissivity
φ	equivalence ratio
η	efficiency
κ_a	absorption coefficient (m^{-1})
λ	thermal conductivity (W/m·K)
θ	polar angle (rad)
ρ	density (kg/m^3)
σ	Stefan-Boltzmann constant ($W/m^2 \cdot K^4$)
υ_s	scattering coefficient (m^{-1})
ω	scattering albedo
ξ	porosity
Γ	extinction coefficient (m^{-1})

Superscripts

m	indices for discrete polar angles
R	related to radiation

Subscripts

g	gas phase
i	reaction number
in	inlet
k	species number

N	north face
out	outlet
P	cell center
s	solid phase
S	south face
F	fuel

ABBREVIATIONS

CB	cooking burner
CV	control volume
DME	dimethyl ether
FDM	finite difference method
FF	free flame
FVM	finite volume method
LFL	lean flammability limit
LPG	liquid petroleum gas
PAH	polycyclic aromatic hydrocarbon
PIB	porous inert burner
PM	porous medium
PMC	porous media combustion
PPC	pores per centimeter
ROP	rate of production
WHO	world health organization
1-D	one-dimensional

CHAPTER 1

INTRODUCTION

The combustion of fossil fuels in conventional combustion devices works on free-flame (FF) mode. In these devices, combustion takes place in the gaseous environment, and therefore their thermal efficiencies are low and pollutant emissions are high. The harmful pollutions, such as carbon monoxide (CO), nitric oxides (NO_X), greenhouse gases, and soot particulates generated due to the burning of gaseous as well as liquid fuels in the conventional burners cause adverse effect on the environment. In this regard, to reduce the hazardous emissions from these devices, significant amount of research has been dedicated for the development of efficient and environmentally friendly combustion techniques. Porous inert burner (PIB) is one such technology that utilizes heat recirculation features of highly conducting and radiating porous matrix (PM) for offering lower levels of CO and NOx emissions as well as higher thermal efficiency than the burners operating on the basis of FF combustion.

The combustion of air-fuel mixture within a PIB helps in stabilizing of flame within the pore structure of the solid matrix/media. Exhaust products heat the PIB downstream of the flame zone. Some of this heat is then conducted and radiated back to upstream section, which preheats the incoming air-fuel mixture. The super-adiabatic combustion caused by the recirculation of sensible enthalpy from the hot combustion products to the unburnt air-fuel mixture favors complete oxidation of the fuel, which consequently reduces the CO and unburned hydrocarbon emissions, while the low flame temperature in

the post-flame region of the PIB inhibits the NOx production. Because of improved heat transfer through the combined modes of conduction, convection and radiation within the PM, not only can low heating value fuels be easily combusted but also a substantial improvement in burning velocity, radiant output, flammability limit and power density can be attained. Owing to higher stability range and better emission characteristics, PIB integrated with thermal devices has been considered as a potential substitute to conventional burners. Because of these unique features, the PIB technology has gained specific importance in recent years.

1.1. Work Done in the Area of PIB

The concept of borrowing energy from a premixed flame to preheat the incoming reactants within the PM was first introduced by Weinberg [1]. Following Weinberg's idea, over the last four decades, a good amount of numerical [2-16], analytical [18] as well as experimental studies [3,8,19-24] pertaining to both gaseous and liquid fuels combustion in PM, and its various applications have been reported by many, and developments until 2010 have been summarized in review papers [25-30]. Combustion in the PM is characterized by lower NOx and CO emissions [31-33], extended limits for a stable flame [34], high flame speed [2, 3], and a high power density [35]. Potential applications of devices employing porous media combustion (PMC) are, but not limited to IC engines [36-38], heat exchangers [39, 40], gas turbines and propulsion [20, 41], burners of cooking stoves [21], hydrogen and syngas production [22,24].

With advances in computing power and computational methods, numerical modeling has become a precursor to the design and development of any device. It helps in identifying the geometric and operating parameters to get the desired output. In the area of PMC, many researchers have done the analysis using different methods, and have outlined the influence of different parameters on gas and solid temperatures, heat flux, and CO emission. In the numerical analysis of the PMC, the work of Tong and Sathe [4] reported way back in 1991 bears significance. In a 1-D planar PM, to account for the non-local thermal equilibrium between the gas and the solid, they considered coupled energy equations for the gas and the solid phases. Heat generation due to combustion was assumed in the form of a centrally located uniform volumetric heat generation source, and volumetric radiation was accounted in the solid-phase energy equation. For a given rate

of heat generation, large optical thickness and high heat transfer coefficient between the solid and the gas phases were found desirable for maximizing the radiant output. Application of PM to study the heat transfer characteristics was extended by Talukdar et al. [11]. With combustion modeled as a localized volumetric heat generation zone, they incorporated non-local thermal equilibrium between the gas and solid phases of the PM by using separate energy equations for them. Sathe et al. [3] modeled the methane-air oxidation using a one-step irreversible reaction and compared it to theoretical predictions. It was found that the stable combustion could be maintained in two spatial domains, one in the upstream half of the porous segment and another at the downstream edge of the segment. The flame speed and radiative output were highest when the flame was located at the center of the segment.

In the analysis of combustion, estimation of emission products is an important aspect, and this cannot be accurately predicted with one-step irreversible reaction as reported in [2, 3, 16]. To address this issue, Hsu and Matthews [5] have justified the usage of multi-step kinetics model with detailed reaction mechanism. Diamantis et al. [10] and Mishra et al. [12] have investigated methane-air combustion within PIB with detailed chemical kinetics. 164 chemical reactions with 20 species were considered. Separate energy equations for gas and solid phases were solved and the effects of the power density, equivalence ratio, extinction coefficient and volumetric heat transfer coefficient on temperature and concentration profiles were studied.

Stable burner operating range of PIBs has been studied by many researchers. Hanamura and Echigo [42] considered a 1-D model to analyze the flame stabilization mechanism in the PIB. Three critical limiting criteria for flame stabilization, i.e., blow off under the condition of higher mixture velocity than the burning velocity of the flame in free space, flame extinction under extremely low mixture velocity, and flashback into the PM were identified. The flame was stabilized only in the upstream half of the PM and was not sustained in the downstream half. Similar findings were reported by other researchers [2, 6] who had determined the stable operating limits by fixing the flame location inside the PIB. Bidi et al. [43] used entropy generation minimization method to study flame stabilization. It was found that the flame occurring upstream half of the PM was more

stable, more efficient, and produced less emission than those at the downstream half of the porous layer.

In PMC, volumetric thermal radiation plays an important role, and thus its consideration in the analysis is paramount. The volumetric radiation can be computed using any of the numerical radiative transfer methods like the discrete ordinates method [9], collapsed dimension method [12], Rosseland approximation [43], P_3 approximation [44], and finite volume method (FVM) [45]. The importance of thermal radiation and of the radiative properties, viz., extinction coefficient, scattering albedo, scattering phase function in the analysis of PIB was studied numerically by Malico and Pereira [9]. They found that the temperature profiles were very sensitive to perturbation in the radiative coefficients, particularly when the scattering albedo was increased. When radiation was neglected, the predicted temperature profile was not in agreement with the available experimental values. Hendricks and Howell [46] found that scattering was far more important than absorption in PIB and that the scattering and absorption coefficients were relatively constant with wavelength and the phase function was mostly isotropic.

The input firing rate and equivalence ratio greatly influence the CO and NOx emissions and in this direction, numerous studies have been made in order to assess the effect of different operating conditions on various pollutant emissions of the PIB. At a given equivalence ratio, both Mital et al. [47] and Khanna et al. [48] reported an increase in CO concentration for the higher firing rate of the PIB, while NOx was measured to decrease with increase in thermal load input. A similar trend was observed by Xiong et al. [49] and Scribano et al. [50] where ultra-low emissions (<15 ppm) were achieved for CO and NOx pollutants under their respective operating conditions.

The combustion devices based on PIB exhibit better thermal performances than the conventional burners. In the recent past, several researchers [21, 51, 52] have extended the application of PMC to domestic burners to improve thermal efficiency and CO emission characteristics. Jugjai and Rungsimuntuchart [51] suggested mechanisms to extract heat from the burnt gases in the conventional liquefied petroleum gas (LPG) burner to achieve high thermal efficiency. They used PM to preheat the incoming LPG-air mixture. Dongbin et al. [53] investigated the effect on the combustion of porous ceramic stove doped with rare earth elements. They observed that the addition of rare

earth elements to porous ceramic led to saving of the fuel consumption by 4.5%, and reduction in CO emission by 40.9%.

1.2. Motivation for the Proposed Work

Globally, various petroleum products like LPG, kerosene, natural gas, and biomass products like crop residue and cow dunk have been used as the main conventional energy sources for household cooking applications. In particular, LPG and kerosene are widely used fossil fuels in these cooking devices as compared to solid fuel counterparts. However, the traditional LPG and kerosene cooking stoves contribute significantly to indoor air pollution emitting pollutant level higher than the restriction limit prescribed by the World Health Organization (WHO). As per the report of WHO, globally, 4.3 million deaths were attributable to indoor air pollution in 2012 [54]. Several acute lower respiratory diseases, chronic obstructive lung diseases and ischaemic heart diseases in the developing countries have been attributed to the higher levels of indoor pollution. Considering environmental protection issues and stringent emission regulation, there is a need to explore the ways to improve the thermal efficiency and emission characteristics of the existing domestic LPG and kerosene stoves.

The average thermal efficiency of the LPG and kerosene cooking stoves available in the Indian market is in the range of 60-65% and 45-55% respectively. At the same time, the CO emissions from these cooking burners are above the current standards of WHO. In order to overcome the disadvantages of the cooking stoves, many studies have been conducted to explore design modifications of these burners [55-58], which possibly lead to higher thermal efficiency and lower pollutant emission. However, in all such studies, combustion of premixed air-fuel mixture took place in the open air environment over perforated metallic burner head. This led to the loss of significant amount of energy through the exhaust gas. Since the gases have low thermal conductivity and have low opacity, the contributions of conduction and radiation modes of heat transfer from the post-flame to pre-flame zone are negligible. Thus, due to poor heat transfer, these burners have low thermal efficiency, low turndown ratio, higher pollutant emissions, etc. So it is clear that, instead of combustion in the open air environment, if air-fuel mixture is made to combust in a conductive and radiating PM, then owing to enhanced heat transfer, significant improvement in thermal efficiency and reduction in emission can be achieved.

Towards enhancing the existing stove effectiveness, Pantangi et al. [59] proposed highly conducting and radiating PIB instead of perforated metallic burner head in the LPG cooking stove. They investigated the thermal efficiency and emission characteristics of the conventional domestic LPG cooking stoves with various PM such as metal balls, pebbles and metal chips. The maximum thermal efficiency increase of 4% was obtained with metal chips. In another work [21], to improve the flame stabilization and burner effectiveness of the LPG cooking stove, two-layered PIB was used. The combustion was allowed to take place in the combustion zone made of silicon carbide (SiC) PM, and the preheating zone was filled with alumina balls (Al_2O_3) of 3 mm diameter. The measured CO and NOx emissions were found to be significantly low in PIB than the conventional LPG cooking stoves. The feasibility of burning liquid fuel within a PIB was studied by Sharma et al. [60] for kerosene pressure stove. They investigated the optimum efficiency of the burner through exergy calculation analyses and found higher thermal efficiency for the PIB integrated stove as compared to the traditional pressure cooking burners. Nevertheless, the above researchers [21, 52, 59, 60] have used numerous experimental trial and error methods to explore the stable combustion of air-fuel mixtures inside the PIB. Thus, numerical modeling of heat transfer in the PIB is required for better assessment of geometric and operating parameters of the burner without the need for extensive experimental trials.

In developing countries like India and China, considering the increase in petroleum product consumption and sudden rise in dependence on imported LPG, there is a need to pay significant attention to alternative fuels. As a promising renewable energy source, dimethyl ether (DME) is one of the excellent alternative fuel with similar physical properties as that of the LPG. DME which can be produced from the renewable resources like coal bed, methane, agriculture waste, syngas and CO_2-rich feedstocks, is a low carbon content fuel and is environmentally friendly. As an additive with petroleum-based fuels it can reduce emissions, polycyclic aromatic hydrocarbons (PAH), and soot [61, 62]. To establish the superiority of DME as a substitute fuel, numerous investigations have been conducted in diesel engines [63], homogeneous charge compression ignition engines [64], gas turbines [65], and heating [66] and cooking applications [67]. However, when DME is allowed to combust in conventional burners, problems related to flame

sustainability, low flammability limit, and low thermal efficiency arise because of its lower calorific value [67-69].

Marchionna et al. [67] investigated the potential of DME as a substitute fuel for household applications and observed that combustion could not be sustained in existing burners for DME concentration above 20% in the LPG-DME mixture. Arya et al. [68] studied the effect of DME addition on LPG cooking burners and found that the thermal efficiency decreased by 5.26% when DME volume fraction in the DME-LPG mixture increased to 20%. Similar observation of a decrease in thermal efficiency with the increase of DME blend in the conventional cooking stoves was reported by Anggarani et al. [69]. However, to date, only a few studies [67-70] have been performed to establish the viability of DME as a substitute fuel in the domestic LPG cooking stoves and these studies have revealed that to burn DME-LPG blend with DME volume fraction above 20%, the burner requires modification of its components and design. Indeed, reports in the literature suggest that DME and LPG are not completely interchangeable by using the existing conventional LPG stoves. In order to overcome these shortcomings, there is a need to improve the existing burners toward providing better fuel compatibility for both LPG and DME.

Furthermore, it is observed from the relevant literature that although some efforts have been made concerning the applicability of employing the idea of PIB in domestic burners, fundamental studies toward analyzing the complex kinetics and flame dynamics of air-fuel mixture inside the PM have not been reported to date. Therefore, in this work, a detailed and comprehensive modeling of the LPG and DME flames inside the PIB are also investigated through reaction pathways and rate of production analyses.

Combustion-derived soot particulates generated due to the burning of fuel-rich mixtures and liquid fuels pose adverse effects on human health and climate change. Toward understanding the fundamental of complexity in soot formation process, many studies have been performed in laminar premixed FF [71-73] over the last two decades. To explore the thermal dependence of the aerosol dynamics Ciajolo et al. [74] and Böhm et al. [75] studied the effect of flame temperature on the soot production process and observed an inverted bell-shaped profile for the soot volume fraction with a reduced amount of soot formation at low and high temperature. In order to accurately capture the

soot inception, surface growth and particle oxidation mechanism in FF combustion, various kinetic models, such as two-equation model [76, 77], method of moments model [78-80], stochastic method [81, 82] and sectional model [83-85] have been proposed that can be coupled with different thermal systems to predict the aerosols dynamics. From the literature survey, it is also revealed that, in spite of the negative impact of soot components on public health and environment, no studies have been performed regarding soot particle evolution process in the PIB. Thus, toward addressing these issues, the problem statements for the present research work along with the roadmap are summarized in the following section.

1.3. Problem Statement and Roadmap

The main motive of this thesis is to perform both experimental and numerical investigation of gaseous and liquid fuels combustion inside highly conducting and radiating PIB for various operating parameters such as equivalence ratio and input thermal load conditions. For the current research work, single-layer and two-layer PIB are taken into account to analyze the complex combustion process within the burner. In view of the specified problem-statement, the following roadmap is defined for the present study:

I. To develop a numerical model to permit the heat transfer analyses in the PIB considering detailed kinetics mechanisms, and validate the solver with the experimentally measured results.
II. To investigate the effects of equivalence ratio, flame speed, different PM properties like burner conductivity and scattering albedo on the variation of CO emission, radiative heat flux and heat release rate profiles of the PIB.
III. To perform numerical and experimental investigation of combustion of LPG (48% n-C_4H_{10}, 25% i-C_4H_{10}, 23% C_3H_{10}, 4% C_2H_6 by volume) inside the PIB stove.
IV. To employ the heat recirculation technique of the PIB in the cooking stove for analyzing the fuel flexibility of both LPG and DME.
V. To study the effect of DME addition on premixed LPG-air combustion within the PIB under both fuel-lean and fuel-rich conditions.
VI. To carry out reaction pathway and the rate of production (ROP) analysis at various locations of the PIB.

VII. To investigate the formation of soot particulate and their growth process within the PIB.

VIII. To analyze the combustion of kerosene in a PIB integrated kerosene pressure stove.

1.4. Summary

With a detailed survey about the various works that has been done till date related to PMC technology, the motivation for the present doctoral study was presented, and based on the review of the available literature, the objective and problem statement of the current research work were defined along with the roadmap. Subsequent Chapters address the experimental and numerical analyses aimed at achieving these goals.

CHAPTER 2

NUMERICAL MODELING OF PIB

In countries like India, China, Thailand, Pakistan and Bangladesh, domestic cooking stoves work on LPG. In the numerical studies reported in the literature, except [13], mostly [2-10, 12, 40, 43], CH_4 has been used as a fuel in the PIB. Contributing towards the recent development of LPG cooking stove with PIB in mind, in this Chapter, a mathematical model is developed with detailed radiation modeling to predict the combustion of the fuel-lean LPG-air mixture within a single-layer PIB. Towards the validation of the formulation and the developed code, CH_4 combustion inside a single-layer PIB is considered. To demonstrate the advantage of combustion of LPG within the PIB, comparisons are made with the CH_4 flame inside PIB as well as with the combustion of LPG in the FF mode. The numerical method and formulations described in this Chapter are utilized throughout the entire study for analyzing the complex heat transfer mechanism inside the PIB.

2.1. Numerical Method and Radiation Formulation

Consideration is given to a 1-D planar PM (Fig. 2.1a) of thickness 0.03 m. The air-fuel mixture enters the PM through its bottom (x_{in}) surface, and soon after the combustion is initiated by a spark at the top (x_{out}) surface, it spreads throughout the volume of the PM. Combustion of fuel leads to the generation of heat and production of species. Heat generation in the reaction zone gives rise to heat transfer by convection from the gas to

the PM. The PM being conducting and radiating, heat transfer by conduction and radiation manifests throughout the PM. Upstream of the reaction zone, conduction and radiation elevate the temperature of the PM, and through convective heat transfer, the incoming fuel-air mixture gets preheated. Downstream to the reaction zone, owing to the additional contribution of energy transfer by advection, gas temperature is more than that of the PM, and, therefore, convective heat transfer takes place from the gas to the solid.

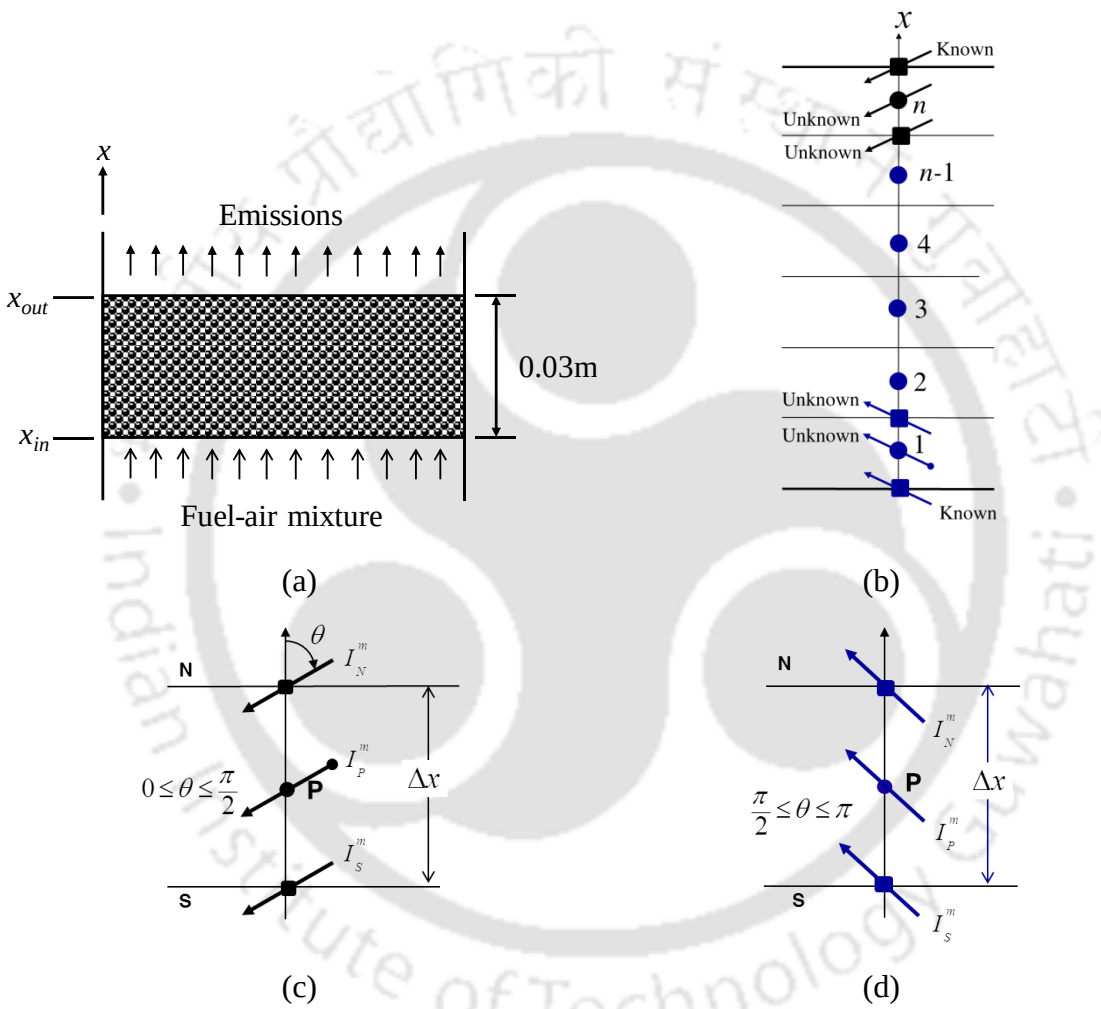

Fig. 2.1. (a) Schematic of the PIB, **(b)** ray tracing in the FVM, **(c)** south-bound $\left(0 \le \theta \le \frac{\pi}{2}\right)$ rays and **(d)** north-bound $\left(\frac{\pi}{2} \le \theta \le \pi\right)$ rays.

Analysis of the present problem requires simultaneous solution of continuity equation, species conservation equation, gas-phase and solid-phase energy equations and the ideal gas equation. The governing equations are given as:

Continuity equation:

$$\frac{\partial(\xi\rho_g)}{\partial t}+\frac{\partial(\xi\rho_g u)}{\partial x}=0 \tag{2.1}$$

Gas-phase energy equation:

$$\xi\rho_g C_g\left(\frac{\partial T_g}{\partial t}+u\frac{\partial T_g}{\partial x}\right)+\xi\sum_{k=1}^{K}\rho_g Y_k C_{g,k} V_k\frac{\partial T_g}{\partial x}+\xi\sum_{k=1}^{K}\dot{\omega}_k h_k W_k +h_V(T_g-T_s)=\xi\frac{\partial}{\partial x}\left(\lambda_g\frac{\partial T_g}{\partial x}\right) \tag{2.2}$$

Solid-phase energy equation:

$$(1-\xi)\rho_s C_s\frac{\partial T_s}{\partial t}-h_V\left(T_g-T_s\right)=(1-\xi)\lambda_s\frac{\partial^2 T_s}{\partial x^2}-\frac{\partial q_R}{\partial x} \tag{2.3}$$

Species conservation equation:

$$\xi\rho_g\left(\frac{\partial Y_k}{\partial t}+u\frac{\partial Y_k}{\partial x}\right)=-\frac{\partial}{\partial x}\left(\xi\rho_g V_k Y_k\right)+\xi\dot{\omega}_k W_k \tag{2.4}$$

Ideal gas equation:

$$\rho_g=\frac{P\overline{W}}{RT_g} \tag{2.5}$$

Elementary reversible or irreversible reactions involving K number of chemical species can be written in the general form as

$$\sum_{k=1}^{K}\upsilon'_{ki}\chi_k \Leftrightarrow \sum_{k=1}^{K}\upsilon''_{ki}\chi_k \tag{2.6}$$

where υ_{ki} are the stoichiometric coefficients for k_{th} species in the i_{th} reaction, and χ_{k} is the chemical symbol for the k_{th} species. The superscripts $'$ and " refer to the forward and reverse stoichiometric coefficients, respectively.

The species production rate is calculated from

$$\dot{\omega}_k=W_k\sum_{i=1}^{I}\left(\upsilon''_{ki}-\upsilon'_{ki}\right)\times\left(k_{f_i}\prod_{k=1}^{K}\left[X_k\right]^{\upsilon'_{ki}}-k_{r_i}\prod_{k=1}^{K}\left[X_k\right]^{\upsilon''_{ki}}\right) \tag{2.7}$$

where I is the number of reactions, $\left[X_k\right]$ is the molar concentration of the k_{th} species. k_{f_i} represents the forward rate constants, while k_{r_i} represents the reverse rate constants of the i_{th} reaction.

The forward rate constants are calculated from the modified Arrhenius expression represented by

$$k_{f_i} = A_i T_g^{\beta_i} \exp\left(-\frac{E_i}{RT_g}\right) \tag{2.8}$$

where A_i is the pre-exponential steric factor, β is the temperature exponent, and E_i is the activation energy for the i^{th} chemical reaction.

2.1.1. Radiation formulation

The radiative source term of the PM can be calculated using the FVM [86] for solving the quasi-steady radiative transfer equation (RTE). The divergence of radiative heat flux $\frac{\partial q_R}{\partial x}$ appearing in the solid-phase energy equation (Eq. (2.3)) is given by

$$\frac{\partial q_R}{\partial x} = \Gamma(1-\omega)\left(4\sigma T_s^4 - G\right) \tag{2.9}$$

where Γ is extinction coefficient, ω is scattering albedo, $\sigma = 5.67\times10^{-8}\,\mathrm{W\cdot m^{-2}\cdot K^{-4}}$ is the Stefan-Boltzmann constant and G is the incident radiation. With I as the intensity, M as the total number of intensities considered over the complete span $(0 \le \theta \le \pi)$ of the polar space and m as the index for the discrete direction, for the geometry (Fig. 2.1a) under consideration, incident radiation G is given by and computed from the following [86]:

$$G = 2\pi\int_0^{\pi} I\theta\sin\theta d\theta \approx 4\pi\sum_{m=1}^{M} I^m \sin\theta^m \sin\left(\frac{\Delta\theta^m}{2}\right) \tag{2.10}$$

The heat flux q_R is given by,

$$q_R = 2\pi\int_{\theta=0}^{\pi} I(\theta)\sin\theta\cos\theta d\theta \approx 2\pi\sum_{m=1}^{M} I^m \sin\theta^m \cos\theta^m \sin\left(\Delta\theta^m\right) \tag{2.11}$$

In Eqs. (2.10) and (2.11), the intensity I^m is computed by solving the RTE, which for the planar geometry with isotropic scattering for a discrete direction θ^m is given by

$$\cos\theta\frac{dI^m}{dx}=-\Gamma I^m+\Gamma(1-\omega)\frac{\sigma T_s^4}{2}+\frac{\Gamma\omega}{4\pi}G=-\Gamma I^m+S \tag{2.12}$$

where S is the source term.

In the FVM approach [86], for the geometry (Fig. 2.1a) under consideration, with reference to Figs. 2.1b-d, Eq. (2.12) is integrated over the discrete angular span $\pi\Delta\theta$ and 1-D control volume (CV) $(\Delta x\times 1\times 1)$. This results in

$$\left[I_N^m-I_S^m\right]D^m=\left(-\Gamma\Delta x I_P^m+\Delta x S_P^m\right) \tag{2.13}$$

where with reference to Figs. 2.1b-d, I_N^m, I_S^m and I_P^m are intensities in discrete direction θ^m at north face, south face, and center of the CV, respectively. Figures 2.1c and 2.1d show token discrete intensities in angular space $0\le\theta\le\frac{\pi}{2}$ and $\frac{\pi}{2}\le\theta\le\pi$, respectively. It is to be noted that intensities I^m in the angular space $0\le\theta\le\frac{\pi}{2}$ originate from the north boundary, and those in the angular space $\frac{\pi}{2}\le\theta\le\pi$ originate from the south boundary. In Eq. (2.13), S_P^m is volume averaged source term calculated at the central node P.

Calculations of intensities start from the boundaries. For intensities originating from the north boundaries, for the boundary CV, the southbound intensities I_N^m at the north face (Fig. 2.1c) are known from the radiative boundary condition. Similarly, intensities originating from the south boundaries, for the boundary CV, the northbound intensities I_S^m are known. For these CVs, in directions $0\le\theta\le\frac{\pi}{2}$ and $\frac{\pi}{2}\le\theta\le\pi$, the unknown intensities I_P^m are calculated by substituting in Eq. (2.13) the known boundary intensities by relating I_N^m, I_S^m and I_P^m with the diamond rule

$$I_P^m=\frac{I_N^m+I_S^m}{2}. \tag{2.14}$$

The resulting unknown intensities I_P^m are thus calculated from the following:

$$I_P^m=\frac{\left|2D^m\right|I_N^m+\Delta x S_P^m}{\left|2D^m\right|+\Gamma\Delta x},\ \text{for}\ 0\le\theta\le\frac{\pi}{2}\ \text{and}\ I_P^m=\frac{\left|2D^m\right|I_S^m+\Delta x S_P^m}{\left|2D^m\right|+\Gamma\Delta x},\ \text{for}\ \frac{\pi}{2}\le\theta\le\pi \tag{2.15}$$

It is to be noted that the $|\ |$ sign in Eq. (2.15) is included to make sure that intensities are not negative. With I_P^m known, the next unknown intensities in the particular CV, for example, I_N^m for CV 1 (Figs. 2.1b and 2.1d) and I_S^m for CV n (Figs. 2.1b and 2.1c) are calculated from Eq. (2.14). This procedure is followed recursively while marching from both the boundaries until all CVs are traced. With ε as of the emissivity of the PM, the boundary intensities are calculated from the following

$$I_{N/S}^m = \frac{\varepsilon \sigma T_{s,N/S}^4}{\pi} + \left(\frac{1-\varepsilon}{\pi}\right) q_{wall} \tag{2.16}$$

where $T_{s,S}$ and $T_{s,N}$ are temperatures of the south (x_{in}) and the north (x_{out}) surfaces of the PM, respectively, and M is the total number of discrete intensities considered over the complete span $0 \le \theta \le \pi$ of the polar space.

The radiative heat flux (q_{wall}) from the burner boundaries is computed from,

$$\begin{aligned} q_{wall} &= 2\pi \sum_{m=M/2}^{M} I^m \left|\cos\theta^m \sin\theta^m \left(\sin\Delta\theta^m\right)\right|; \frac{\pi}{2} \le \theta \le \pi \\ &= 2\pi \sum_{m=1}^{M/2} I^m \cos\theta^m \sin\theta^m \left(\sin\Delta\theta^m\right); 0 \le \theta \le \frac{\pi}{2} \end{aligned} \tag{2.17}$$

The values of volumetric heat transfer coefficient h_V and pore diameter d_p are calculated from the following correlations [87],

$$\frac{h_V d_p^2}{\lambda_g} = \left(0.0426 + \frac{1.236}{L/d_p}\right) \mathrm{Re}, \quad d_p = \frac{\sqrt{4\varphi/\pi}}{\mathrm{PPC}} (\mathrm{cm}) \tag{2.18}$$

where PPC is the pores per cm of the PM and $\mathrm{Re} = \frac{\rho u d_p}{\mu}$.

2.1.2. Boundary and initial conditions

The species mass fractions and the temperature are known at the inlet of computational domain, while at the outlet all gradients are set to zero, to ensure that equilibrium is reached in the PIB. At the inlet (x_{in}) surface of the PIB, the boundary conditions are:

$$\left.T_g\right|_{x=x_{in}^-} = \left.T_g\right|_{x=x_{in}^+}$$
$$\left.\dot{m}\right|_{x=x_{in}^-} = \left.\xi\dot{m}\right|_{x=x_{in}^+} \qquad (2.19)$$
$$\left.Y_k\right|_{x=x_{in}^-} = \left.\xi Y_k\right|_{x=x_{in}^+}$$

The values of $\dot{m}_{in}$ and $Y_{k,in}$ depend on the input thermal load (Q_{th}) and equivalence ratio (φ). $\dot{m}_{in}$ is the mass flow rate of the incoming fuel-air mixture, and is expressed as $\dot{m}_{in} = \dot{m}_f + \dot{m}_{air}$, where $\dot{m}_f \left(= \frac{Q_{th}}{LHV_f}\right)$ is the mass flow rate of fuel and $\dot{m}_{air}$ is the mass flow rate of air, which is calculated from the equation, $\varphi = \frac{\left(\dot{m}_{air}/\dot{m}_f\right)_{stoichiometric}}{\left(\dot{m}_{air}/\dot{m}_f\right)_{actual}}$. $Y_{k,in}$ is the mass fraction of various chemical reactants in the fuel-air mixture, calculated from the known value of φ. At the burner exit zero gradient boundary conditions are imposed for all the parameters to confirm that complete equilibrium is established inside the PIB, while at the outlet the solid-phase energy equation is subjected to the following boundary condition,

$$(1-\xi)\lambda_s \frac{dT_s}{dx} + (1-\xi)h_V\left(T_s - T_g\right) + (1-\xi)\varepsilon\sigma\left(T_s^4 - T_\infty^4\right) = 0 \qquad (2.20)$$

It is to be noted that in Eq. (2.20) T_s represents the temperature of the outer boundaries $(x_{in}$ and $x_{out})$ of the PIB. When Eq. (2.20) is applied to the boundary at x_{in}, $T_s = T_{s,S}$ and when it is applied to the boundary at x_{out}, $T_s = T_{s,N}$.

The present solver allows the user to specify initial estimates for mass flux, temperature, and the mass fractions profiles. At the entrance of the burner, the initial temperature profile is set equal to the inlet condition (298 K) and linearly increases to their adiabatic flame temperature at the PM center and remain at this value until the top boundary of the burner. The initial species mass fraction profiles starts from the stated boundary values and varies to their equilibrium values at the burner exit. The property parameters required for the numerical analysis are given in Table 2.1.

Table 2.1. PIB property data [10].

Material	SiC
Porous burner length	30 mm
PPC	8
Porosity (ξ)	0.9
Pore diameter (d_p)	1.34 mm
Thermal conductivity (λ_s)	0.15 W/m·K
Scattering Albedo (ω)	0.8
Extinction coefficient (Γ)	$3.0(1-\xi)/(0.00134)\,\mathrm{m}^{-1}$
Emissivity (ε)	0.8

2.1.3. Solution method

The solid-phase energy equation (Eq. 2.3), volumetric radiation information (Eq. 2.9) and convective heat transfer between solid and gas medium are included to the premixed laminar code Cantera [88] to solve the above formulations for the PIB. The volumetric radiative term $\frac{\partial q_R}{\partial x}$ needed in the solid-phase energy is solved using the FVM, while the solid-phase energy equation is solved using the tridiagonal matrix Thomas algorithm via the finite difference method (FDM). The solver Cantera simulates the modified coupled macroscopic transport equations by Newton-minimization method [89] using pseudo-transient solution with spatially changing time steps. The convective fluxes are approximated using the first-order upwind difference formula and the diffusive terms are discretized by the conservative second-order central-difference scheme.

The solver allows the user to define appropriate initial and boundary conditions for the gas phase temperature and species concentrations at the inlet of the burner domain. The solver also needs the user to specify a flame location in the PM by assigning the gas temperature at an interior point of the computational domain $(x_{in} \le x \le x_{out})$, and the flame speed V_0 is found as part of the solution. To determine the transport properties, thermal diffusion and multicomponent diffusion models are adopted.

Adaptive mesh criteria are used to find the grid independent solution, and the parameters: ratio = 2, slope = 0.05 and curve = 0.1, yield grid points in the range of 530-590. The initial estimation is on a coarse grid with 200 grid points. Once the solid-phase energy equation, continuity equation, species conservation equation, ideal gas equation and the gas-phase energy equation are solved on the coarse grid, new grid points are added in the computational domain where the solution or its gradients change quickly. This process of mess refinement continues until the grid refinement criterion (ratio = 2, slope = 0.05 and curve = 0.1) is met.

2.2. Results and Discussions

In the following, the formulation outlined before is validated first. This validation is done for CH_4 combustion in a PIB reported by Diamantis et al. [10]. For validation as well as combustion of LPG, the dimensions of the PM, and thermophysical and optical properties are the same as that of Diamantis et al. [10]. Axial distributions of solid and gas temperatures, burner stability range in terms of filtration velocity and mixture flow rate with equivalence ratio, radiant heat fluxes, and variation of CO emissions with equivalence ratio are analyzed. For the purpose of comparison, results of CH_4 combustion in the PIB are also presented. Further to assess the superiority of combustion in the PM, results of LPG combustion in the FF mode are also analyzed.

2.2.1. Validation

Towards the validation of the formulation, results from the present work are validated with that of Diamantis et al. [10] where CH_4 is used as the fuel for combustion inside the PM. For computation of the lean CH_4-air combustion, the GRI 2.11 [90] mechanism is used, which consists of 249 reactions and 49 species, while the thermal and transport data for LPG-air combustion are taken from USC mech 2 mechanism [91] which consists of 111 species and 784 reactions. For equivalence ratio φ = 0.5 and 0.9, and four different values of $\frac{V_0}{V_{0L}}$, in Figs. 2.2a-d, axial temperature distributions of gas and solid are compared with that of [10]. These comparisons are made for the reaction zone stabilized in the mid-section (Figs. 2.2 a, c) and upstream of the mid-section (Figs. 2.2 b, d). In all

four cases, results from the present work are found to compare exceedingly well with that reported in [10].

An observation of temperature distributions in Figs. 2.2a-d shows that for the same equivalence ratio, the filtration velocity V_0 increases when the flame stabilizes in the mid-section. Also, with the flame located in the mid-section, when the lean equivalence ratio increases, gas and solid temperatures both increase. This observation is in tune with [2,6,42,43]. It has been reported in [2,6,42,43] that for the stable performance, the reaction zone should not be located downstream of the mid-section. Thus, in the following, results are analyzed for the reaction zone located in the bottom half section of the PIB.

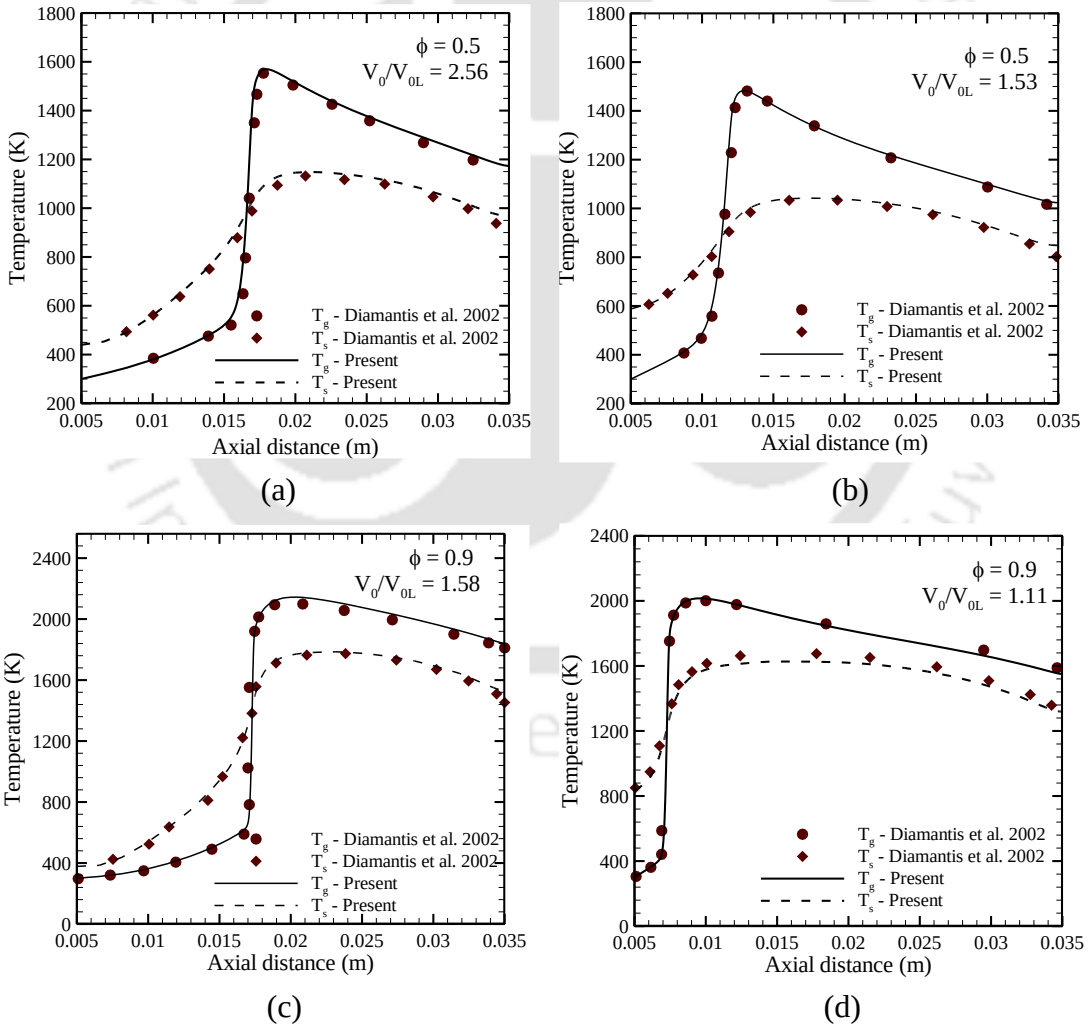

Fig. 2.2. Comparison of variations of T_g and T_s for equivalence ratio and flame speed ratio V_0/V_{0L} **(a)** (0.5, 2.56), **(b)** (0.5, 1.53), **(c)** (0.5, 1.53) and **(d)** (0.9, 1.11).

2.2.2. Ray independent test

In the presence of the volumetric radiation $\frac{\partial q_R}{\partial x}$, for a given number of CVs, results depend on the number of intensities considered over the spherical space. For the 1-D planar geometry considered in the present work, radiation is azimuthally symmetric. Thus, intensities in the polar space $(0 \le \theta \le \pi)$ need to be considered. With equivalence ratio $\varphi = 0.6$ and $\frac{V_0}{V_{0L}} = 2.29$, effect of number (M) of intensities on the axial variation of solid temperature T_s is shown in Fig. 2.3. Figure 2.3a shows this variation over the entire thickness of the PIB, whereas the zoomed view of the peak temperature is shown in Fig. 2.3b. Between $M = 2$ and $M = 16$, the difference in the maximum temperature is 26 K. The maximum temperatures corresponding to $M = 16$ and 24 are almost the same. Thus, in the following, in the calculation of the volumetric radiative source term $\frac{\partial q_R}{\partial x}$, 16 intensities are considered.

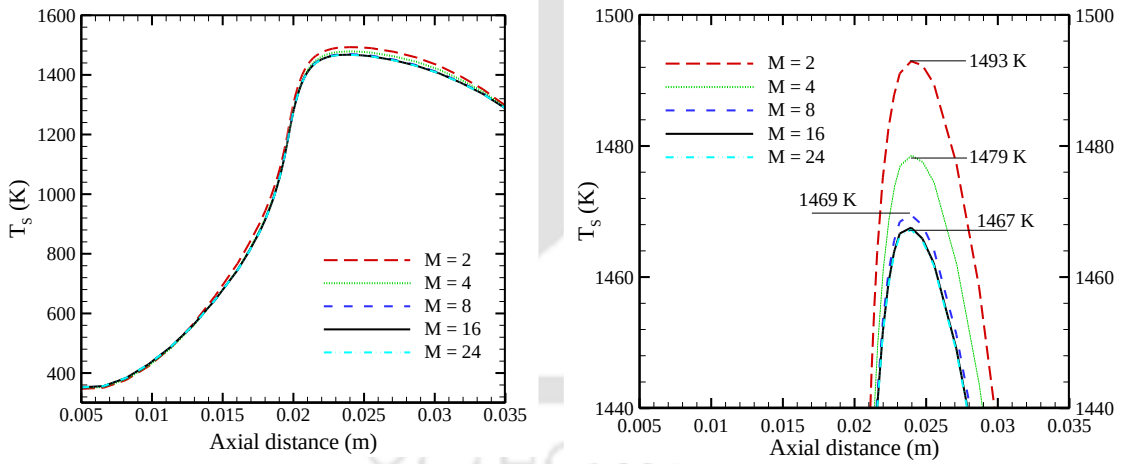

(a) (b)

Fig. 2.3. Effect of number of rays on axial solid phase temperature distribution **(a)** complete axial range and **(b)** zoomed view; $\varphi = 0.6$.

2.2.3. Heat release rate

Compared to the combustion of a fuel in a FF mode, owing to improved heat transfer by conduction, convection, and radiation, its combustion in a PM is advantageous. With flame stabilized in the mid-section, this fact is demonstrated in Fig. 2.4 that illustrates

heat release rate as a function of gas temperature. For different equivalence ratios φ, these comparisons are made for the combustion of LPG in the PM and in the FF mode. For a given φ, the maximum heat release rate and also the total amount of heat release rate for LPG combustion in the PM is much higher than its combustion in the FF mode. For $\varphi = 0.55, 0.7$ and 0.9, the maximum heat release rates for LPG combustion in the PIB are 2.68, 2.10 and 1.78 times, respectively higher than for the LPG combustion in the FF mode. It is further observed that when the equivalence ratio φ increases, with LPG combustion in PIB and FF mode, the total heat release rate increases. With the reaction zone stabilized in the mid-section of the PM, the mass flow rate of the fuel increases as φ increases, and this leads to increase in the volumetric heat generation.

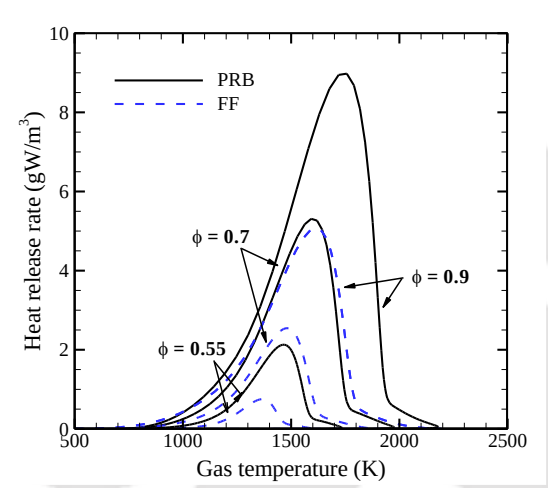

Fig. 2.4. Comparison of variations of heat release rate with gas temperature for PIB and FF combustion for equivalence ratios $\varphi = 0.55,\ 0.7$ and 0.9.

2.2.4. Stability range

Flashback and blowoff are two undesirable phenomena associated with gas burners. When the filtration velocity exceeds the incoming fuel-air mixture velocity, the flashback occurs. Blow off occurs when the velocity of the incoming fuel-air mixture exceeds the filtration velocity. Thus, stable operating range is an important aspect of combustion in a burner. In the present work, these results are presented in Figs. 2.5a, b. For the sake of comparison, results are presented for CH_4 and LPG combustion in the PM and FF mode.

Stable burner operating range for LPG and CH_4 combustion in the PM and FF mode in term of filtration speed and flow rate is shown in Figs. 2.5a, b respectively. For a certain

equivalence ratio φ, the filtration speed S_L attains its highest possible limit (HL) when it is stabilized in the midsection of the PM, and the lowest possible limit (LL) when it is stabilized at the upstream end of the PM. Flame inside the PM will experience blow off when V_0 exceeds the filtration velocity corresponding to the HL. Similarly, the flashback occurs when V_0 is below filtration velocity corresponding to LL of the stable operating range. Operation between the HL and LL gives the stable operating range of the burner.

Figure 2.5a shows the stable operating range in terms of filtration velocity V_0, while Fig. 2.5b shows the same in terms of flow rate $(\dot{m} = \rho V_0)$. The lean flammability limit (LFL) is the lowest equivalence ratio beyond which the flame cannot be self-sustained inside the PIB. With reference to Figs. 2.5a and 2.5b, $\varphi = 0.399$ is the LFL at which LPG flame stabilizes in the mid-section of the PIB at a flow rate of 0.09934 kg/m^2 s. While for CH_4, $\varphi = 0.43$ is the LFL at a flow rate of 0.08605 kg/m^2 s. In case of LPG combustion in the FF mode, this value is 0.456. This indicates that a leaner fuel-air mixture can have a stable combustion in the PIB.

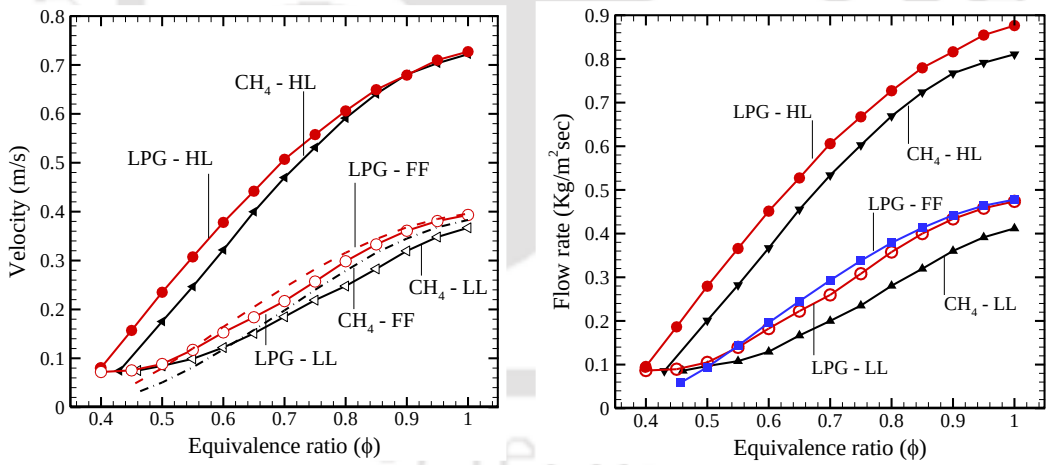

(a) (b)

Fig. 2.5. Comparison of stability range in terms of **(a)** flame speed and **(b)** firing rate of LPG and CH_4 combustion in the PIB.

It is observed from Figs. 2.5a and 2.5b that for both LPG and CH_4 combustion in the PIB, with an increase in equivalence ratio φ, the burner stable operating range also increases. However, the HL and LL of LPG are more than CH_4 combustion in the PIB. It is further observed that for the lean $(\varphi \leq 0.5)$ LPG-air mixture, both HL and LL are higher than the

laminar flame velocity V_{0L} for the FF combustion of LPG. With LPG combustion in the PIB, due to heat losses, flames at lower φ cannot stabilize close to the upstream end. But as φ increases, flames can be stabilized anywhere along the PIB, but their LL becomes lower than V_{0L} if they are very close to the entrance of the PIB. For higher φ, LL again approaches V_{0L}.

2.2.5. Heat flux

In combustion of a fuel in a PIB, stable reaction zone can be achieved in the bottom half portion of the PM. Radiant heat flux and the total flux do depend on the location of the reaction zone. For a given location of the reaction zone, radiant heat flux and the total heat flux vary with the equivalence ratio. These variations are shown in Figs. 2.6 and 2.7. Variations of radiant heat flux with the flame location for $\varphi = 0.6$, and with reaction zone located at the mid-section of the PM, variations with φ, are shown in Figs. 2.6a and 2.6b, respectively. These variations are shown for combustion of both LPG and CH_4 in the PM. It is observed from Fig. 2.6a that as the flame moves downstream, the filtration speed increases (Figs. 2.2a-d), leading to increase of solid-phase temperature (Figs. 2.2a-d), and consequently as observed, the radiant heat flux increases. At any location, the radiant output from LPG is more than that for CH_4. This is for the reason that the firing rate of LPG is more than that for CH_4, and this leads to enhanced heat generation, hence higher solid temperature and the radiant heat flux. From Fig. 2.6b, it is observed that for any value of φ, also the radiant heat flux with LPG is more than that for CH_4. This trend is also attributed to the fact that increase in the filtration velocity with increase in φ is more for LPG.

Variations of the total (conductive, convective and radiative) heat flux with the flame location for $\varphi = 0.6$ are shown in Fig. 2.7a. With flame located at the mid-section of the PM, the variations with φ are shown in Fig. 2.7b. For the purpose of comparison, variations of total heat flux are provided for both LPG and CH_4. Additionally, in Fig. 2.7b, the total heat flux variations for LPG and CH_4 combustion in the FF mode are also provided. As the flame location shifts downstream, the total heat flux increases. This is true for both LPG and CH_4. However, with LPG, the total heat flux is more than that for

CH_4. An observation of Fig. 2.7b shows that the total heat flux with LPG combustion in the PIB is much more than that of LPG combustion in the FF mode. With combustion in the PIB, this increase is owing to the improved heat transfer and stable combustion for a higher range of the firing rate. The total heat flux with LPG is also more than that for CH_4.

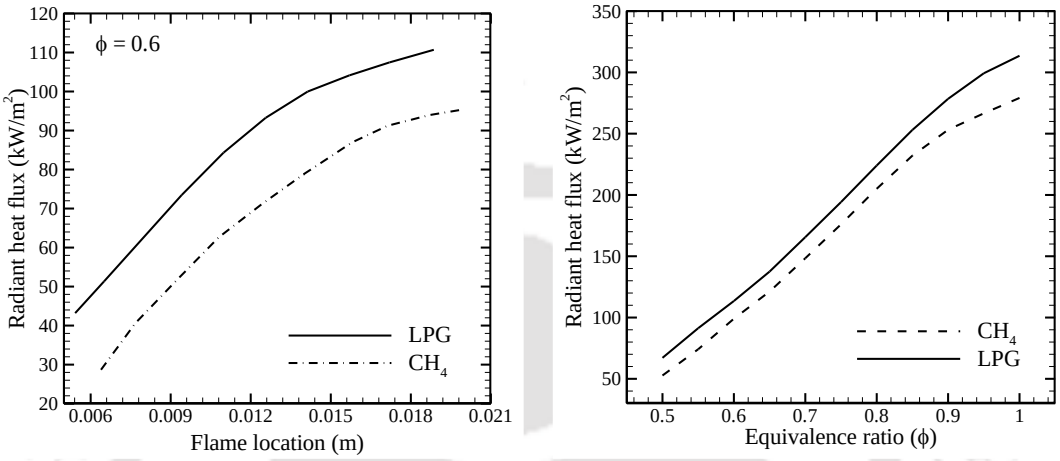

(a) (b)

Fig. 2.6. Comparison of variations of radiative heat flux due to combustion of CH_4 and LPG in PIB as a function of **(a)** flame location and **(b)** equivalence ratio.

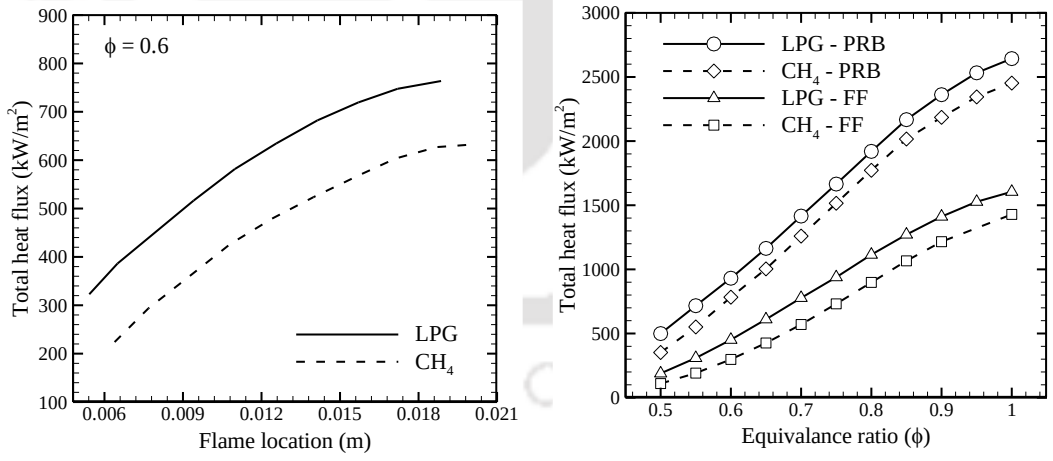

(a) (b)

Fig. 2.7. Comparison of variations total heat flux with **(a)** flame location and **(b)** equivalence ratio in the combustion of CH_4 and LPG in PIB.

2.2.6. CO emission

CO emission is one of the major concerns in combustion devices. Its presence in the exhaust gas, in one hand, indicates incomplete combustion, and on the other, its exposure

is bad for health. Thus, in combustion applications, estimation and minimization of CO level remain an important task. Combustion of a fuel in a PIB is known to not only increase the thermal efficiency but also to reduce CO emission. In Fig. 2.8a, CO concentrations profiles for LPG combustion in PIB along the axial direction at two locations are shown, whereas in Fig. 2.8b, equilibrium CO mass fraction from LPG and CH_4 combustion in PM and FF mode are compared.

In Fig. 2.8a, for equivalence ratio $\varphi = 0.9$, variations of CO mass fraction with axial distance are provided for flame stabilized at two locations, viz., mid-section and upstream of the mid-section of the PM. For the two locations, the corresponding burning velocities are 0.6768 m/s and 0.3609 m/s, respectively. It is observed that irrespective of the flame location, the production of CO is the highest at the reaction zone, and higher is the filtration velocity, higher is the peak magnitude of CO mass fraction.

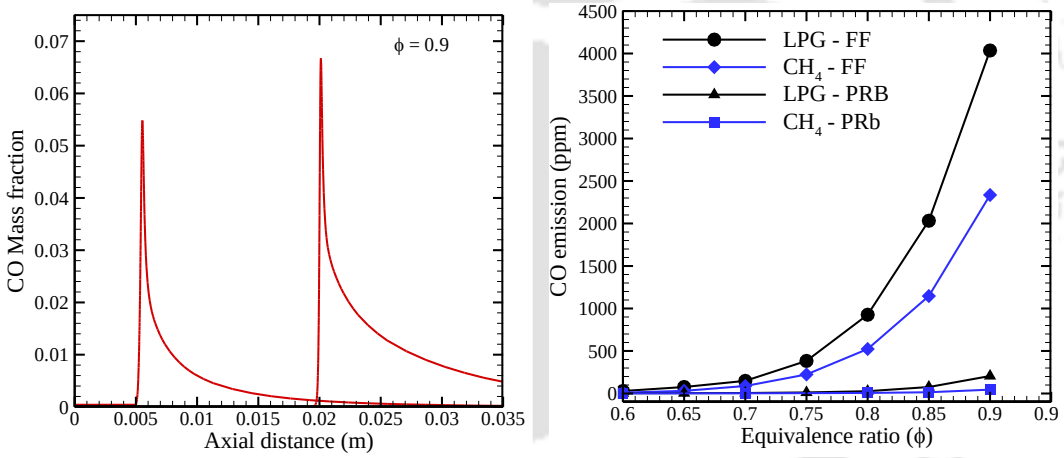

(a) (b)

Fig. 2.8. (a) Comparison of variations of CO mass fraction with the axial location, **(b)** Comparison of variations of CO emissions with equivalence ratio for combustion in PIB and in FF mode.

With flame located in the upstream, for LPG and CH_4 combustion in the PM, variations of CO emissions with equivalence ratio are compared with LPG and CH_4 combustion in FF mode in Fig. 2.8b. It is to be noted that the combustion of LPG-air mixture in the PIB and in the FF mode are calculated using equal domain length (0.03 m) with same fixed flame location. It is observed that the CO emission with LPG and CH_4 combustion in FF mode is much higher than that of combustion in the PIB. However, the CO concentration

calculated at the outer surface of the PIB is lower with CH_4 as compared to LPG. This is owing to the fact that LPG has higher carbon content than CH_4. For φ = 0.6-0.9, CO emission in LPG fired PIB is in the range of 2.86 - 205.81 ppm whereas that in LPG combustion in the FF mode, the same is 29.14 - 4035.66 ppm. With LPG combustion in PM, an average reduction of 1224.67 ppm in CO emission can be achieved, whereas an average reduction of 725.25 ppm can be achieved if CH_4 is allowed to combust in the PIB instead of its combustion in FF mode. This thus justifies combusting LPG in the PIB.

2.3. Summary

The premixed combustion of LPG-air mixture within a single-layer PIB was numerically analyzed. The contribution of the volumetric radiation was accounted, and the FVM was used to compute this information. With the solid-phase energy equation computed using the FDM, the species conservation equation, and the species diffusion and the heat generation terms appearing in the gas-phase energy equation were computed using the solver Cantera. Detailed chemical mechanisms with 111 species and 784 reactions were considered. Comparison of results from the present work showed an excellent agreement with those reported in the literature. In the parametric study, for the sake of comparison, results from LPG combustion in the PM and FF mode were compared with those of CH_4 combustion. LPG combustion in PM was found to have a higher operating range and radiative heat flux than that of CH_4.

CHAPTER 3

COMBUSTION OF LPG IN TWO-LAYER PIB

As technology advances, two-layer PIBs have shown better performances over single-layer PIBs [92] in terms of stability range, power density, and pollutant emissions. This Chapter devotes to the analyses of combustion of LPG inside a two-layer PIB for domestic cooking stove application. In this Chapter, the experimental setup used to study the combustion of gaseous fuels within the PIB is presented as well as the procedures followed throughout the experiments conducted for this thesis are described in details. The upstream section of the two-stage PIB is made of alumina balls with small pores, while the downstream section consists of a higher porosity SiC PM. The local quenching of flame caused by the sudden change in porosity at the intersection of the burner improves the stable operating range as compared to that achieved from a single-layer PIB.

The numerical modeling of the PIB provides the possible and optimum operating conditions for LPG stove. The formulation provided in the previous Chapter is first validated with the experimental data. In order to investigate the effect of the geometrical configuration of the two-layer PIB on the performance of the cooking stove, various stable operating conditions with thermal power input from 0.55 kW to 16.99 kW, and equivalence ratio in the range of 0.4-0.8 are considered. In addition, following guidelines of the WHO, the most effective burner on the basis of the minimum CO emission and the maximum thermal efficiency is proposed.

3.1. Experimental Setup and Procedure

The schematic diagram of the experimental set up [21] used for testing the performance of the PIB-based cooking stove is shown in Fig. 3.1. The PIB set up comprises a mixing chamber, a burner casing and two different porous layers, each 80.0 mm in diameter. The upstream section of the two-section PIB is made of Al_2O_3 spheres of 3 mm diameter supported on a wire mesh holder attached to the burner housing, while the downstream section consists of highly radiating and conducting SiC PM with 90% porosity. The air is supplied from an air compressor, and fuel is supplied from pressurized cylinder fitted with a pressure regulator. To achieve the required equivalence ratio, the flow rates of fuel and air are regulated by needle valves and monitored by Coriolis mass flow meters (accuracy ± 0.001 g) prior to entering the mixing chamber. The air and fuel are delivered at room temperature (298 K) and atmospheric pressure to the PIB through the mixing chamber of 50 mm inner diameter containing fine wire screens to promote proper mixing of the fuel-air mixture. To minimize the radiation loss, an adjustable stand with radiation shield is attached. Combustion starts at the interface of the two sections and spreads in the entire volume of the SiC. Due to the high surface area to volume ratio, high thermal conductivity and high emissivity of the PM, combustion remains fully submerged in the SiC matrix. The burner casing made of an insulating material prevents heat loss by conduction in the radial direction.

The temperature distribution profiles along the axial distance of the burner were measured using chromel-alumel and platinum-platinum/10% rhodium (*Pt-Pt*/10%*Rh*) thermocouples acquired through a data acquisition system. In order to measure the temperatures of the preheating zone and the combustion zone of the PIB, two chromel-alumel thermocouples were inserted in the Al_2O_3 layer (T_1 and T_2) and three *Pt-Pt*/10%*Rh* thermocouples were located within the SiC matrix (T_3, T_4, and T_5) at an interval of 10 mm along the burner, as shown in Fig. 3.1. The surface temperature of the burner was measured using the IR thermo-camera with spectral range of 7.5 µm-14 µm, and capable of measuring the temperature in the range of -40 °C to 2300 °C. CO concentration in the exhaust gas was measured by Greenline 8000 portable flue gas analyzer. The sampling was done as recommended in the Bureau of Indian Standard (BIS): 4246:2002.

For the desired equivalence ratio, stable operating ranges were obtained for which the combustion was stabilized within the PIB. The burner was allowed to operate for at least 30-minute period at a given test condition and temperature distributions were measured at regular interval to ensure that steady state had been achieved inside the PIB. Once stable combustion was established within the PIB for a given φ, the flow rates of fuel and air were simultaneously decreased stepwise while keeping the φ constant. This procedure was followed until the flame reached the location of the thermocouple probe T_1, where it attained the minimum stability limit (LL) and experienced flashback at that φ. Then the flow rate of the mixture increased step by step until the flame reached a higher limit (HL), where it experienced blow-off at the burner surface. This method was followed to determine the stable operating limits of the fuel-air combustion within the PIB stove.

Thermal efficiencies of PIB stoves were found by conducting the water boiling test as per the guidelines prescribed in the BIS:4246:2002. The method followed is briefly described in the following. Aluminum vessel along with a lid and a stirrer for the experiment were selected and filled with a known amount of water (5 kg) at room temperature. The weight of the vessel with water was noted with the help of a weighing balance (accuracy ± 0.5 g). The initial temperature T_i of the water was measured using a glass-in-mercury thermometer. Once the flame was stabilized, the vessel was kept above the burner. Water was heated up to 80°C, and for uniformity in temperature, stirring was started and continued until the end of the test when the temperature T_f of the water had reached 90±0.5°C. At that stage, the burner was switched off. The time taken to raise the temperature of the water from initial temperature T_i to 90°C was noted. In every case, experiments were repeated three times, and the average of three sets of data was taken for the analysis. The percentage of thermal efficiency $\left(\eta_{th} = \frac{\text{Heat output}}{\text{Heat input}} \times 100\right)$ of the stove was calculated based on BIS: 4246:2002 prescribed formula:

$$\eta_{th} = \frac{\left(m_w \cdot c_w + m_p \cdot c_p\right)\left(T_f - T_i\right)}{Q_{th}} \times 100 \tag{3.1}$$

where m_w is the mass of water, c_w is the specific heat of water, m_p is mass of the pan and c_p is the specific heat of the pan, $Q_{th}\left(= m_f \cdot Q_{LHV}\right)$ is the input thermal load, m_f is the

mass (flow rate × time) of the fuel consumed during the experiment and Q_{LHV} is the lower heating value of the fuel.

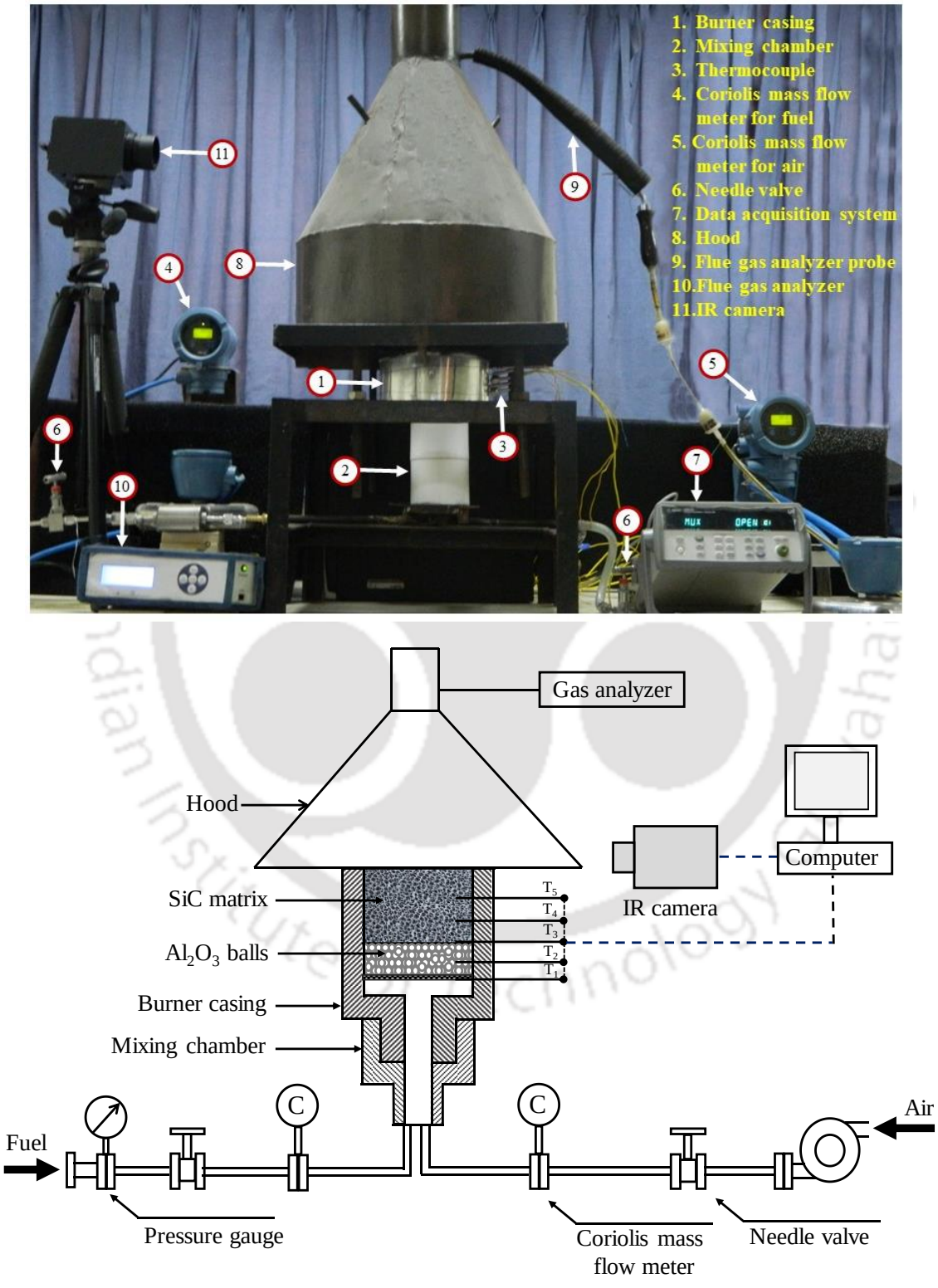

Fig. 3.1. Image and schematic diagram of the PIB setup.

3.2. Geometry and Numerical Model

A schematic of the PIB used for numerical study is shown in Fig. 3.2. The computational model includes a SiC section and an Al_2O_3 section. The air-fuel mixture enters the PIB through its bottom (x_{in}) surface. Combustion is initiated by a spark at the top (x_{out}) surface, and it stabilizes at the interface of the SiC matrix and Al_2O_3 section. Combustion of air-fuel mixture leads to the generation of heat and production of species. Heat generation at the intersection of the PIB gives rise to heat transfer by convection from the gas to the SiC matrix. The SiC being conducting and radiating, heat transfer by conduction and radiation manifests in the entire volume of the PM. Upstream of the interface, conduction and radiation elevates the temperature of the Al_2O_3 section, and through convective heat transfer, the incoming fuel-air mixture gets preheated. Downstream to the interface, owing to the additional contribution of energy transfer by advection, the gas temperature is more than that of the SiC PM, and, therefore, convective heat transfer takes place from the gas to the solid.

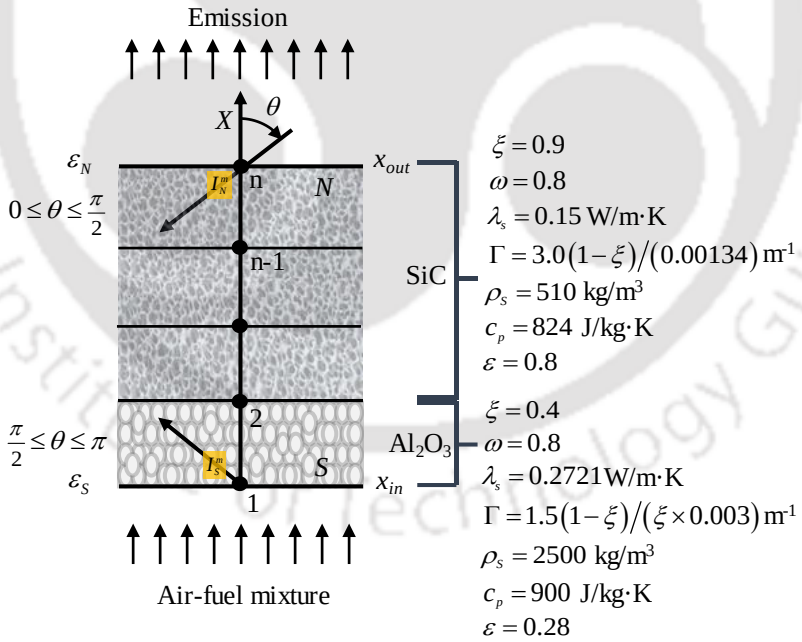

Fig. 3.2. Schematic diagram of the burner along with the material properties [94,95] used in the two-section PIB.

The FDM based complete local thermal non-equilibrium flow model to solve the macroscopic transport equations, boundary conditions, and solution methodology can be found in Chapter 2. The radiative flux appearing in the solid energy equation is calculated

using the FVM for solving the quasi-steady RTE. The convective heat transfer coefficient h_V for Al_2O_3 balls is obtained from Wakao and Kaguei [93],

$$\frac{h_V d_p^2}{\lambda_g} = 6\xi\left(2.0 + 1.1\mathrm{Re}^{0.6}\,\mathrm{Pr}^{1/3}\right) \tag{3.2}$$

where $\mathrm{Re} = \rho u d_p / \mu$ and $d_p = \dfrac{\sqrt{4\xi/\pi}}{\mathrm{PPC}}(\mathrm{cm})$

The material properties of the PIB are given in Fig. 3.2.

3.3. Results and Discussions

In the development of a PIB, thicknesses of SiC and Al_2O_3 sections are important factors that need to be fixed beforehand. In this respect, effects of five different thicknesses of the SiC matrix and the Al_2O_3 sections (Table 3.1) with various operating conditions on the performance of the LPG fired PIB in terms of temperature distributions, CO emissions and thermal efficiencies are investigated in this study.

Table 3.1. Specifications and nomenclatures of investigated cooking burners (CB)

Designation	Al_2O_3 thickness, mm	SiC thickness, mm
CB1	12	15
CB2	12	20
CB3	12	30
CB4	12	40
CB5	20	15

3.3.1. Validation

For $\varphi = 0.54$ and power input (Q_{th}) = 1.11 kW, comparisons of axial temperature distributions with experimental data for CB2 burner are shown in Fig. 3.3a. Figure 3.3b presents the predicted and measured surface temperatures as a function of Q_{th} for $\varphi = 0.5$. It is observed that the computed solid temperature distributions agree fairly well with the experimental data.

It is observed from Fig. 3.3a that at axial locations T_1, T_2 and T_3 (Fig. 3.1), differences in computed and measured temperatures are 50K, 35K and 10K, respectively. This has been

attributed to minor periodic fluctuations in thermocouple beads by the flow of air-fuel mixture. At location T_1, which is in the section (Fig. 3.1) made of alumina balls, the fluctuation is high. However, at the interface of the SiC and the Al_2O_3 section, the computed temperature is close to the measured temperature. As the air-fuel mixture moves downstream, due to the resistance of the PM, its velocity decreases, and hence at the interface (T_2) where the reaction starts, the fluctuation decreases. At the location T_3, close to the burner surface, the fluctuation is minimum, and the computed and measured temperatures are very close to each other.

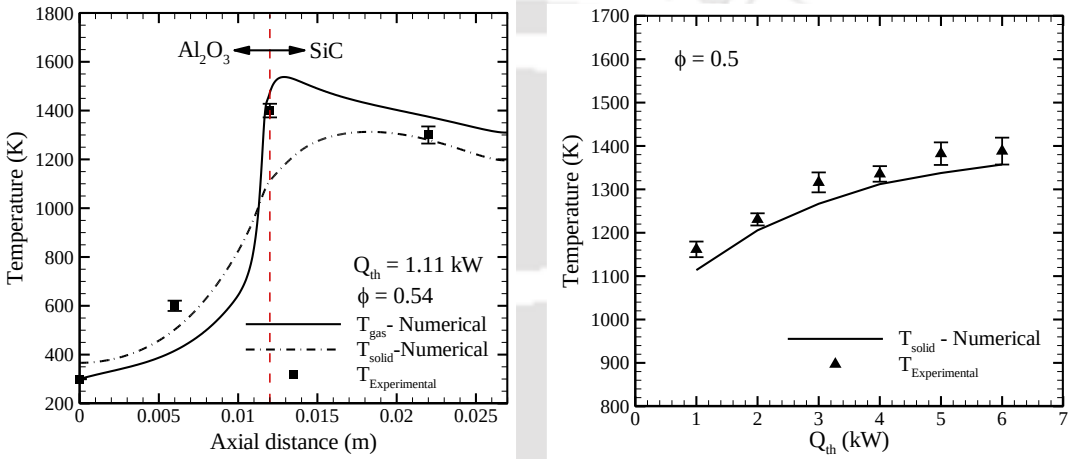

(a) (b)

Fig. 3.3. Predicted and experimental **(a)** axial temperature profile of the burner and **(b)** temperature at exit surface as a function of different operating conditions.

A comparison of computed and experimentally measured temperature at the top surface of the PIB is shown in Fig. 3.3b. For CB2 burner at $\varphi = 0.5$, this comparison is shown for thermal loads at six power inputs in range 1-6 kW. The surface temperature was measured by an infrared camera. It is observed that measured and computed temperature profiles compare well within an average error of 38.5K. It is observed that the surface temperature increases with increase in power input. At a given φ, with increase in power input, the mass flow rate of LPG-air mixture increases, and a higher volume of fuel is combusted, and this leads to an increase in surface temperature.

3.3.2. Effects of thicknesses of porous layers

For 5 sets of thicknesses (Table 3.1) of the Al_2O_3 and SiC sections, Tables 3.2-3.4 provide temperatures of solid at location T_1, flammability limit, and operating range,

respectively. In a premixed combustion, like the present one, preheating of the air-fuel mixture is desirable to improve burner's performance. With $\varphi = 0.5$ and Q_{th} = 5.0 kW, for burners CB1-CB4 (Table 3.1), computed and measured temperatures, and computed radiative heat flux at location T_1 (middle of the Al_2O_3 section) of the burner are provided in Table 3.2. With increase in thickness of the SiC stage, the radiative heat flux increases, and as a result, the preheating temperature also increases. At T_1, the measured preheat temperature for burner CB4 is 60.7K more than that of CB1, and the radiative heat flux is 55.85% more. A thicker SiC PM integrated burner increases radiation feedback to the preheating zone, which leads to an increase in preheating temperature. It is observed that the computed temperatures and the measured ones compare reasonably well.

Table 3.2. Preheating effect

Cooking burner types	Radiative flux at T_1 (MW/m^3)	Temperature (K) at T_1 ($\varphi = 0.5, 5.0$ kW)	
		Solid temperature (Numerical)	Experimental measurements
CB1	20.3943	453.785	488.8
CB2	26.6337	484.288	517.3
CB3	29.6526	506.573	532.7
CB4	31.7847	530.561	549.5

In Table 3.3, the LFL obtained for all (CB1 - CB5) PIBs are shown. The computed values match very well with the experimental data. Once the φ reaches the flammability limit inside the burner, the combustion process terminates. The LFL of $\varphi = 0.37$ is found for the burner CB1, which is in good agreement with the computed one $(\varphi = 0.36)$. By increasing thickness of the SiC matrix, it can be further lowered to 0.31(burners CB3 and CB4). However, LFL is relatively insensitive to the Al_2O_3 layer thickness.

Table 3.4 summarizes computed results of stable operating range for all burners for different Q_{th} and φ. For any burner, operating range in terms of thermal loads shifts to higher values as the φ increases from 0.4 to 0.8. Also at a constant φ, heat recirculation causes the operating range to increase for thicker burners.

Table 3.3. Flammability limit

Cooking stove types	Lean Flammability limit (φ)	
	Numerical	Experimental
CB1	0.36	0.37
CB2	0.31	0.34
CB3	0.29	0.31
CB4	0.28	0.31
CB5	0.34	0.36

Table 3.4. Operating range of various cooking burners

(φ)	Operating range (Q_{th}, kW)				
	CB1	CB2	CB3	CB4	CB5
0.4	0.62-1.65	0.68-2.27	0.55-3.23	0.55-3.23	0.55-3.10
0.5	0.77-5.15	0.85-6.01	3.0-6.18	3.26-5.75	2.57-4.29
0.6	5.13-8.31	5.64-9.24	6.16-9.44	6.16-9.75	4.92-8.41
0.7	8.47-11.70	8.95-12.77	8.95-12.77	9.55-13.49	8.47-11.70
0.8	12.10-15.63	12.91-16.59	12.91-16.59	13.19-16.99	12.23-15.63

3.3.3. CO emission of the burner

Thickness of the SiC matrix influences temperature of a PIB (Table 3.2), and therefore, it should also affect CO emissions. For burners CB1-CB4, this effect is shown in Figs. 3.4a-d for φ = 0.4, 0.6, 0.7 and 0.8, respectively. Effect of SiC zone thickness on CO emission is shown in Fig. 3.4a for φ = 0.4. For all thermal loads, CO emissions of CB3 and CB4 burners are found to be less than that of CB1 and CB2 burners. In cases of CB1 and CB2 burners, for low Q_{th}, high CO emission is due to less oxidation rate caused by low combustion temperature. For the CB1 burner, the CO emission decreases when Q_{th} increases. Whereas, for the CB2 burner, first CO emission decreases with increasing Q_{th} until emission reaches the minimum at the thermal input of about 1.0 kW. Up to 1.0 kW, the effect of higher oxidation rate due to increase in combustion temperature is causing a reduction in CO emission. For Q_{th} above 1.0 kW, CO emission increases. This is attributed to the fact that, for high Q_{th}, the residence time of the fuel-air decreases which

leads to an increase in CO emission. However, this same trend is not observed for CB3 and CB4 burners. For these two burners, the effect of higher residence time has a greater impact than low combustion temperature on CO emissions. So, the normal trend of increasing CO emissions can be seen with increasing Q_{th}. For $\varphi = 0.4$, CO emission levels for all types of burners are found to be between 0 and 5 ppm.

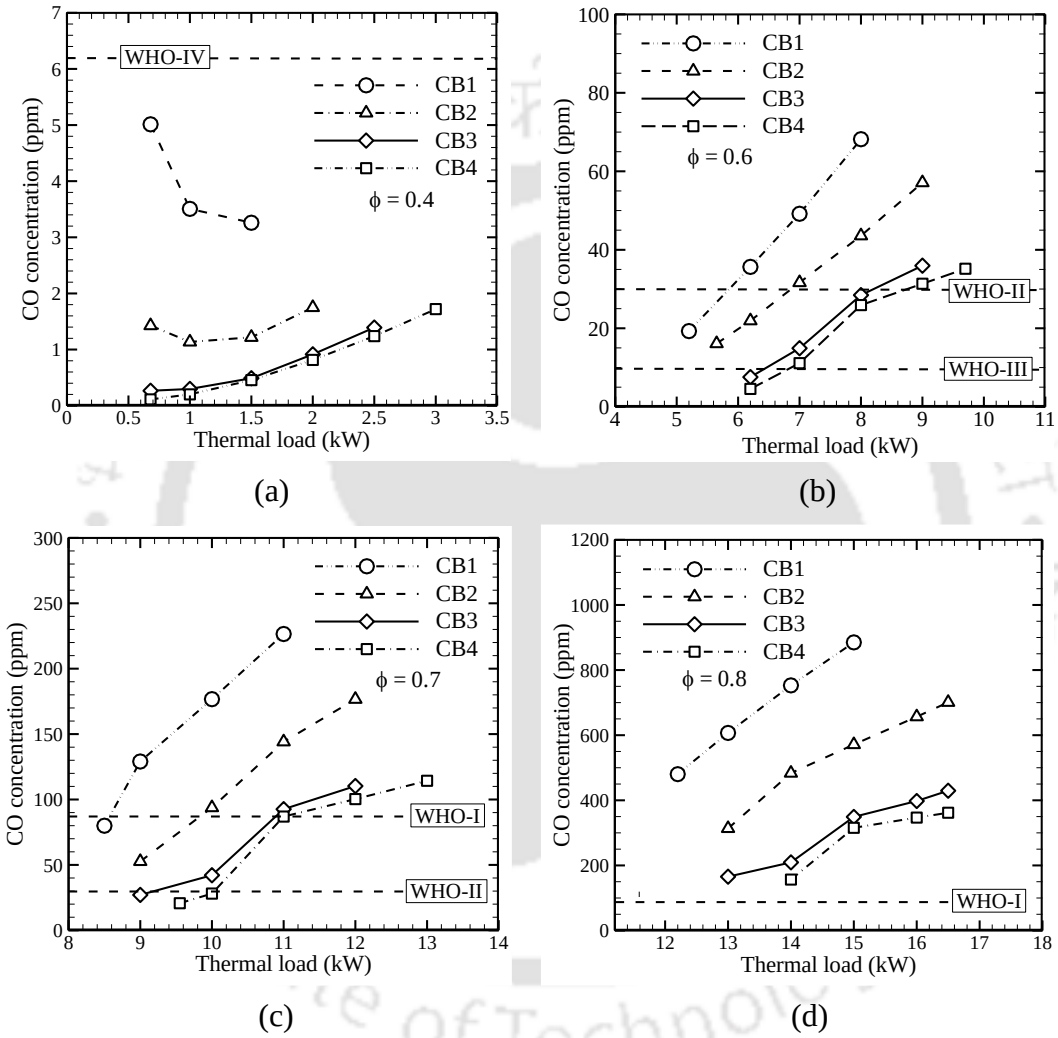

Fig. 3.4. Emission of CO as a function of Q_{th} and φ for various considered burners.

Computed profiles of CO emission are plotted in Figs. 3.4b-d for $\varphi = 0.6, 0.7 \text{ and } 0.8$, respectively. For any φ, it is observed that CO emission for any burner increases with increase in Q_{th}. Also, at any φ, higher the thickness of the SiC matrix, lower is the CO emission. This trend is attributed to the increase in the residence time with increase in the thickness. For example, the CO emission of CB2 burner integrated LPG stove is lower than that of CB1 burner. Similarly, the CO emissions from the stove with the CB3 and

CB4 burners are lower than the CO emission of the stove when CB1 and CB2 burners are used. In all cases, CO emissions of CB3 burner and the CB4 burner are nearly identical.

At $\varphi = 0.6$ and Q_{th} in the range 6.0-8.0 kW, CO emission is in the range 35-70 ppm for the CB1 burner, while for CB3 burner, the same is in the range 7-28 ppm (Fig. 3.4b). With CB3 burner, an average reduction of 67.7% can be achieved in CO emission. However, a small reduction in CO emission is observed between CB3 and CB4 burners. For a higher equivalence ratio $\varphi = 0.7,$ CO emissions are low for CB3 and CB4 burners. For an operating range of 9.0-11.0 kW, with the use of CB3 burner instead of CB1, an average reduction of 69.6% can be achieved in CO emission. A similar trend is observed for $\varphi = 0.8.$

To protect against adverse effects on health from CO exposure in indoor environment, WHO [96] has prescribed a regulation (Table 3.5). Conventional cooking stoves, in which combustion takes place in the gaseous environment, cannot comply to this guideline. However, a LPG cooking stove with a PIB can very well comply. Figure 3.4a indicates that the CO emissions of all the burners operating at $\varphi = 0.4$ are well below the emission standard permitted by WHO I-IV. At $\varphi = 0.6,$ and above 5.8 kW load (Fig. 3.4b), the CO emission for CB1 burner is more than the WHO-II restrictive limit. Whereas, for CB3 and CB4 burners, up to thermal load of 8 kW, the CO emissions are lower than the prescribed standards of WHO-II. From Fig. 3.4c, it is evident that, at $\varphi = 0.7,$ for all operating ranges, CB1 burner integrated cooking stove produces more CO emission than current standards of WHO-I (87.3 ppm). While for CB3 and CB4 burner, CO predictions are lower than WHO-I standard value up to a thermal input of 11 kW. Above 11.0 kW, CO emissions start to exceed the WHO-I limitation. Thus, from the point of view of CO emission, the CB3 burner is more desirable than the CB1 and CB2 burners. In Fig. 3.4d, results are shown for $\varphi = 0.8$ for a range of Q_{th} from 12-16.5 kW. In this operating range, CO emissions from all burners are above WHO standards. Thus, it can be concluded that to meet the prescription CO emission by WHO, a LPG stove with a PIB must operate below $\varphi = 0.8.$ Also, it is observed that compared to CB3, with CB4 burner, reduction in CO emission is not significant. Therefore, CB4 burner is not recommended.

To study the effect of thickness of the Al_2O_3 section on the CO emission, studies were made with CB1 and CB5 burners. While the thickness (15 mm) of the SiC PM is fixed, thickness of Al_2O_3 section for CB1 and CB5 are 12 mm and 20 mm, respectively. Figure 3.5 shows CO emissions of these burners as a function of thermal load for $\varphi = 0.6$. It is observed that the thickness of the preheating zone does not have a significant effect on CO emissions.

Table 3.5. Carbon monoxide guidelines by WHO [96]

Averaging time	Concentration (ppm)	Standard
15 minutes	87.3	WHO-I
1 hour	30.6	WHO-II
8 hours	8.73	WHO-III
24 hours	6.11	WHO-IV

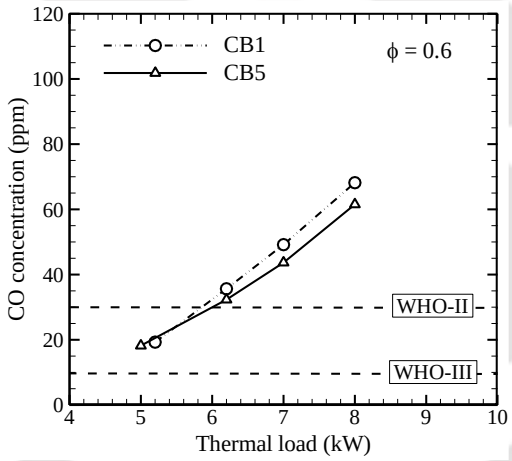

Fig. 3.5. Emission of the CO as function of Q_{th} for CB1 and CB5 burners.

A comparison of computed and measured CO emissions at the exit of CB1 and CB3 burners is shown Fig. 3.6a. The φ is kept constant at 0.5. Measured CO emissions are found more than the computed. This variation can be explained by inhomogeneous mixing of LPG-air mixture within the PIB, which leads to higher CO emission. Both numerical study and experimental measurements show that for higher burner thickness, the CO emission decreases. For all PIBs, for all φ and Q_{th}, NOx emissions were very low. Due to low combustion temperature inside the PIB, NOx emissions remained below 1.5 ppm for all the cases.

3.3.4. Thermal efficiency

Figure 3.6b shows the effect of SiC matrix thickness on experimentally measured thermal efficiency for LPG stove with CB1 and CB3 burners. Keeping φ constant at 0.5, thermal efficiencies were measured by varying Q_{th} in the range of 1-5 kW for CB1 and 3-5 kW for CB3. The thermal efficiency of CB3 burner is lower than that of the CB1 burner. This is due to the fact that, for a given Q_{th} and φ, the net radiation flux at the surface of burner decreases with increasing SiC thickness. The thermal efficiency of CB1 burner is found to be 1% - 2% higher than that of CB3 burner.

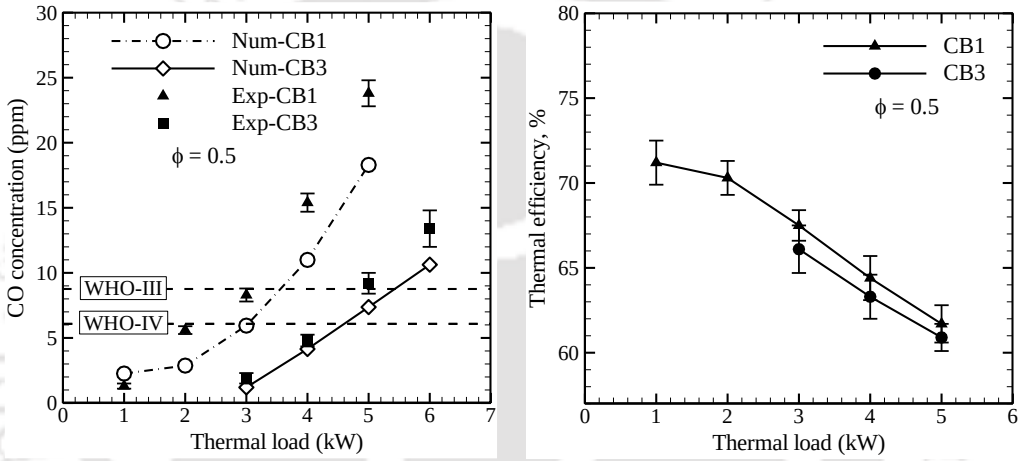

(a) (b)

Fig. 3.6. **(a)** CO emission and **(b)** thermal efficiency as a function of thermal input for CB1 and CB4 burners at $\varphi = 0.5$.

An observation of results on CO emissions presented in Figs. 3.4a-d and Fig. 3.6a shows that for all operating ranges, CO emission decreases with increase in burner thickness. Thus, from the standpoint of CO emission, CB3 burner is the most appropriate for LPG stove in an indoor environment. On the other hand, from results in Fig. 3.6b, it is found that the thermal efficiency of LPG stove decreases with increase in burner thickness. Therefore, from the standpoint of thermal efficiency, stove with CB1 burner is more desirable. Since the operating range and burner thickness affect the CO emission and thermal efficiency of a LPG stove, it is necessary to design the most appropriate burner for different operating conditions on the basis of minimum CO emission and maximum thermal efficiency. Thus, in the following, based on experimental and numerical analyses,

the most desirable burner considering various φ, high thermal efficiency and stringent emission standard limits is proposed.

It is observed from Fig. 3.4a that at low φ $(\varphi = 0.4)$, CO emissions from all four burners are below the WHO restrictive limit. Thus, considering high thermal efficiency (Fig. 3.6b) and emission standard limits permitted by WHO (Fig. 3.4a), it can be concluded that for lower φ, LPG stove with CB1 burner is the most effective. With reference to Figs. 3.4b-c, it has been mentioned previously that for all stable operating ranges obtained for φ above 0.4, CB1 integrated stove produces more CO emission than the current standard of air quality limit as compared to other burners. Therefore, it is concluded that for φ above 0.4, stove with CB3 burner is the most desirable from the standpoint of thermal efficiency and CO emission.

3.3.5. Effect of conductivity and scattering albedo

For a low φ $(\varphi = 0.4)$, considering efficiency (Fig. 3.6b) and CO emission (Fig. 3.4a), CB3 has been found to have an edge over other three other three PIBs. However, for $\varphi = 0.7$, and Q_{th} of above 11 kW, the CO emission for CB3 is found to be higher than the WHO-I restrictive limit (Fig. 3.4c). Can alteration of optical property, the scattering albedo ω and the transport property, the thermal conductivity λ_s of the material of the SiC matrix allow CB3 burner to operate within WHO-1 norm. If either the scattering albedo ω is reduced by 50% or the thermal conductivity is increased by 10 times, CO emission from CB3 burner over the complete range of thermal input comes fully under WHO-I emission limit. Figures 3.7a, b support these observations.

CO emission and radiative heat flux of a burner are interrelated. If CO emission comes down, the radiative heat flux goes up, and vice versa. Scattering albedo ω and thermal conductivity λ_s of the PIB have a favorable effect on lowering the CO emission (Figs. 3.7a and 3.7b). To understand qualitatively, how variation of radiative heat flux with thermal load is influenced, for $\varphi = 0.7$ and CB3 burner, results are provided in Figs. 3.7b and 3.7c. From these figures, it is observed that a decrease in ω and an increase in λ_s, have a favorable effect on CO emission. The observed trend is for the fact that a medium

with smaller scattering albedo ω absorb more radiative energy. This causes an increase in preheating temperature of the incoming LPG-air mixture, thus leading to a decrease in CO emission. With an increase in thermal conductivity, more energy is conducted from the SiC matrix to the preheat section. As a consequence, the incoming LPG-air mixture gets preheated at a higher temperature, causing a decrease in CO emission. Also with a decrease in ω and an increase in λ_s, the radiative and conductive heat transfer from flame front to its upstream and downstream section increases. This causes an increase in radiative heat flux at the burner surface (Fig. 3.7c, d), which ultimately leads to an increase in radiant efficiency of the stove. From the above discussion, it is concluded that a PIB with high thermal conductivity and low scattering albedo is more desirable from the point of view of CO emission and radiant efficiency.

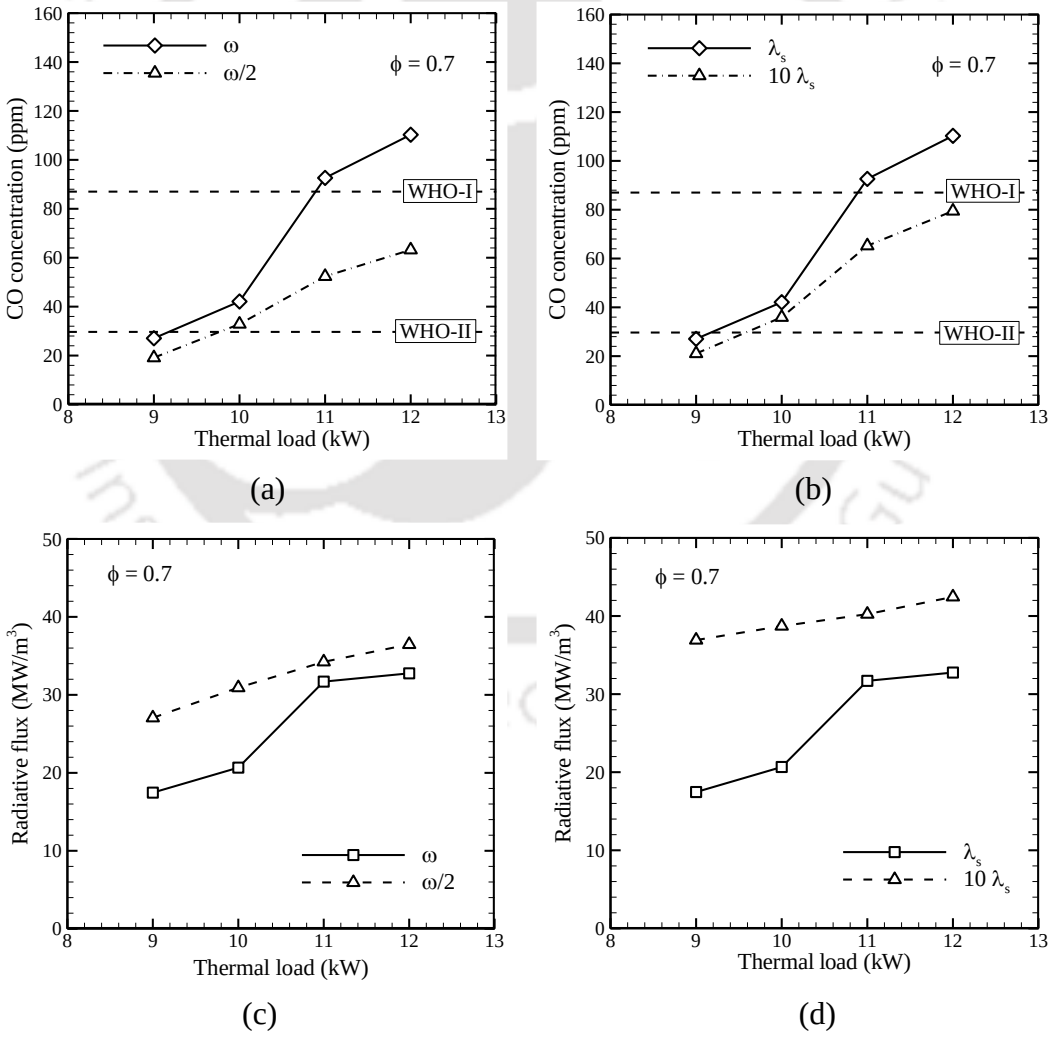

Fig. 3.7. Effect of ω and λ_s on the CO emission and radiative flux.

3.4. Summary

Combustion characteristics of LPG in a two-layer PIB stove were analyzed both computationally and experimentally. Performance of the PIB in terms of temperature distributions, CO emissions, thermal efficiency and radiative heat flux were studied for different geometric and operating parameters such as equivalence ratio, thermal load, thickness of the PIB, scattering albedo and thermal conductivity of the PM. To meet the accepted indoor air quality norms as prescribed by WHO, the most effective burner from the viewpoint of low CO emission and high thermal efficiency was also proposed.

CHAPTER 4

EFFECT OF DME ADDITION TO LPG FLAME

Worldwide, petroleum products have been used as the most conventional fuel in combustion devices. In particular, LPG is the most commonly used energy source in these devices. However, in developing countries, considering the increase in demand of LPG consumption and depleting fossil fuel reserves, there is a need to not only improve the thermal performances of existing LPG fired stoves, but at the same time extensive research is required to check the feasibility and flexibility of burning alternative energy sources like biofuel, methanol, dimethyl ether (DME), ethanol, hydrogen, and Fischer–Tropsch fuels in these improved burners. The nonpetroleum-based fuel DME has physical properties (Table 4.1) similar to those of LPG, and is considered as a renewable alternative to LPG because of its high oxygen level, high cetane number, low soot formation, and low emission.

During the last few decades, extensive research work has been done on the DME flame [97], and its additive with propene [98], methane [99], ethylene [100], hydrogen [101] and butane [102-104] combustion for premixed FF conditions. However, the effect of DME addition on LPG combustion under excess enthalpy combustion conditions achieved within the PIB has not been investigated. Thus the objective of this study is to analyze the behavior of the premixed DME-LPG-air flame inside the highly conducting

and radiating SiC-Al_2O_3 based PIB. Furthermore, to assess the advantage of LPG-DME combustion within PIB over FF combustion, computed results for premixed FF combustion at the same input conditions are also provided in this work. Flame behaviors of pure LPG, LPG-DME blend (50% - 50%), and pure DME within the PIB are studied for equivalence ratios in the range of 0.5-1.3. The addition of DME on premixed LPG-air combustion is studied under both fuel-lean and fuel-rich conditions to analyze the stable operating range, mole fraction profiles, and reaction rate of dominant reactions related to major flame species. To further interpret the effect of different DME fractions in LPG-DME fuel blend, pollutant emission, gas-phase and solid-phase temperature distributions, H_2-syngas production, as well as radical pool concentration and reaction zone thickness of the PIB are compared with those of pure LPG combustion.

Table 4.1. Physical properties of DME and LPG

Property	**DME**	**LPG**
Chemical formula	CH_3OCH_3	48% nC_4H_{10}, 25% iC_4H_{10}, 23% C_3H_{10}, 4% C_2H_6
Molecular weight (g/mol)	46.07	53.91
Maximum vapour pressure (kPa)	530	520
Heating value (MJ/kg)	28.8	46
Liquid density (kg/m^3)	667	540
Boiling point (°C)	-24.8	-22
Ignition point (°C)	350	488
Maximum flame speed (m/s)	0.47	0.409

4.1. Kinetic Model Selection

In order to precisely model the combustion mechanism inside the PIB, the detailed kinetic scheme used in the computation must be capable of predicting the laminar burning speed of LPG flame and DME flame over all equivalence ratios and preheating conditions relevant to the PMC. Therefore, in this work, first the predicted FF burning velocities of the following high-temperature kinetic models are compared to the available experimental data for LPG and DME combustion at elevated temperature conditions.

- NUIG Aramco Mech 1.3 [105], which consists of 1542 different elementary reactions and 253 chemical species.
- An extended kinetic model consisting of 836 elementary reactions and 128 different species resulting from the combination of the USC Mech 2.0 [91] model and the DME submodel based on Princeton-Zhao Mech [106].

In this work, the new model is referred to as "USC-Zhao Mech" model, in which the kinetics, thermodynamics and transport properties of C_1-C_6 hydrocarbon are taken from the extensively validated USC Mech 2.0 model. The DME sub mechanism, which consists of 52 elementary reactions and 17 chemical species, is incorporated into the USC Mech 2.0 core model. It is to be noted that the work in this thesis is not intended to develop a comprehensive kinetic mechanism; rather, a single kinetic model is created by combining different sub mechanisms available in the literature to predict the combustion characteristics of LPG/DME fuel blends.

In Figs. 4.1a and 4.1b the predicted FF burning velocities using the Aramco Mech 1.3 model and the new USC-Zhao Mech model are presented along with the published experimental data for LPG-air mixture [107] and DME-air mixture [108]. As no experimental data is available for the flame speed of LPG-DME blend, Figs. 4.1a, 4.1b only show the comparisons of the burning speeds for pure LPG and DME flames at ambient temperature and preheated temperature conditions. As shown in Fig. 4.1a, for LPG combustion, both models yield good agreement with the experimental data at all mixture temperatures. However, slight discrepancies among the simulated and experimental flame speeds are observed at a higher temperature of 600 K for both kinetic mechanisms. However, for pure DME flame, Aramco Mech 1.3 model over predicts the experimental data consistently over all temperature conditions (Fig. 4.1b). Especially at a higher temperature, Aramco Mech 1.3 mechanism shows over prediction for fuel-rich and stoichiometric conditions, whereas, with USC-Zhao Mech model, improvements in predictions of the burning speed can be observed as compared to Aramco Mech 1.3 model over all equivalence ratios and temperatures. From Figs. 4.1a and 4.1b, it is clear that the USC-Zhao Mech kinetic mechanism used in this work gives a better prediction of flame speeds for all conditions relevant to the PIB. Therefore, this model is used to investigate the chemical kinetic mechanism, sensitivity analysis and reaction pathway analysis for the combustion of LPG-DME-air mixtures within the PIB.

4.2. Results and Discussions

In the following, the formulation and kinetic model presented before is first validated with the experimental data. The stable operating ranges and temperature distribution of LPG-DME flames inside PIB, calculated using USC-Zhao Mech model are compared with the experiment results. In order to investigate the influence of DME addition to LPG on PMC, axial distributions of gas and solid phase temperature, mole fraction profiles and production rates of major flame species at different position of the burner and reaction zone thickness of the PIB with different DME fractions are analyzed in detail. Further to study the effect of DME addition on pollutant formation and burner reactivity, reaction pathways analyses and normalized sensitivity analyses are also presented. In addition, to assess the advantage of PIB, laminar FF combustion of LPG-DME-air mixture is also presented. In the present study, the volume fraction $\left(\alpha = \frac{V_{\mathrm{DME}}}{V_{\mathrm{DME}} + V_{\mathrm{LPG}}} \right)$ of DME in LPG-DME fuel blends (100% LPG/0% DME, 50% LPG/50% DME and 0% LPG/100% DME by volume) for various equivalence ratios in the range of 0.5 - 1.3 are considered.

4.2.1. Stable operating range of LPG-DME flame inside the PIB

In the two-layer PIB, stable combustion can be attained at the interface of the Al_2O_3 and SiC matrix. At the stable operating condition, the filtration velocity V_0 (m/s) is same as that of incoming LPG-DME-air mixture velocity and it is expressed as,

$$V_0 = \frac{\dot{V}_{LPG} + \dot{V}_{DME} + \dot{V}_{air}}{A_c} \tag{4.1}$$

where $\dot{V}$ is the volumetric flow rate of LPG, DME and air and A_c is the cross-section area of the PIB. The experimental uncertainty analyses are estimated using root sum square method, as proposed by Kline and McClintock [109]. The total uncertainty in filtration velocity is found to vary in the range between 1.9% to 9.8%, while the maximum uncertainty in the equivalence ratio is about ±0.005.

For a particular equivalence ratio φ, the V_0 achieves its HL at the downstream portion of the intersection, while the LL occurs at the upstream portion of the intersection of the PIB. Figures 4.1c-4.1e present the flame stability ranges for the LPG-DME fuel blends in

terms of V_0 for equivalence ratio in the range of $\varphi = 0.5-1.3$. The numerically predicted results using the USC-Zhao Mech model are presented along with the current experimental data. It can be seen that, for LPG-DME-air combustion inside the PIB, the USC-Zhao Mech model yields good agreement with the measured data. Furthermore, for the sake of comparison, available published data of FF burning speeds for LPG-air and DME-air mixtures are also presented in Figs. 4.1a and 4.1b respectively. Unlike the FF combustion, the heat recirculation process in PIB ensures stabilization of flame for a wide range of mixture flow rates and LPG-DME volume fractions (α) at a given φ.

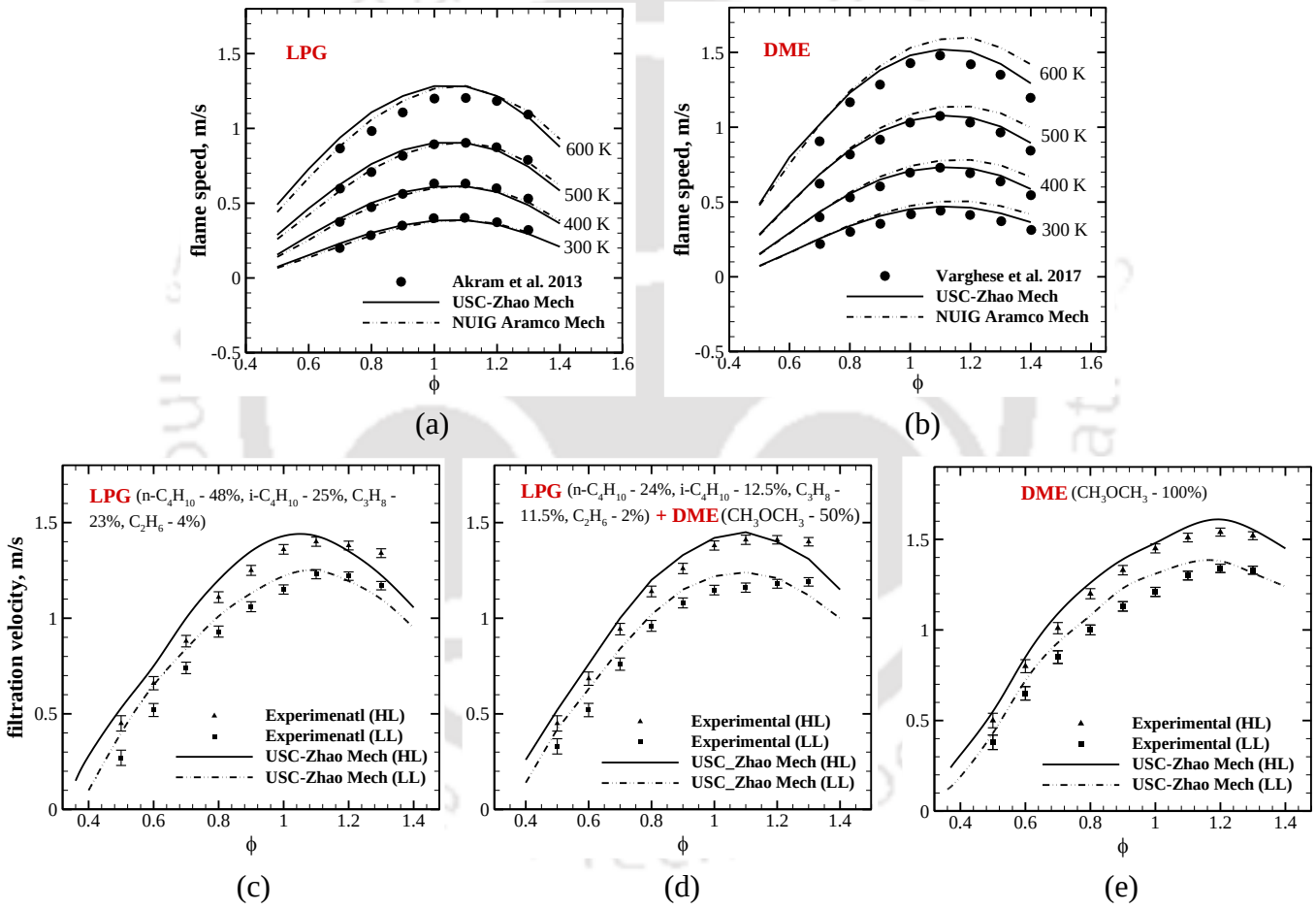

Fig. 4.1. Comparisons of the laminar burning speeds for **(a)** pure LPG flame and **(b)** pure DME flames over all φ and elevated temperature conditions, **(c)** experimental and numerical result comparisons of the flame stability ranges of the PIB for 100% LPG, **(d)** 50% LPG-50% DME, and **(e)** 100% DME flames.

As seen from Figures 4.1c-4.1e, at a given φ, with increase in DME concentration, the stable operating range of binary fuel-air mixtures further increases. For pure LPG

combustion, flame with the maximum filtration velocity of 140 cm/s can be stabilized in the PIB at $\varphi = 1.1.$ If instead of LPG, DME is allowed to combust in PIB, the highest HL increases to 159.0 cm/s. This is attributed to the fact that, with the addition of DME, the concentration of highly active free radicals increases (Fig. 4.2), leading to the faster oxidation rate within the burner, which ultimately increases the filtration velocity and thus the operating limits of the PIB. Moreover, the filtration velocities of LPG-DME-air flames within the PIB are more than their corresponding laminar flame speeds for any values of φ and α, as observed in Figs. 4.1c-4.1e. The highest measured filtration velocity of pure LPG-air flame within PIB is 100.0 cm/s more than that of FF mode, while for pure DME-air flame inside PIB, the maximum filtration velocity is found to be 114.0 cm/s higher than that of FF burning speed. Furthermore, from Fig. 4.1 it is observed that for wide variations of LPG-DME blend in the range of $\alpha = 0.0 - 1.0,$ combustion can be stabilized inside the PIB at the same fuel-air mass flow rate and equivalence ratio. In the following sections, experiments and computational studies are conducted by varying LPG-DME mixtures ($\alpha = 0.0$, 0.5 and 1.0), at fuel-lean condition $\varphi = 0.6,$ corresponding to the mixture mass flow rate of 0.9 kg/m^{2}s and at fuel-rich condition $\varphi = 1.3,$ corresponding to the mixture mass flow rate of 1.5 kg/m^2 s.

4.2.2. Effect of DME addition on temperature profiles and total heat release rate

To further explore the flame structure of LPG and DME mixtures ($\alpha = 0.0$, 0.5 and 1.0) inside the PIB, the T_g and T_s distributions of the burner at two different equivalence ratios $\varphi = 0.6$ and 1.3, corresponding to flow rate of 0.9 kg/m^2 s and 1.5 kg/m^2 s respectively, are studied here. In addition, the effect of DME volume fraction on the peak radical pool concentration in the PIB and FF at fuel-lean and fuel-rich condition is investigated in Fig. 4.2. Figures 4.3a and 4.3b present the axial temperature distributions of the PIB measured using the thermocouples at $\varphi = 0.6$ and $\varphi = 1.3,$ along with the predicted gas-phase and solid- phase temperature profiles for different DME volume fractions, while the zoomed view of the gas phase temperature profiles is illustrated in Fig. 4.3c. Comparisons of computed maximum solid temperatures of the PIB with experimentally measured data based on infrared camera are provided in Fig. 4.3d. It is observed that for all cases, the computed temperature profiles agree reasonably well with the experimental data.

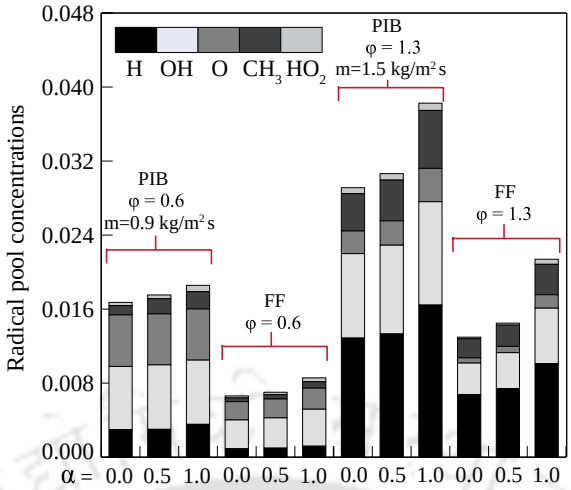

Fig. 4.2. Comparisons of the effect of α on the peak radical pool concentrations ($H+OH+O+CH_3+HO_2$).

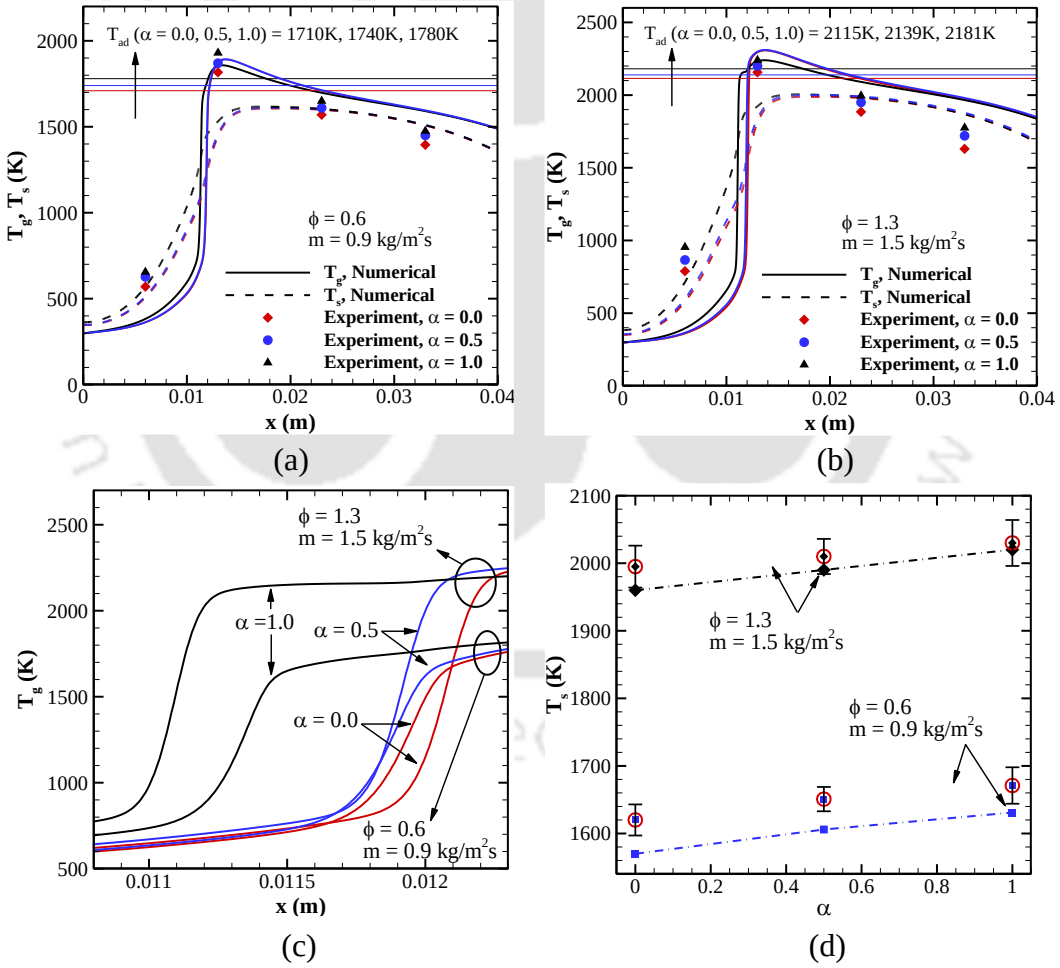

Fig. 4.3. Comparisons of measured and predicted axial temperature distributions of the PIB for **(a)** $\varphi = 0.6$ and **(b)** $\varphi = 1.3$, **(c)** zoomed view of T_g profiles for different φ and α, **(d)** comparisons of computed surface temperature with experimental data.

With reference to Fig 4.2, for a given φ and α, the total radical pool concentration produced during combustion inside the PIB is much higher than that of FF case, which ultimately increases the reaction zone temperature within the PIB. As seen in Figs. 4.3a and 4.3b, at the intersection of Al_2O_3 and SiC matrix the maximum measured and predicted gas temperatures are higher than their respective adiabatic FF temperatures, thus allowing the PIB to operate in an excess enthalpy combustion mode under both fuel-lean and fuel-rich conditions. Figure 4.3 a-c show that as the mass flow rate increases from 0.9 kg/m^2 s to 1.5 kg/m^2 s, the gas and solid temperatures increase for a given DME fraction. It is also observed that, at a given equivalence ratio and mass flow rate, with the increase of α, peak mole fractions of all free radicals increase (Fig. 4.2) leading to the promotion of oxidation rate inside the PIB. Furtherance of reaction rate causes the flame location to move the upstream region of the intersection of the PIB, as shown in Fig. 4.3c, and as a result, residence time of the hot combustion products inside the PIB increases, subsequently enhancing the convective heat transfer between gas and solid phases of the PIB. This leads to an increase in solid-phase temperature for the higher value of α at a given equivalence ratio and mass flow rate (Fig. 4.3d). Also with the increase in solid-phase temperature, the radiation feedback from the post-flame region to its upstream preheat region increases, thus leading to an increase in preheating temperature of the incoming fuel-air mixture. These observations can be comprehended from Figs. 4.3a and 4.3b, where the measured and predicted preheating temperatures at location T_2 are more for higher DME fractions. For the pure DME flame, the measured preheat temperature is found to be 85 K more than that of the pure LPG flame at $\varphi = 0.6$, while for $\varphi = 1.3$, a 62 K higher preheat temperature is observed for DME combustion within the PIB.

As discussed above, the excess enthalpy combustion can be achieved in the PIB because of improved heat transfer by conduction, convection, and radiation, and this causes higher heat release rate (*HRR*) at the reaction zone of the PIB as compared to the FF combustion. The comparisons of total heat release rate (*THRR*) due to combustion of different LPG-DME-air mixtures inside the PIB and their combustion in the FF mode are made in Fig. 4.4. For both fuel-lean and fuel-rich mixtures, for any value of α, the maximum heat release rate inside the PIB is found to be much higher than that of FF combustion. At $\varphi = 0.6$, and for $\alpha = 0.0$, 0.5 and 1.0, the *THRR* of LPG-DME-air combustion within

PIB is increased by 3465, 3580 and 3777 J/cm^3 s respectively compared to FF combustion. Similarly, at $\varphi = 1.3$, and for $\alpha = 0.0$, 0.5 and 1.0, the *THRR* for combustion within PIB is increased by 7986, 8324 and 8432 J/cm^3 s, respectively from their corresponding FF values.

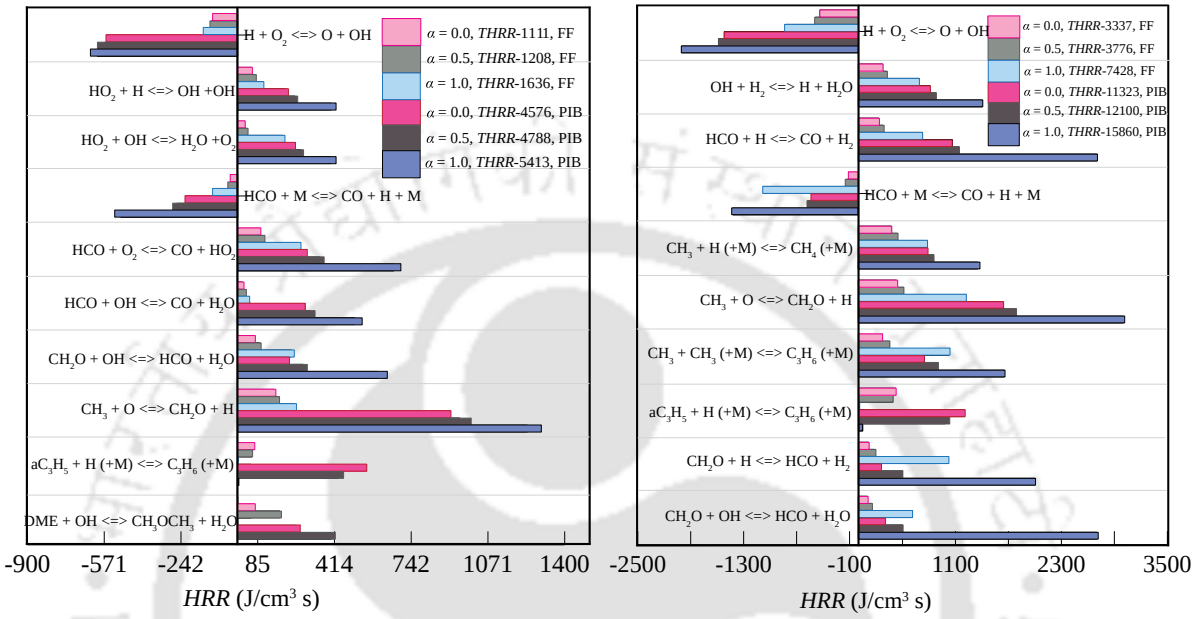

Fig. 4.4. Comparisons of *HRR* of major reactions for different α values for the PIB and FF cases at both **(a)** fuel-lean $(\varphi = 0.6)$ and **(b)** fuel-rich $(\varphi = 1.3)$ conditions.

In the case of DME combustion, higher temperature (Fig. 4.3) is due to high heat release rate caused by the increment of free radical pools within the PIB. Thus, in order to investigate the major exothermic and endothermic reactions responsible for the higher heat generation of the DME flame inside PIB, the *HRR* values for different LPG-DME blends at both fuel-lean $(\varphi = 0.6)$ and fuel-rich $(\varphi = 1.3)$ conditions are illustrated in Figs. 4.4a and 4.4b. For all the cases, the chain branching reaction $CH_3 + O \rightleftarrows CH_2O + H$ is the most exothermic, contributing significantly to the *THRR*, while $H + O_2 \rightleftarrows O + OH$ is the most endothermic reaction, which consumes a substantial amount of heat to generate O and OH free radicals. It is also observed that with an increase in DME fraction α, contribution of the reactions involving methyl radical (CH_3), formyl radical (HCO) and formaldehyde (CH_2O) to the overall heat release rate increases, resulting in higher heat generation than that of pure LPG flame inside the PIB. An observation of Fig. 4.4 shows

that, for $\varphi = 0.6,$ with DME combustion inside the PIB, the percentage contributions of reactions HCO + O_2 ⇄ CO + HO_2 and CH_2O + OH ⇄ HCO + H_2O to the overall heat release rate are increased by 7.0 % and 8.0 % as compared to their contributions for LPG flame within the PIB. Similarly, for $\varphi = 1.3,$ with the use of DME instead of LPG in the PIB, the contributions of reactions CH_2O + H ⇄ HCO + H_2, CH_3 + O ⇄ CH_2O, CH_3 + CH_3 (+M) ⇄ C_2H_6 (+M) and CH_2O + OH ⇄ HCO + H_2O to the overall heat release rate are increased by 10.0 %, 4.0 %, 5.0 % and 6.0% respectively.

4.2.3. Reaction mechanism of various LPG-DME blend flames inside the PIB

The detailed oxidation mechanisms of premixed DME-air and LPG-air flames in FF mode have been reported in various previous research works [97], [102], [104], [106] and [115]. However, no studies were reported to understand the effect of the DME addition on LPG flame behavior under excess enthalpy combustion condition attained within the PIB. Thus in order to investigate the effects of DME addition on the reaction mechanism of the LPG combustion in excess enthalpy combustion mode, concentration profiles and ROP analyses of neat LPG, LPG-DME blend (50% - 50%) and neat DME flames inside the PIB for the fuel-lean $(\varphi = 0.6)$ and fuel-rich $(\varphi = 1.3)$ condition are shown in Figs. 4.5-4.10. Moreover, for the purpose of comparison, computed mole fraction profiles of the major intermediate species for premixed FF combustion are also provided at the same input conditions. It is to be noted that the mole fraction profiles of LPG-DME-air combustion in the PIB and in the FF are compared by aligning the reaction zone such that maximum gradient of the T_g profiles are at the same position. In addition, Fig. 4.11 illustrates the main reaction paths of LPG and DME decomposition within the PIB.

The results suggest that at a fixed mass flow rate and equivalence ratio, with increase in DME concentration the species concentration profiles shift to the upstream region of the interface of the Al_2O_3 and SiC section. For all cases (fuel-rich and fuel-lean), LPG and LPG/DME mixture combustion reactions dominate at the intersection of the burner, while pure DME combustion reaction dominates in the Al_2O_3 section of the burner. For pure DME flame, the reactants are consumed completely in the Al_2O_3 section of the burner (Fig. 4.5a). This is due to the furtherance of the reaction rates and higher filtration velocity of DME than that of LPG, as discussed before. It can be seen from Fig. 4.5b that

the C_4 hydrocarbons, C_4H_{10} and iC_4H_{10} dissociate before the C_3 (C_3H_8) hydrocarbon. Then the oxygenate reactant (CH_3OCH_3) dissociates followed by the C_2 (C_2H_6) hydrocarbon.

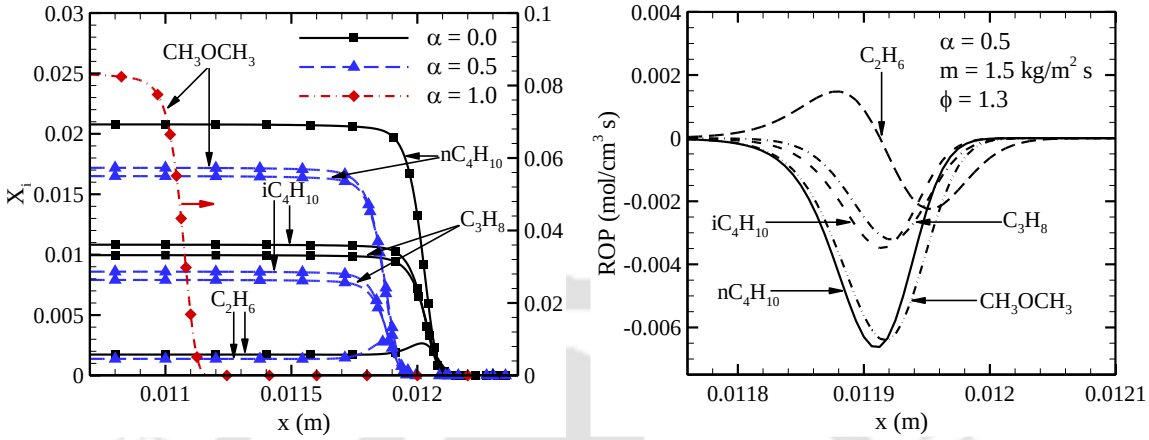

Fig. 4.5. **(a)** Mole fraction profiles and **(b)** ROP analysis of fuel reactants for different LPG-DME mixtures inside the PIB for $(\varphi = 1.3)$

Modeling results show that for the lean LPG-DME flames ($\alpha = 0.0$, 0.5 and 1.0) within the PIB, at $T_g \approx 970$ K and $T_s \approx 1190$ K, the concentration of fuel is ≈ 80% that of entering the burner. In the case of rich mixtures, the corresponding mole fraction of fuel is approximately 90% of that of inlet fuel concentration. Here the oxidation reaction starts at 0.2-0.3 mm close to the intersection of the Al_2O_3 and SiC region in both LPG and LPG/DME flames. Whereas, for pure DME flames, fuel decomposition starts within Al_2O_3 section, 0.9-1.0 mm further from the intersection (Fig. 4.5a). With reference to Fig. 4.11, the oxidation reaction of LPG is initiated by hydrogen abstraction of n-butane (nC_4H_{10}) to produce secondary butyl (sC_4H_9) radical and n-butyl (pC_4H_9) radical, via H atom, OH and O radicals. When n-butane is present in the fuel, sC_4H_9 becomes more abundant than pC_4H_9. This is due to the higher bond dissociation energy of primary hydrogen atoms than that of secondary hydrogen atoms. Iso-butane also undergoes hydrogen abstraction reaction by H, O and OH radicals to form tertiary butyl (tC_4H_9) and iso-butyl (iC_4H_9). At this location of PIB, where the gas phase temperature is close to 970 K, the DME oxidation process initiated by H-atom abstraction reaction forming methoxymethyl radical (CH_3OCH_2).

C_4H_{10} + (H, OH, O) ⇄ sC_4H_9 + (H_2, H_2O, OH)

C_4H_{10} + (H, OH, O) ⇄ pC_4H_9 + (H_2, H_2O, OH)

iC_4H_{10} + (H, OH, O) ⇄ tC_4H_9 + (H_2, H_2O, OH)

iC_4H_{10} + (H, OH, O) ⇄ iC_4H_9 + (H_2, H_2O, OH)

CH_3OCH_3 + (H, OH, O, CH_3) ⇄ CH_3OCH_2 + (H_2, H_2O, OH, CH_4)

In the case of fuel rich LPG flame, a small amount of C_4H_{10} is consumed by unimolecular decomposition, generating n-propyl (n-C_3H_7) and CH_3 radical, via C_4H_{10} (+M) ⇄ nC_3H_7 + CH_3 (+M). Propane (C_3H_8) is mainly consumed by O and H atoms to form n-C_3H_7 and iC_3H_7 radicals.

C_3H_8 + (O, H) ⇄ nC_3H_7 + (OH, H_2)

C_3H_8 + H ⇄ iC_3H_7 + H_2

At this location, further dissociation of sC_4H_9 and iC_4H_9 yields propene (C_3H_6) through *β*-scission reactions, via sC_4H_9 (+M) ⇄ C_3H_6 + CH_3 (+M), and iC_4H_9 (+M) ⇄ C_3H_6 + CH_3 (+M). The resultant C_3H_6 undergoes the H-abstraction reaction generating allyl radical (aC_3H_5), which forms allene (aC_3H_4), via aC_3H_5 ⇄ aC_3H_4 + H. 2-Butene (C_4H_8-2) is formed from the decomposition reaction of sC_4H_9 radical. The resultant 2-butene generates methylallyl radical (C_4H_7), which decomposes to 1,3-butadiene (C_4H_6), through C_4H_7 ⇄ C_4H_6 + H. nC_3H_7 is consumed by *β*-scission reaction to produce ethylene (C_2H_4) and CH_3 through nC_3H_7 (+M) ⇄ C_2H_4 + CH_3 (+M). Similarly, pC_4H_9 undergoes decomposition reaction to form ethylene (C_2H_4) and ethyl radical (C_2H_5), via pC_4H_9 (+M) ⇄ C_2H_4 + C_2H_5 (+M).

In the case of DME blended flames, the intermediate reactions observed in the Al_2O_3 section, at $T_g \approx 970$ K are similar to the low-temperature reactions reported in ref. [106]. At this location, a small amount of methoxymethyl-peroxy ($CH_3OCH_2O_2$) is formed from the methoxymethyl radical through CH_3OCH_2 + O_2 ⇄ $CH_3OCH_2O_2$, which, in turn, isomerizes to hydroperoxy-methoxymethyl radical by $CH_3OCH_2O_2$ ⇄ $CH_2OCH_2O_2H$. Subsequently, the resultant $CH_2OCH_2O_2H$ radical decomposes via *β*-scission reaction $CH_2OCH_2O_2H$ ⇄ CH_2O + CH_2O + OH.

The mole fraction of ethane (C_2H_6) attains its peak at $T_g \approx 1160$ K and $T_s \approx 1217$ K for all the lean mixture flames and at $T_g \approx 1290$ K and $T_s \approx 1522$ K for all rich mixture flames

inside the PIB. Here, the concentration of LPG/DME reactant is around 56% of that of incoming fuel. The recombination reaction of nearly half of the methyl radicals, CH_3 + CH_3 (+M) ⇄ C_2H_6 (+M), results in higher concentration of ethane than that of its inlet value (Fig. 4.6). The ethane is then consumed by H, O and OH radicals through hydrogen abstraction reaction to form ethyl (C_2H_5). At this location, the remaining half of the methyl radical reacts with HO_2 to produce methoxy radical via CH_3 + HO_2 ⇄ CH_3O + OH.

At a location close to the intersection of the two layers inside PIB, where the concentration of reactant mixture is around 23% and 13% of that of inlet values for lean and rich mixture flames respectively, formaldehyde (CH_2O) and methane (CH_4) attain their peak. Here, $T_g \approx 1310$ K and $T_s \approx 1232$ K for fuel-lean flame and $T_g \approx 1530$ K and $T_s \approx 1539$ K for fuel-rich mixture flames. In this region, methane is mainly generated through CH_3 + H (+M) ⇄ CH_4 (+M) and subsequently consumed by hydrogen abstraction reaction, via CH_4 + (H, OH) ⇄ CH_3 + (H_2, H_2O). If DME is present in the fuel, large parts of methane are formed through H-abstraction reaction from CH_3OCH_3, via CH_3OCH_3 + CH_3 ⇄ CH_4 + CH_3OCH_2 (Fig. 4.9). The resultant methoxymethyl radical is then consumed by β-scission reaction CH_3OCH_2 ⇄ CH_2O + CH_3, yielding formaldehyde and methyl radical. At this location, C_2H_5 radical undergoes hydrogen abstraction reaction to generate Ethylene (C_2H_4). This C_2H_4 is then consumed by hydrogen abstraction reaction to form vinyl radical (C_2H_3). Some of the C_2H_4 reacts with O radical to form methyl and formyl radical (HCO). The methyl radical is primarily consumed by oxygen atom to generate formaldehyde through CH_3 + O ⇄ CH_2O + H and secondarily reacts with hydroxyl radical through CH_3 + OH ⇄ CH_2(s) + H_2O, yielding singlet methylene radical (CH_2(s)). The CH_2(s) subsequently reacts with other molecules to generate more stable triplet methylene (CH_2). The resultant CH_2 reacts with O_2 to produce HCO. Formyl radical is also generated by hydrogen abstraction of formaldehyde, via CH_2O + (H, O, OH) ⇄ HCO + (H_2, OH, H_2O), which, in turns reacts with O_2 (HCO + O_2 ⇄ CO + HO_2) or decomposes to carbon monoxide (HCO + M ⇄ H + CO + M).

It is well-known that, in fuel-rich flames, acetylene (C_2H_2) and propagyl (C_3H_3) are important intermediates, which act as soot precursors for the formation of aromatic rings and PAHs [110]. For rich LPG flame and LPG-DME blend flame, most of the reactions

related to C_2H_2 occur at downstream section of the intersection of the two-layer PIB, where it reaches its peak at a gas phase temperature of $T_g \approx 1815$ K. The acetylene is mainly formed from the vinyl (C_2H_3) and propyne (pC_3H_4) radicals, via

$C_2H_3 (+M) \rightleftarrows C_2H_2 + H$

$C_2H_3 + H \rightleftarrows C_2H_2 + H_2$

$pC_3H_4 + H \rightleftarrows C_2H_2 + CH_3$

C_2H_2 is consumed by reaction with oxygen atom to produce ketenly radical (HCCO). The resultant ketenly radical may react with H atom producing carbon monoxide, via HCCO + H $\rightleftarrows$ $CH_2(s)$ + CO, which has a significant contribution to CO formation in fuel-rich flames. The propagyl radicals (C_3H_3) are generated from the reaction of acetylene with $CH_2(s)$ or CH_2 through the reaction $C_2H_2 + CH_2(s) \rightleftarrows C_3H_3 + H$ and $C_2H_2 + CH_2 \rightleftarrows C_3H_3 + H$. The other routes for the production of C_3H_3 are through the isomers of C_3H_4, via $aC_3H_4 + OH \rightleftarrows C_3H_3 + H_2O$ and $pC_3H_4 + OH \rightleftarrows C_3H_3 + H_2O$.

Finally, the propagyl radical formed before recombines to produce benzene (C_6H_6). The resultant C_6H_6 may undergo H-abstraction reaction to produce phenyl radical (C_6H_5) via $C_6H_6 + (H, OH) \rightleftarrows C_6H_5 + (H_2, H_2O)$, which in turn, reproduce benzene through, $C_6H_5 + H (+M) \rightleftarrows C_6H_6 (+ M)$ and $C_6H_5 + H_2 \rightleftarrows C_6H_6 + H$. The other important path for the formation followed by destruction of C_6H_6 is through the C_4H_5-2 radical: C_4H_5-2 + C_2H_2 $\rightleftarrows$ C_6H_6 + H. Some of the phenyl radicals are consumed by reaction with O_2, producing phenoxyl radical (C_6H_5O). Thermal decomposition of phenoxyl radical tends to the formation of cyclopentadienyl radical (C_5H_5), via $C_6H_5O (+M) \rightleftarrows C_5H_5 + CO (+M)$. The resultant C_5H_5 radical then reacts with H atom to generate cyclopentadiene (C_5H_6), through $C_5H_5 + H (+M) \rightleftarrows C_5H_6 (+M)$, which may reproduce C_5H_5 through, $C_5H_6 + H \rightleftarrows C_5H_5 + H_2$.

Eventually, for LPG and LPG-DME flames, the fuel gets almost consumed at the SiC section of the burner, where the gas phase temperature reaches $T_g \approx 1624$ K for lean flame and $T_g \approx 2150$ K for the fuel-rich flame. Whereas, for pure DME lean and rich flames, complete consumption of fuel takes place within the Al_2O_3 section of the burner at gas phase temperature of $T_g \approx 1592$ K and $T_g \approx 2025$ K, respectively. At this position,

for all the flames, CO reaches its peak and is eventually consumed by reaction with hydroxyl to produce carbon dioxide and hydrogen atom.

4.2.4. Species concentration Profiles and ROP analysis

To study the effect of DME addition on the LPG combustion within PIB, mole fraction profiles of the major intermediate flame species like CH_3, CH_2O, C_2H_2, C_3H_3, CH_3CHO, C_2H_6, CH_4, CO, C_6H_6, C_6H_5, C_5H_5, and C_5H_6 are analyzed in this section. To identify dominant reactions responsible for the formation and destruction of these species, the ROP of important reactions are also studied in Figs. 4.8-4.10. At $\varphi = 0.6$ (m = 0.9 kg/m^2 s) and $\varphi = 1.3$ (m = 1.5 kg/m^2 s), comparisons of computed axial mole fraction profiles and production rates of flame species in the PIB and FF combustion reaction are presented in Figs. 4.6-4.10 for different DME fractions, $\alpha = 0.0, 0.5$ and 1.0. It can be seen from Figs. 4.6-4.7 that, in the PIB the peak mole fraction of all the intermediate species exhibit higher values as compared to their respective FF species profiles. It is also observed that for all the cases PIB have narrower species profiles than that of FF, which is owing to the fact that flames within the PIB have thinner reaction zone width than FF, as discussed in section 4.2.8. In all the flames, CH_3, CH_2O, C_2H_6, CH_4, and CO are major chemical species, but C_2H_2, C_3H_3, C_6H_6, C_6H_5, C_5H_5, and C_5H_6 play an important role only in rich flames.

Among the reactants present in the parent fuel mixture, ethane is consumed last. Although ethane is a reactant in the fuel, within the PIB it acts as an intermediate species in the chemical reaction, as seen in Figs. 4.6a and 4.7a. This is mainly due to the recombination reaction of methyl forming ethane, via $CH_3 + CH_3 (+M) \rightleftarrows C_2H_6 (+M)$. However, it is not the case for lean LPG-air mixture in FF combustion (Fig. 4.6a), due to unavailability of enough CH_3 for the recombination reaction. The recombination reaction of methyl is also responsible for the higher concentration of C_2H_6 in the DME blended fuel. Figures 4.6b-c and 4.7b-c provide concentration variations of CH_3 and CH_2O for different DME fractions along the axial distance of the PIB. The dominant reactions responsible for CH_3 and CH_2O formations are shown in Fig. 4.8. It is observed that in fuel-rich flames higher amounts of methyl and formaldehyde are predicted as compared to the lean flames. This is due to the presence of lower amounts of O, OH and HO_2 radicals in rich flames, which reduces the consumption of CH_3 and CH_2O. As expected,

the addition of DME in LPG fuel increases the CH_3 concentration. It is evident that, for combustion inside the PIB, the lean LPG flame generates the lowest CH_3 mole fractions, whereas CH_3 concentration is highest in rich DME flame.

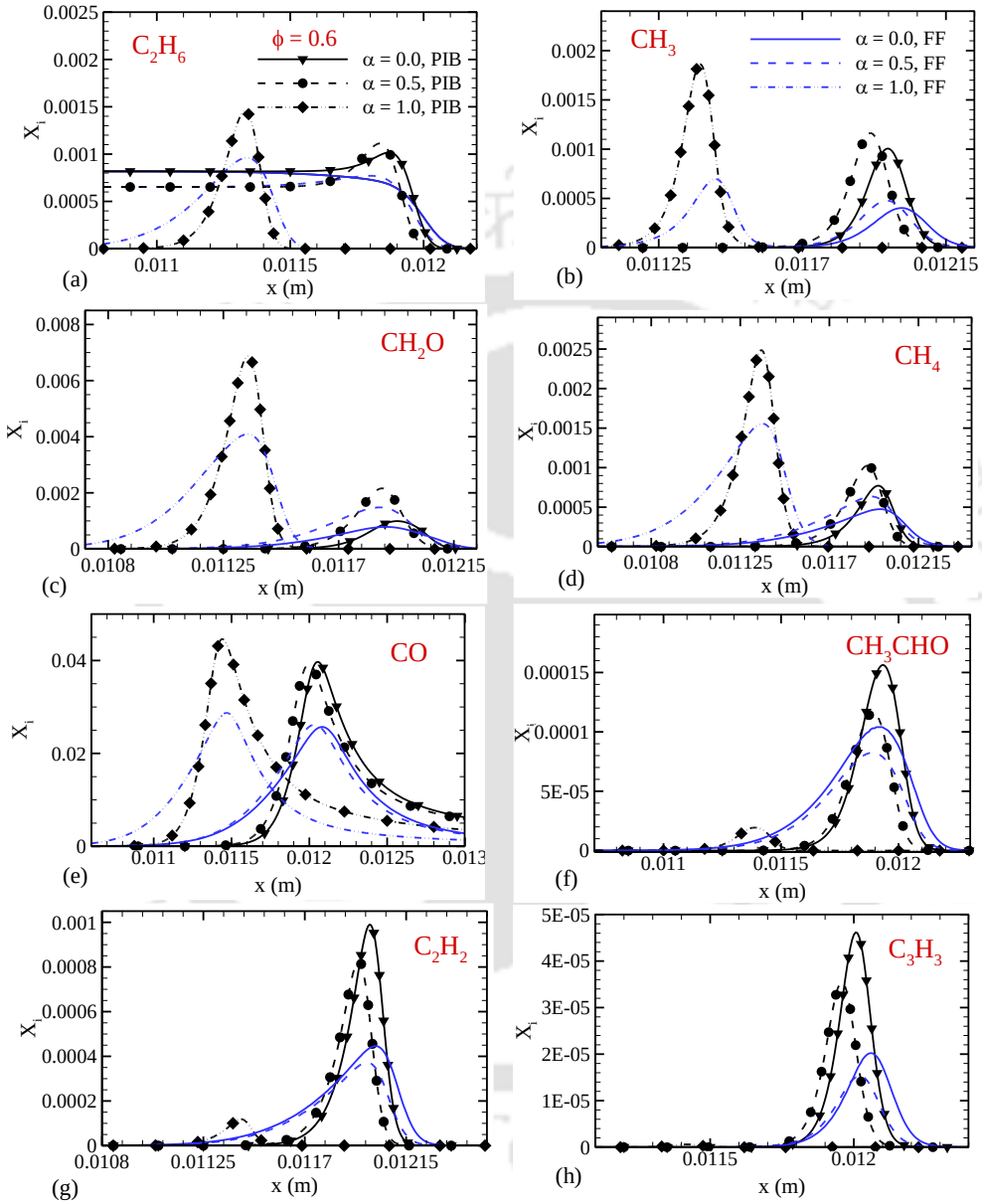

Fig. 4.6. Mole fraction profiles of major intermediate species along the PIB for $\varphi = 0.6$.

The trends of CH_2O are similar to that of CH_3. The peak level of CH_3 and CH_2O continues to increase with increasing α. With the increase of DME fraction a similar trend of increase in CH_3 and CH_2O mole fractions was reported in previous studies [102, 111] for the case of laminar DME/LPG FF. The rate of progress analysis results show that the

β-scission of methoxymethyl ($CH_3OCH_2 \rightleftarrows CH_2O + CH_3$) is an important production path for these hydrocarbons in DME flames, which is not present in the pure LPG oxidation reaction. It is apparent from the results that, the peak concentration of CH_2O in the pure DME flame is approximately 8 times higher than that of LPG flame, whereas, CH_3 mole fraction in DME flame is only two times higher than that of LPG flame. The presence of dominant consumption path of CH_3 through $CH_3OCH_3 + CH_3 \rightleftarrows CH_3OCH_2 + CH_4$ is responsible for the small increase of CH_3 concentration as compared to CH_2O in DME flames.

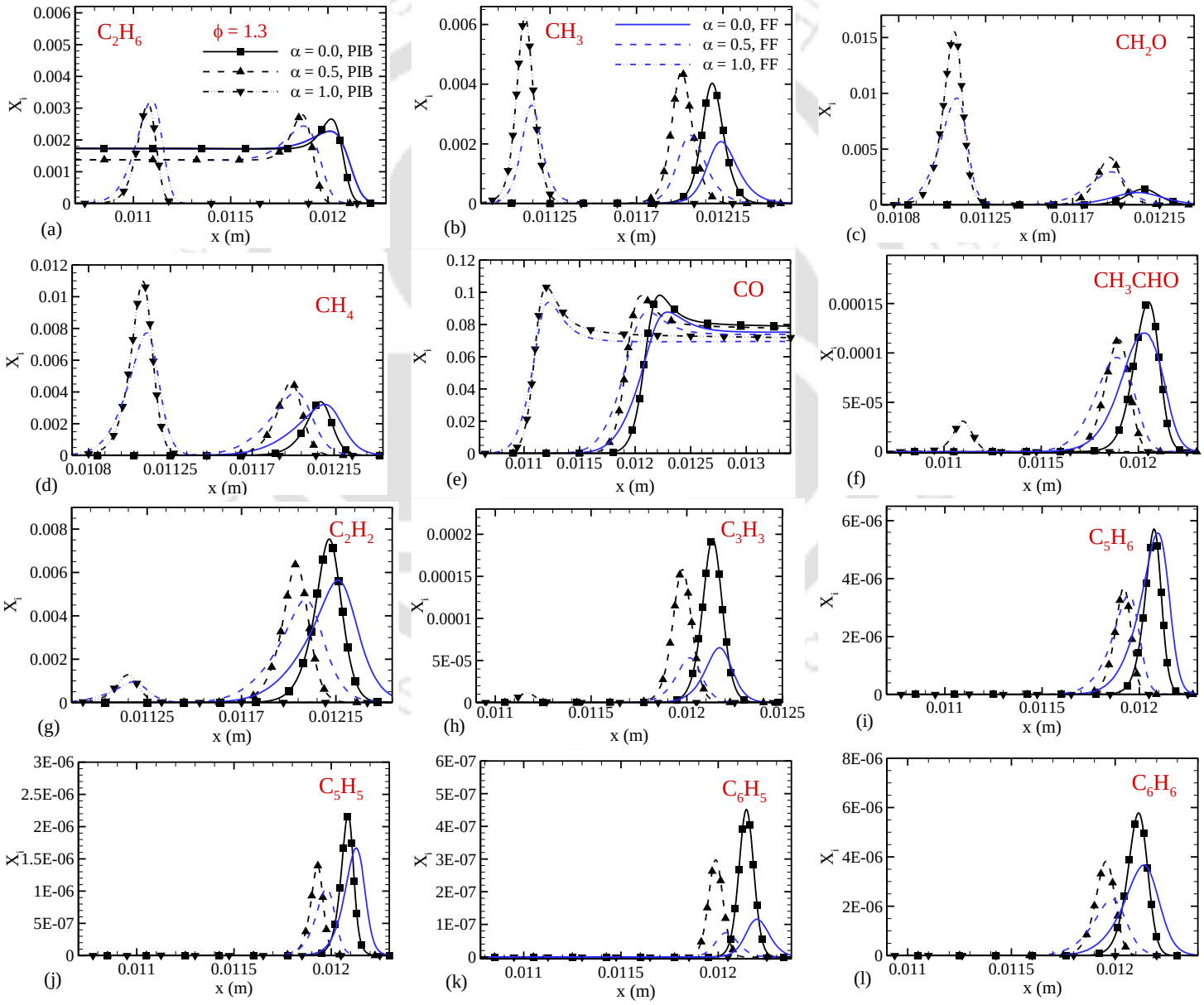

Fig. 4.7. Mole fraction profiles of major intermediate species along the PIB for $\varphi = 1.3$.

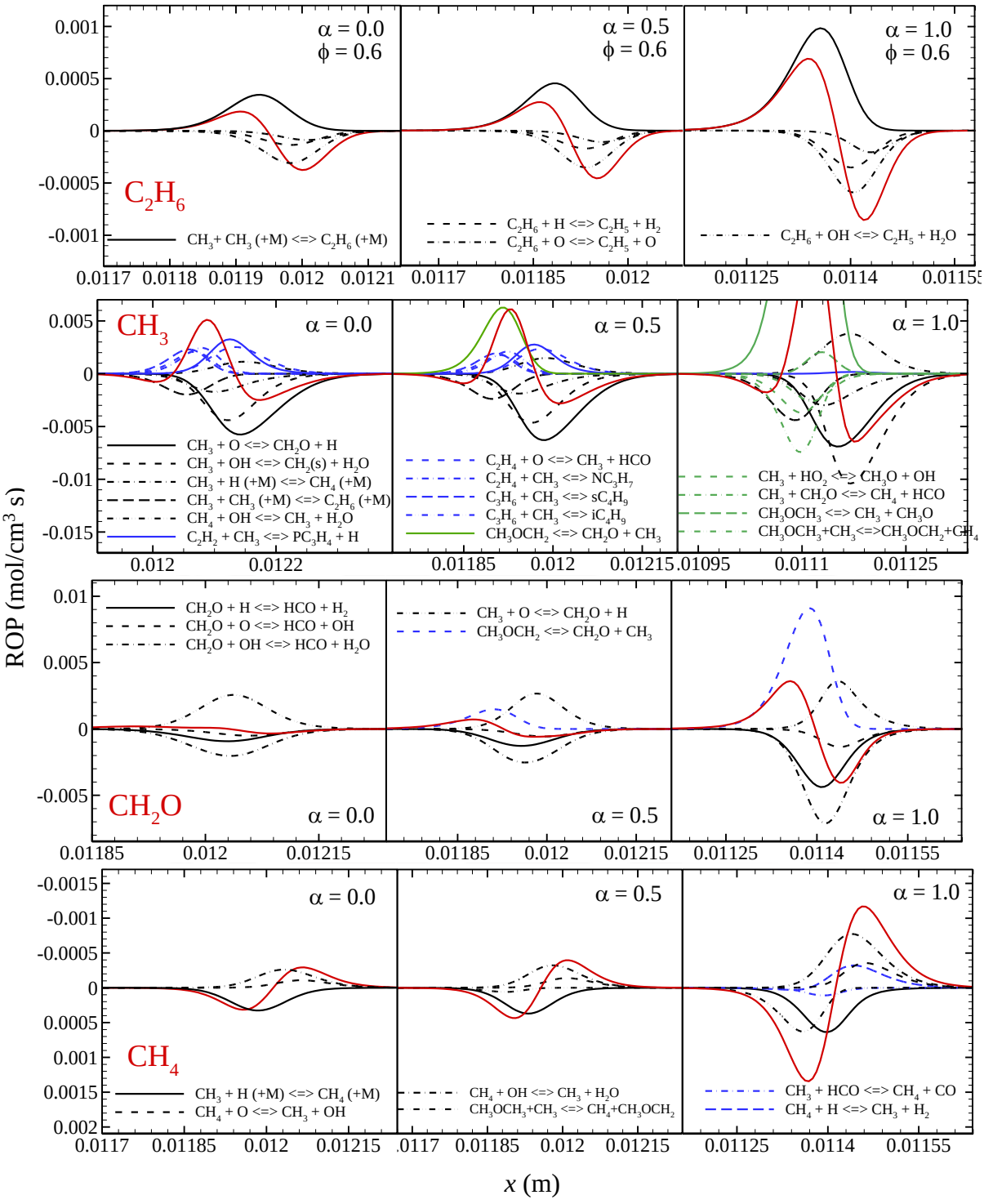

Fig. 4.8. ROP analyses of C_2H_6, CH_3, CH_2O, and CH_4 for lean LPG-DME combustion. Solid lines (red) refer to the total ROP of the species.

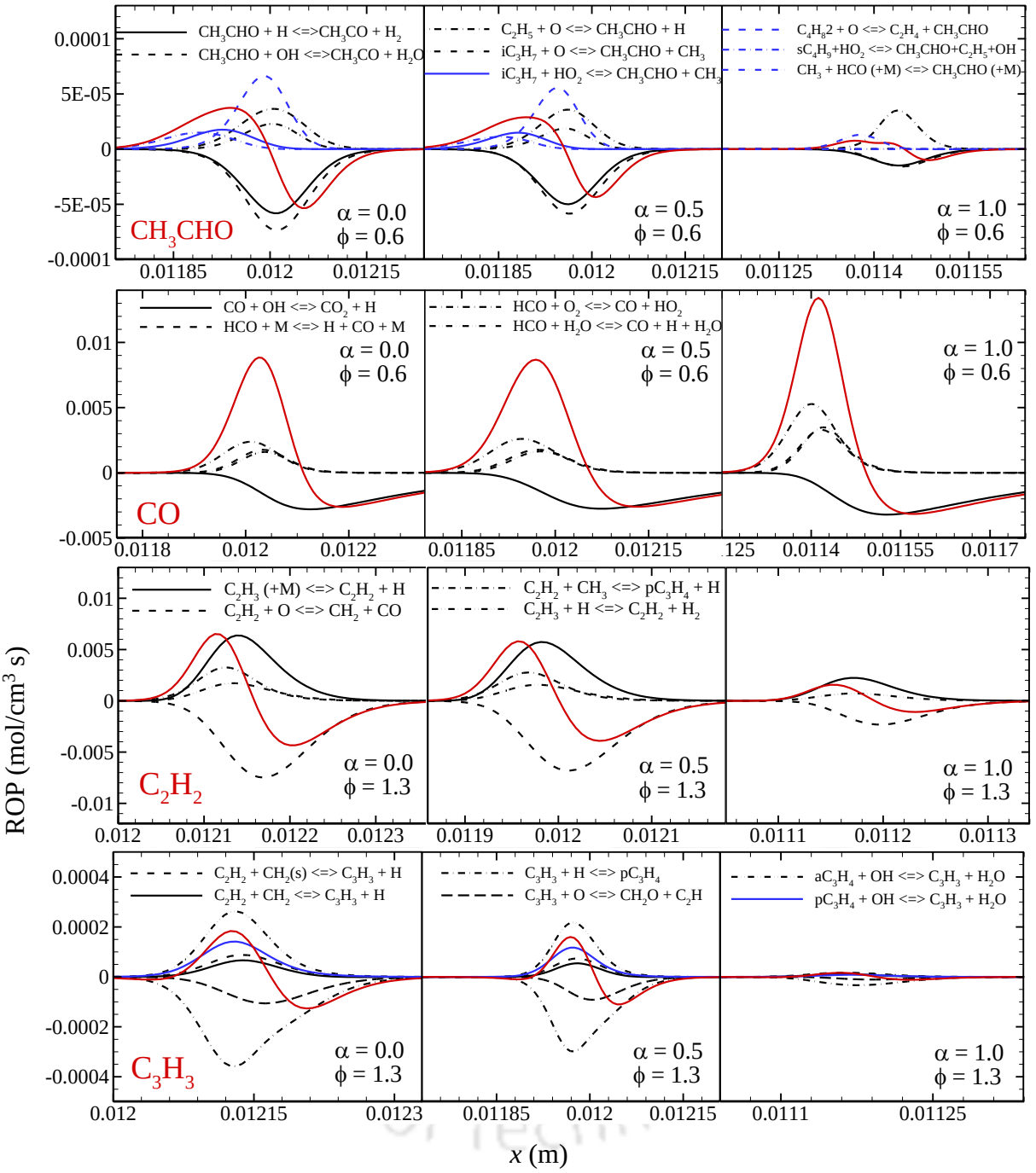

Fig. 4.9. ROP analyses of CH_3CHO, CO, C_2H_2, and C_3H_3 for different LPG-DME flames.

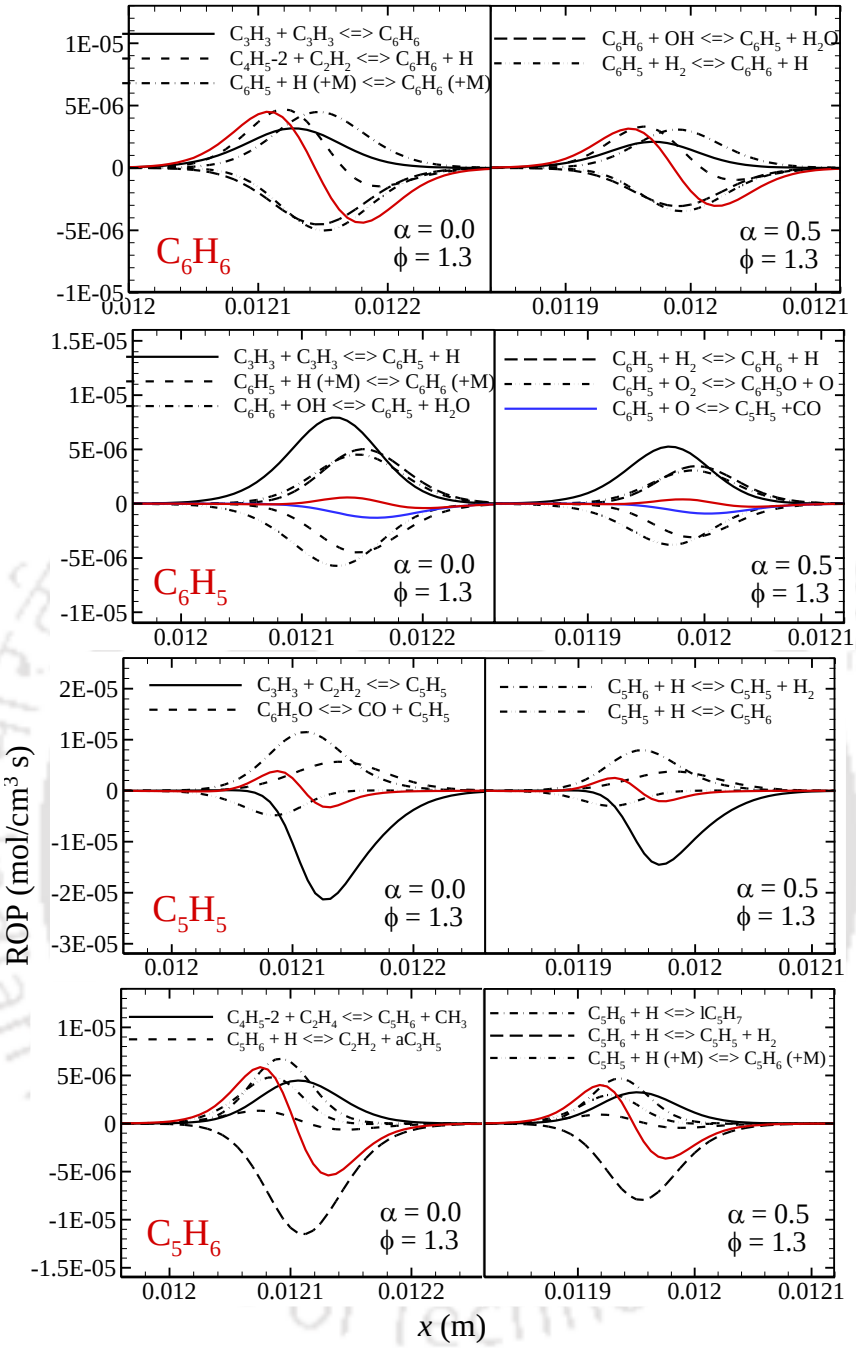

Fig. 4.10. ROP analyses of C_6H_6, C_6H_5, C_5H_5, and C_5H_6 for rich LPG-DME flames. For $\alpha = 1.0$ formation of these species almost disappears.

Since large amount of CH_3 is present in the DME flame compared to the LPG flame, it enhances the methane production through the reaction $CH_3OCH_3 + CH_3 \rightleftarrows CH_3OCH_2 + CH_4$. Thus, the peak concentration of CH_4 increases with the increase of DME level in LPG-DME fuel blend (Figs. 4.6d, 4.7d). This is contrary to what is reported by Bekat et al. [102], where mole fraction of CH_4 remained unaffected by the addition of DME in

C_4H_{10} flame at elevated inlet temperature conditions. Moreover, for all cases, rich flames produce a large amount of CH_4 than lean flames inside the PIB.

Acetaldehyde (CH_3CHO) is a toxic intermediate combustion product formed in hydrocarbon flames. To illustrate the effect of DME addition with LPG, the mole fraction profiles of CH_3CHO for $\alpha = 0.0, 0.5$ and 1.0 are presented in Figs. 4.6f and 4.7f for $\varphi = 0.6$ and $\varphi = 1.3$. The primary reactions related to CH_3CHO are shown in Fig. 4.9. It is observed that the behavior is different to that of formaldehyde. The figure shows a decrease in CH_3CHO concentration with the increase of DME fraction, which is contrary to the observations made by previous study [102] where DME addition increased the formation of CH_3CHO. Bekat et al. [102] showed that $CH_3 + HCO \rightleftarrows CH_3CHO$ is responsible for the increment of acetaldehyde concentration in the DME doped flame, whereas, in the present case progress rate of this reaction remains unaffected with the addition of DME. However, with the flame inside PIB, the rate of formation of reaction $iC_3H_7 + O \rightleftarrows CH_3CHO + CH_3$ and $C_4H_8\text{-}2 + O \rightleftarrows C_2H_4 + CH_3CHO$ decreases significantly when DME fraction in the fuel blend is increased from 0 to 1.0, leading to lower CH_3CHO production. These results suggest that DME addition with LPG fuel can lead to the lower CH_3CHO formation in PIB combustion.

The unsaturated hydrocarbon C_2H_2 and C_3H_3 are considered as the most important soot precursors in the combustion mechanism [110]. With the addition of DME in the C_4H_{10} flame, a slight decrease in C_2H_2 and C_3H_3 mole fractions has been reported previously for the premixed laminar FF condition [102]. Also in the present case, the role of both C_2H_2 and C_3H_3 is significantly reduced in DME blended flame compared to pure LPG flame inside the PIB. For a constant equivalence ratio and mass flow rate, the calculated mole fraction profiles and production rates of dominant reactions related to C_2H_2 and C_3H_3 with different DME concentrations are plotted in Figs. 4.6,4.7 g-h and Fig. 4.9, respectively. These figures show higher concentrations of the soot precursors C_2H_2 and C_3H_3 in the PIB for LPG combustion than that of its combustion in the FF mode. However, it is found that the peak value of C_2H_2 and C_3H_3 decreases significantly when DME is added to LPG in the PIB. Previously, Bekat et al. [102] suggested that the reaction $C_2H_2 + O \rightleftarrows CH_2 + CO$ is responsible for the lower concentration of C_2H_2 in DME blended flame. Whereas in this study, the lower reaction rate of vinyl (C_2H_3) and propyne (pC_3H_4) radicals with H

atom lead to lesser acetylene formation for higher α values inside the PIB. With $\alpha = 0.5$, 19.0% reduction in acetylene formation and 21.0% reduction in propagyl formation can be achieved as compared to pure LPG combustion in the PIB. In the case of pure DME flame within the PIB, an order of magnitude decrease in C_2H_2 and C_3H_3 is observed than that of LPG flame. The production rates of primary reactions related to C_2H_2 and C_3H_3 are presented in Fig. 4.9. It shows that both the consumption rate and formation rate of these reactions are decreased with DME addition. These results imply that DME addition in LPG flames within PIB could suppress the formation of C_2H_2 and C_3H_3.

Equivalence ratio affects the concentration of aromatic rings such as C_6H_6, C_6H_5, C_5H_5, and C_5H_6 significantly. Formation of the aromatic ring is directly associated with the C_3H_3 concentration through $C_3H_3 + C_3H_3 \rightleftarrows C_6H_6$ reaction. As fuel-lean mixture generates less amount of C_3H_3, the production rout of aromatic species almost disappear for LPG/DME flames inside PIB for $\varphi = 0.6$. Figures 4.7i-l and 4.10 show the mole fractions and ROP analyses of C_6H_6, C_6H_5, C_5H_5 and C_5H_6 for fuel-rich conditions. These figures show that the formation of C_6H_6, C_6H_5, C_5H_5, and C_5H_6 reduced significantly for $\alpha = 0.5$ within PIB. Moreover, in the pure DME flame, the formation of these soot precursors almost disappears. This suggests that DME addition in LPG fuel stream can lead to substantial reduction in soot formation in the PIB.

4.2.5. Soot suppression study in DME flame

For the combustion of LPG inside the PIB, the peak concentrations of soot precursors such as C_2H_2, C_3H_3, C_6H_6, C_6H_5, C_5H_5, and C_5H_6 are more than their corresponding FF values; however with the addition of DME in the LPG-air mixture, significant decrease in soot precursors can be achieved, as discussed in the previous section. To gain insight into the soot suppression in DME blended flames, in Fig. 4.11 the main reaction paths of LPG and DME decomposition at rich condition $(\varphi = 1.3)$, leading to the formation of aromatic rings are presented. Reaction pathway analyses of neat LPG, neat DME and LPG/DME mixture are carried out at burner location of 98.6% fuel consumption, corresponding to a T_g of about 1820 K, where benzene concentration reaches its peak value. It is to be noted that, the thickness of the arrows connecting two species in Fig. 4.11 is proportional to the

net elemental fluxes from the species containing C atom and the values above the arrows signify the fraction of parent reactants that are being consumed by different radicals.

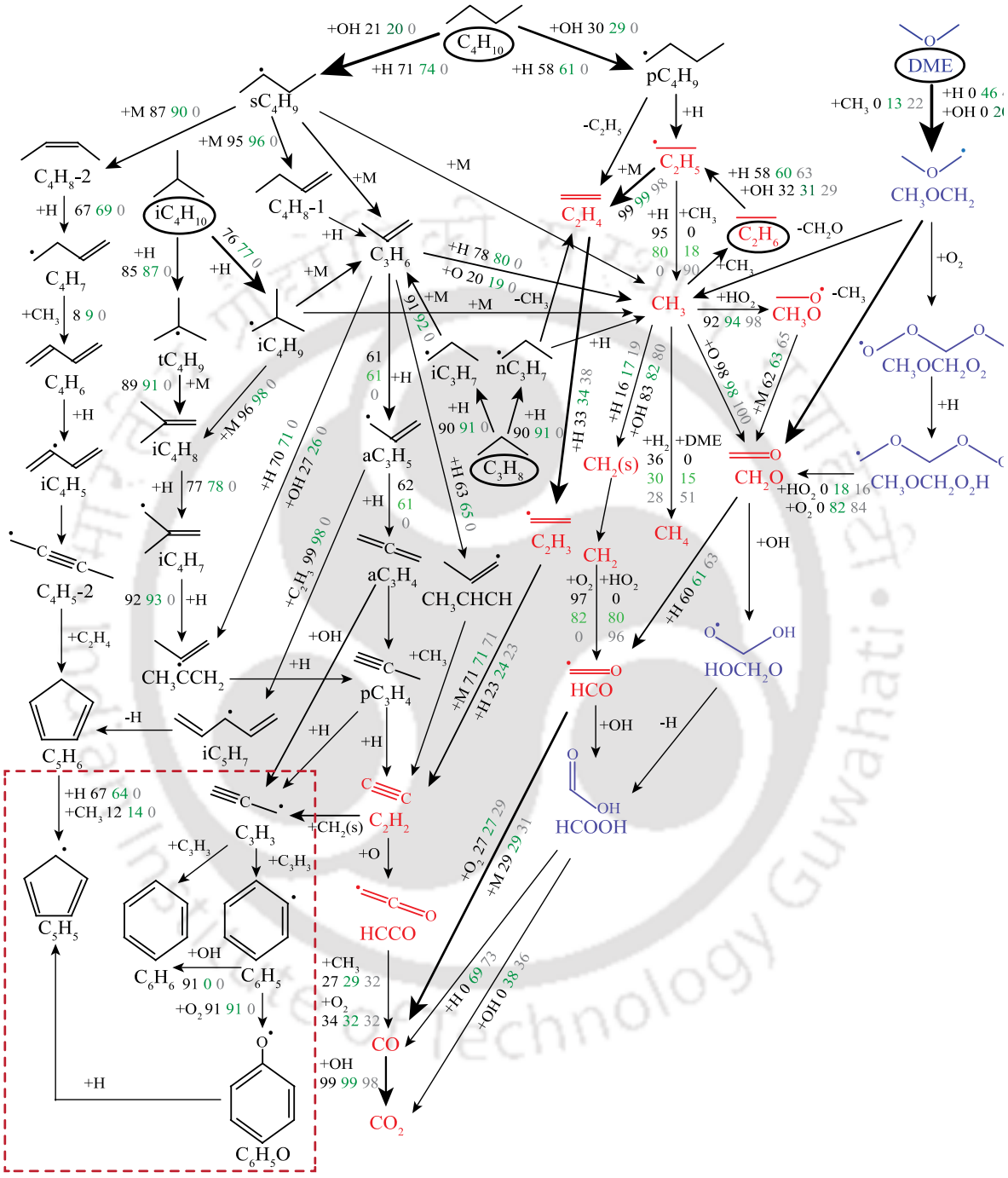

Fig. 4.11. Reaction path analyses of LPG-DME mixture combustion reaction within the PIB. The values above the arrows refer to the fraction of pure LPG (black), DME (gray) and LPG-DME blend (green) fuels, that are being consumed by different radicals

To differentiate the oxidation mechanism of all flames within the PIB, various colors are used to highlight major species produced by both LPG and DME fuels (red), by neat LPG fuel (black), and by neat DME fuel (blue). For all cases, the importance of reactions involving OH radical reduces, with the addition of DME in the fuel-air mixture, whereas, a higher percentage contribution of H atom and CH_3 radical is observed in the DME-doped flame inside the PIB.

In Fig. 4.11 the production pathways of major soot precursors are presented within the dashed box, which completely vanish for neat DME flame within PIB. It shows that for LPG flame within PIB, the C_3H_3 formation pathways through aC_3H_4 and pC_3H_4 species are dominant contributors in aromatic ring generation and, with the addition of DME, these pathways disappear. Moreover, oxidation of DME leads to the formation of C_1-C_2 hydrocarbon intermediates, which subsequently reduce the generation of soot precursors.

Figure 4.11 also indicates that DME addition into the LPG fuel stream produces some new oxygenated species: CH_3OCH_2, $CH_3OCH_2O_2$, CH_3OCH_2O2H, $HOCH_2O$, and HCOOH. From these species, CH_3OCH_2 is an important intermediate, which contributes to the formation of CH_3 and CH_2O as discussed before. However, the intermediates; $CH_3OCH_2O_2$, $CH_3OCH_2O_2H$, $HOCH_2O$, and HCOOH, are generated with lower concentrations.

4.2.6. Effect of DME addition on H_2/syngas production

The PIB is also regarded as the most promising technology for producing H_2 and syngas (H_2 + CO) from the fuel-rich combustion of gaseous and liquid hydrocarbons [112-117]. In order to demonstrate the influence of DME addition on the H_2/syngas generation capability of LPG-air combustion under fuel-rich conditions, Fig. 4.12 reports the concentrations of H_2, CO, and CO_2 at the PIB exit as a function of α, for the same input condition of $\varphi = 1.3$ and m = 1.5 kg/m^2 s. It is found that conversion of initial reactant to H_2 increases mildly with the addition of DME to the LPG-air mixture. However, a substantial decrease in CO mole fraction is observed with the increase of DME content in the LPG-DME mixtures causing a decline in syngas yield. Moreover, for higher α value, CO_2 content is found to increase in the flue gas, thereby leading to the production of syngas with a low caloric value.

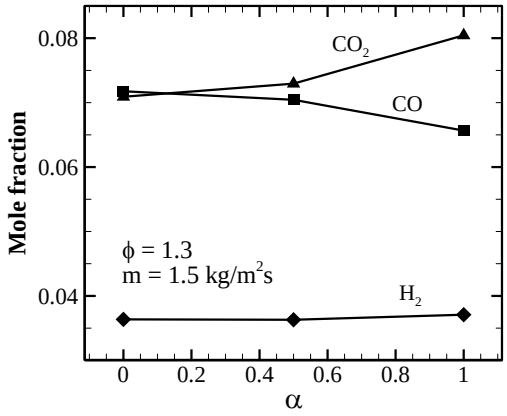

Fig. 4.12. Concentrations of H_2, CO, and CO_2 as a function of α at $\varphi = 1.3$.

4.2.7. Flame thickness of different LPG-DME blends inside the PIB

In combustion technology, the flame thickness and filtration velocity are inversely proportional to each other. In this study, the flame thickness is calculated using temperature gradient method,

$$\zeta = \frac{T_{g,\max} - T_{g,\text{in}}}{\left.\frac{\mathrm{d}T_g}{\mathrm{d}x}\right|_{\max}} \tag{4.2}$$

A flame with a thinner reaction zone width has higher filtration velocity and leads to the furtherance of reaction rates. With flames located at their respective operating limit (HL and LL) in the PIB, Table 4.2 compares the flame thickness of pure LPG, LPG-DME blend $(\alpha = 0.5)$, and pure DME combustion within the PIB and in FF mode as a function of equivalence ratio. The expected trend of variation of flame thickness with equivalence ratio can be seen for all cases.

It is seen from Table 4.2 that, for all values of α and φ, combustion in the PIB exhibits thinner flame width than that of the laminar FF. It is further observed that for a certain φ, the flame inside the PIB has narrower reaction zone thickness at a mass flow rate corresponding to the HL than that of LL of the stable operating range, which is due to the increase in filtration velocity as discussed in section 4.2.1. The computed results also suggest that for a given equivalence ratio the DME blended flame within the PIB has thinner reaction zone width than that of LPG flame, especially under fuel-lean and fuel-rich side this effect appears to be more pronounced.

Table 4.2. Flame thickness (mm) of various LPG/DME flames in the PIB and in FF

φ	$\alpha = 0.0$			$\alpha = 0.5$			$\alpha = 1.0$		
	FF	**PIB**		**FF**	**PIB**		**FF**	**PIB**	
		LL	**HL**		**LL**	**HL**		**LL**	**HL**
0.5	1.14	0.67	0.55	1.10	0.66	0.53	1.09	0.39	0.36
0.6	0.69	0.47	0.43	0.62	0.42	0.40	0.57	0.35	0.34
0.7	0.51	0.35	0.34	0.51	0.36	0.34	0.46	0.32	0.32
0.8	0.44	0.32	0.32	0.42	0.32	0.31	0.35	0.30	0.29
0.9	0.40	0.30	0.30	0.38	0.30	0.28	0.32	0.27	0.27
1.0	0.40	0.29	0.29	0.39	0.27	0.26	0.32	0.26	0.26
1.1	0.39	0.29	0.29	0.38	0.26	0.26	0.32	0.25	0.24
1.2	0.38	0.30	0.29	0.36	0.26	0.26	0.31	0.24	0.24
1.3	0.41	0.32	0.3	0.44	0.28	0.28	0.30	0.24	0.24

4.2.8. Sensitivity analyses

To interpret the influence of different reactions on the burner reactivity due to DME addition, the sensitivity analyses of filtration velocity for various DME-LPG-air mixtures ($\alpha = 0.0, 0.5$ and 1.0) within the PIB are investigated in Fig. 4.13. For both fuel-lean and fuel-rich conditions, sensitivity analysis is conducted using the USC-Zhao Mech model. In addition, the sensitivity coefficients of laminar FF speed are also presented at the same input conditions for the purpose of comparison. The sensitivity analyses for premixed DME-air FF are qualitatively consistent with the results obtained by Zhao et al. [106]. The normalized sensitivity is determined using $\left(A_i / V_0\right)\left(\partial V_0 / \partial A_i\right)$, where A_i refers to the pre-exponential factor for i^{th} reaction.

It is observed from Fig. 4.13 that, for combustion of LPG-DME-air mixtures inside the PIB, all reactions exhibit less sensitivity than their respective FF values for both fuel-lean and fuel-rich conditions. The observed trend is due to the fact that, combustion of fuel-air mixture within PIB instead of gas environment causes the reaction equilibrium to move

toward the reactant side at high-temperature conditions. As expected for all cases the chain branching reaction, H + O_2 ⇄ O + OH is the most sensitive reaction that promotes the filtration velocity of the burner. Furthermore, with an increase in DME fraction, the sensitivity coefficient of this reaction decreases. The CO oxidation reaction CO + OH ⇄ CO_2 + H is the second most dominant reaction for lean fuel-air combustion, while the HCO decomposition reaction, HCO + M ⇄ CO + H + M exhibits the second highest positive sensitivity for rich fuel-air combustion inside PIB. The higher sensitivity of the CO oxidation reaction than the HCO decomposition reaction in the lean flame is due to the larger contribution of the former reaction toward the generation of H atoms, which enhances the burner reactivity. In addition, for both fuel-lean and fuel-rich flames the sensitivity of these two reactions increases as the DME fraction increases in the fuel-air mixture.

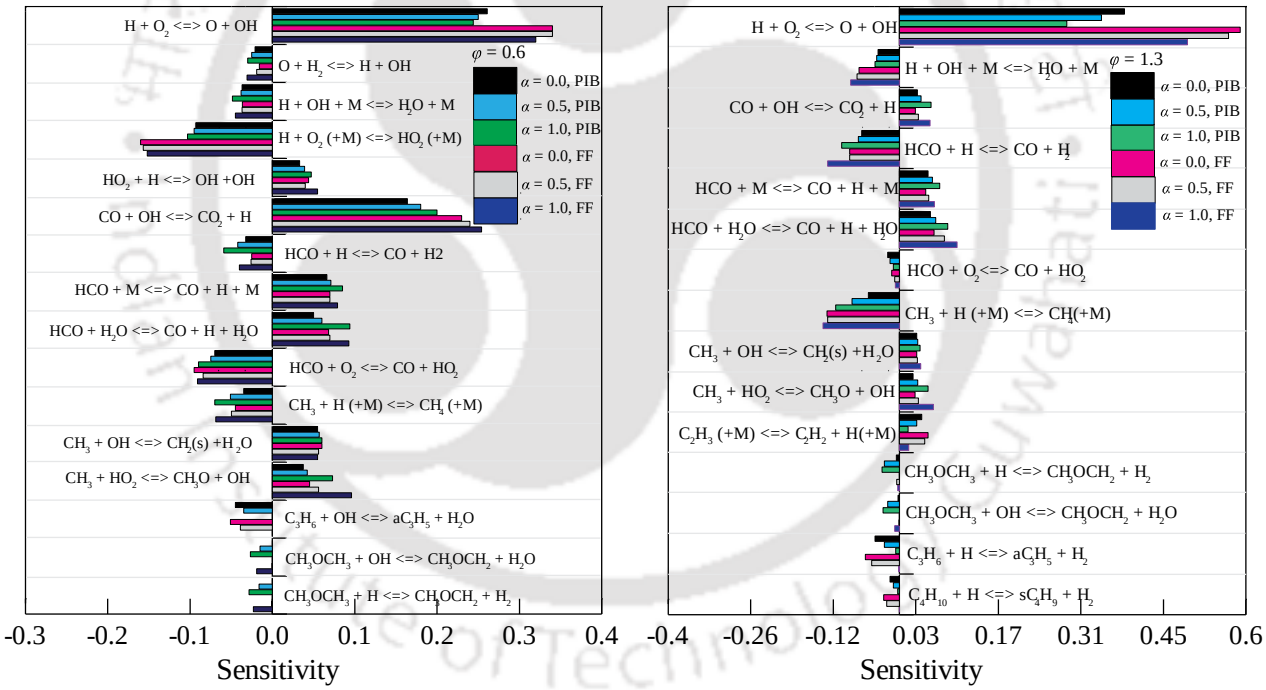

Fig. 4.13. Comparisons of sensitivity analyses of filtration velocity for **(a)** lean LPG-DME combustion and **(b)** rich LPG-DME combustion inside the PIB with their respective FF values.

From Fig. 4.13 it is observed that for fuel-lean conditions the chain termination reaction H + O_2 (+M) ⇄ HO_2 (+M) is the most negative sensitive reaction, which inhibits the filtration velocity of the burner. However, for rich conditions CH_3 + H (+M) ⇄ CH_4 (+M)

is the most important chain-termination reaction. Moreover, for all flames the chain-propagation reaction $CH_3 + HO_2 \rightleftarrows CH_3O + OH$ plays an important role, increasing the concentration of OH and CH_3O radicals, and therefore prompting the reactivity of combustion process inside the PIB. The $HCO + H_2O \rightleftarrows CO + H + H_2O$ and $CH_3 + OH \rightleftarrows CH_2(s) + H_2O$ reactions also exhibit positive sensitivity at both lean and rich conditions, as shown in Fig. 4.13. The sensitivity of these reactions strengthened with the addition of DME in the LPG-air mixture, enhancing the filtration velocity of the flame within the burner. The LPG specific reaction $C_4H_{10} + OH \rightleftarrows sC_4H_9 + H_2O$ shows a small positive sensitivity coefficient, and its reactivity decreases with DME addition due to the reduction of LPG concentration in the DME-LPG mixtures. The DME specific reactions such as $CH_3OCH_3 + OH \rightleftarrows CH_3OCH_2 + H_2O$, $CH_3OCH_3 \rightleftarrows CH_3 + CH_3O$ and $CH_3OCH_3 + H \rightleftarrows CH_3OCH_2 + H_2$ are also relatively less sensitive to the filtration velocity of the PIB. The normalized sensitivity of these reactions increases by increment of DME fraction.

4.2.9. Parametric sensitivity

To investigate the influence of various thermal and optical parameters on the overall reactivity of PIB, filtration velocity sensitivity of LPG/DME/air flame is presented in Fig. 4.14. Equivalence ratios corresponding to lean and rich flames are found to be more dominant parameters for the filtration velocity sensitivity than that of stoichiometric flame. For the fuel-lean conditions with an increase in equivalence ratio, the V_0 increases, causing a positive sensitivity coefficient. Whereas, in case of fuel-rich flames, for higher equivalence ratio the V_0 reduces, leading to a negative sensitivity coefficient. In addition, the other parameters such as scattering albedo and extinction coefficient show negative sensitivity inhibiting the reactivity of the burner. The total fractional amount of energy attenuated due to scattering (υ_s) and absorption (κ_a) of radiation per unit length is called extinction coefficient $\Gamma(=\kappa_a+\upsilon_s)$. The scattering albedo (ω) is defined as the fraction of radiation energy attenuated by scattering over the total extinction $\left(\omega=\frac{\upsilon_s}{\Gamma}\right)$. The negative sensitivity of these two parameters is due to the fact that, PIB with higher scattering albedo and extinction coefficient absorb less radiation energy, thus leading to a decrease in preheating temperature, which subsequently decreases the V_0.

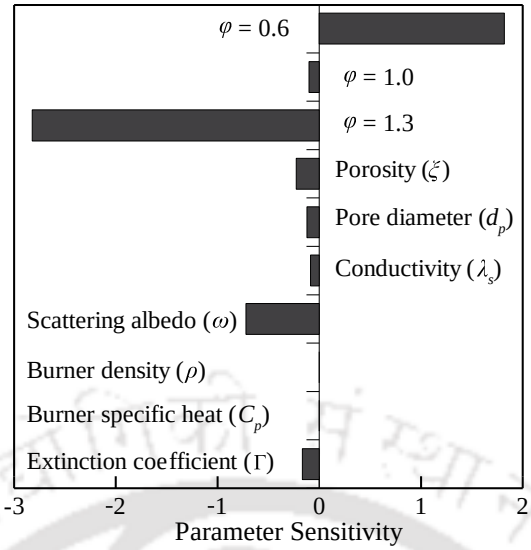

Fig. 4.14. Sensitivity of different PIB properties on filtration velocity

The burner conductivity and porosity of the PIB exhibit positive sensitivity, which increases the V_0. This is owing to the fact that, medium with high porosity possesses low extinction coefficient, and thus by absorbing more radiative energy it increases the burner reactivity. Similarly, with the increase of burner conductivity, a greater amount of heat can be conducted back to the preheat section. This leads to an enhancement of incoming fuel-air mixture temperature, which ultimately increases the V_0 of the PIB. However, the filtration velocity is found to be insensitive to the porous burner density and specific heat capacity, as seen in Fig. 4.14.

4.3. Summary

The addition of DME on the premixed LPG-air combustion within the two-section PIB was analyzed for both fuel-lean and fuel-rich conditions. The reaction pathway and rate of production analyses were performed by using an extended USC-Zhao Mech model consisting of 836 elementary reactions and 128 different species. For the sake of validation, numerical predictions for filtration velocities and temperature distributions were compared to the experiment results. The axial temperature profiles, mole fraction distributions, overall heat release rate and the production rate of dominant reactions associated with major flame species inside the PIB were also investigated for different LPG-DME-air mixtures. To investigate the influence of important reactions on the burner reactivity due to DME addition, a sensitivity analysis was carried out using the USC-

Zhao Mech model. In addition, the effect of different DME levels in the fuel-air mixture on the filtration velocity sensitivity, and reaction zone thickness of the PIB were also analyzed.

CHAPTER 5

PERFORMANCE EVALUATION OF DME AS AN ALTERNATIVE FUEL

At present, there exists no report in the literature of any domestic burner that is fully compatible with both LPG and DME fuel. Unlike the previous studies [67, 70], where the burner required modification of its components and design to facilitate the combustion of both DME and LPG fuels, in this work the stable combustion for both LPG-air and DME-air mixtures in the same burner setup is investigated using the energy-efficient PIB. The novelty brought by the present study is that we employed the heat recirculation technique of the PMC in the domestic burner for providing low emission and high efficient stove offering fuel compatibility for both LPG and DME. The results obtained in this Chapter will help to understand the effects of various operating parameters on the thermal performances of the PIB stove burning both LPG and DME. Therefore, the aim of this Chapter is to assess the advantages of DME combustion within PIB integrated stove through experimental and numerical investigation.

In the following, first the stable operating ranges, and CO emissions for the combustion of the DME-air mixture within the PIB stove obtained from the experiment and the numerical formulation are compared with the results of LPG-air combustion obtained using the same stove setup. In order to investigate the heat recirculation phenomenon of the PIB, the conduction and radiation energy feedback in terms of preheat conduction

efficiency and preheat radiation efficiency are also investigated in details. Furthermore, to assess the benefit of ultra-lean DME-air combustion inside the PIB, the performance of the burner in terms of radiation and thermal efficiencies, as well as temperature distributions for various thermal inputs and equivalence ratios are investigated. In addition, to understand the dynamics of the DME-air flame within the PIB under the ultra-fuel-lean condition, the structure of chemical reactions, radical pool formation, and heat generation rate contributions are investigated through detailed kinetic mechanism and reaction path analyses.

5.1. Results and Discussions

5.1.1. Stable operating ranges of DME-air flames within the PIB stove

Porous burners are considered as a potential substitute to the conventional gas burners for their better fuel flexibility, extended flammability limits and the ability to stabilization of combustion over a wide range of input conditions. Thus, specific attention is paid to the study of burner's stable operating range and LFL for the combustion of DME-air mixture. As discussed in previous Chapters, for a given φ, above the LFL, the thermal load attains its LL at the upstream section of the interface of the PIB, while it achieves the HL at the downstream portion. Therefore, the burner must be operated within these thermal power limits for the stable combustion of DME-air flame at a particular φ. Table 5.1 and Table 5.2 summarize these results.

In Table 5.1 the experimental measurements for the stable operating ranges in terms of Q_{th} are presented for the combustion of the DME-air mixture within the PIB stove for equivalence ratios in the range of $\varphi = 0.4 - 0.8$. Moreover, for the sake of comparison, previously mentioned results of stable operating limits for the LPG-air flames are also reported in Table 5.1. Furthermore, the comparisons of the Q_{th} for the LPG fired PIB and the conventional burner are presented in the table. For all the values of φ, Q_{th} for the PIB stove is found to be higher than that of the conventional burner. From Table 5.1, it also can be observed that in the conventional burner flame cannot be sustained for equivalence ratio less than $\varphi = 0.6$.

The stable operating limits of the PIB with DME flame follow the same trend as the LPG flame. For both the fuels with the increase of φ from 0.4 to 0.8, the stable thermal power limits move towards higher values. However, the stability range of DME flame in the PIB are found to be less than that of LPG flame for a given φ. This trend is due to the lower calorific value of DME as compared to the LPG fuel, which is also responsible for the higher LFL of DME flame inside the burner as shown in Table 5.2. Both experimental measurements and computational prediction show higher LFL for DME flame than that of LPG flame inside the PIB. From Table 5.2 it can be observed that within the PIB the DME-air flame cannot self-sustain below the flammability limit of $\varphi = 0.38$, while for LPG-air mixture this value is $\varphi = 0.31$.

Table 5.1. Operating range of the PIB stove for various fuel-air mixtures

Equivalence Ratio (φ)	Operating range, Q_{th} (kW)		
	DME-air, PIB stove	LPG-air, PIB stove	LPG-air, Conventional burner
0.4	0.93-2.4	0.55-3.23	-
0.5	3.4-4.9	3.0-6.18	-
0.6	7.1-9.51	6.16-9.44	2.668
0.7	11.14-12.87	8.95-12.77	4.61
0.8	14.6-16.7	12.91-16.59	6.624

Table 5.2. Comparisons of flammability limits

	Lean Flammability limit (φ)	
	DME-air	LPG-air
Numerical results	0.35	0.29
Experimental results	0.38	0.31

5.1.2. CO emissions suppression and combustion enhancement of DME fired PIB

In Fig. 5.1a, the measured and computed equilibrium CO concentrations for the combustion of DME and LPG in the PIB stove are presented at various Q_{th} and φ. It is observed that, at all input conditions, both the measurement and prediction show lower CO concentrations for the DME flame than the LPG flame inside the PIB. For example,

at $\varphi = 0.5$ and thermal load in the range of Q_{th} = 3.9 - 5.04 kW, an average reduction of 47.1% in CO emission can be seen for the DME flame as compared to the LPG flame, while for $\varphi = 0.6$ and for thermal operating range in the limit of 7.9 - 9.2 kW, with DME flame an average reduction of 27% can be attained in CO emission. This suggests that further reduction in CO emission can be achieved with the use of DME instead of LPG in the PIB stove.

The conventional stoves produces more CO emission than the restriction limit prescribed by the WHO for indoor environment. However, with the use of PIB at the fuel-lean condition the CO emission comes under the WHO restriction limit. Figure 5.1a support these outcomes for the combustion of DME-air and LPG-air mixture within the PIB stove. It can be seen that CO emissions for both LPG and DME flames in the PIB operating at $\varphi = 0.4$ are lower than the constraint of WHO standard. Whereas, for $\varphi = 0.5$ and thermal power of above Q_{th} = 4.0 kW the LPG fired PIB exceeds the emission limit permitted by WHO. However, at $\varphi = 0.5$ the CO emission for the DME combustion in the PIB is found to be lower than the WHO limitation. From Fig. 5.1a it is also evident that at $\varphi = 0.6,$ for all the operating ranges the CO emissions from both the LPG and DME fired burners are above the WHO standards. Thus if DME is used instead of LPG in the PIB, following the guideline of WHO, the maximum allowable equivalence ratio can be extended from $\varphi = 0.4$ to $\varphi = 0.5,$ and the thermal load from Q_{th} = 4.0 kW to Q_{th} = 5.0 kW.

CO emission is sensitive to the flame temperature and the location of the flame within the PIB. To further understand the reduction in CO emission for DME flame than that of LPG flame in the PIB stove, in Fig 5.1b the axial gas and solid-phase temperature profiles of the burner for the combustion of both LPG-air and DME-air mixtures are compared under the same operating condition of $\varphi = 0.5,$ and Q_{th}=5.0 kW. Figure 5.1c shows the close-up view of the gas-phase (T_g) and solid-phase (T_s) temperature distributions along with the CO mole fraction profiles for the combustion of LPG and DME inside the PIB stove. It is observed that DME flame has higher gas and solid-phase temperature than that of LPG flame. Moreover, when DME is allowed to burn inside the PIB instead of LPG, the flame front shifts towards upstream section of the burner. This is attributed to the fact that, for a particular φ and Q_{th}, DME flame yields more amount of active free radicals

(HO_2, OH, O, H) than that of LPG flame within the PM as seen in Fig. 5.2a. This leads to the furtherance of reaction rate causing the combustion zone to move towards the upstream location. Thus the longer residence time of the hot DME-air combustion products inside the PIB caused by the shifting of flame location towards upstream section subsequently reduces the CO emission.

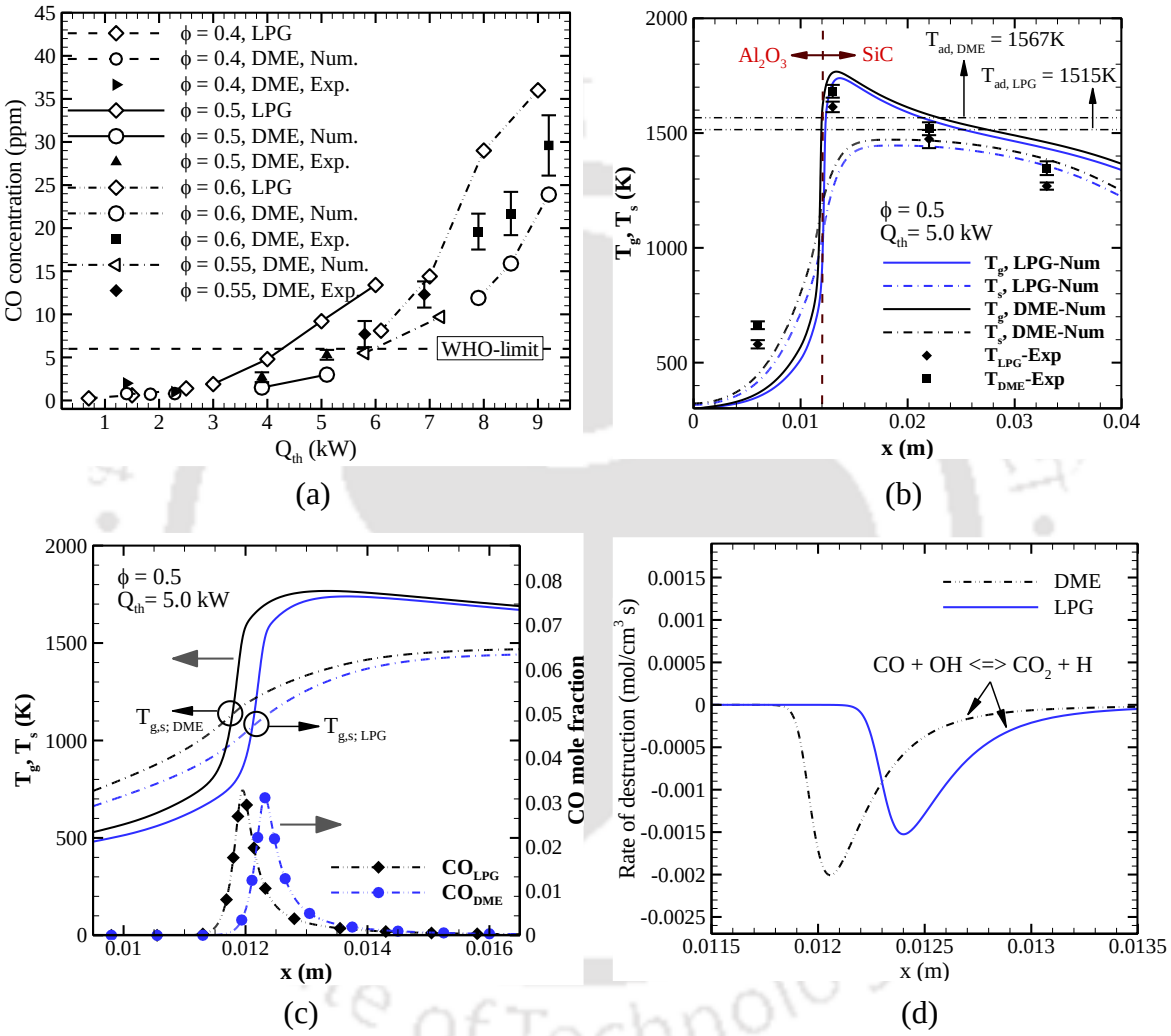

Fig. 5.1. (a) Comparisons of measured and computed CO emissions for the combustion of DME and LPG in the PIB at various Q_{th} and φ, **(b)** The axial T_g and T_s profiles of the PIB, **(c)** The close-up view of the T_g and T_s along with the CO mole fraction profiles, and **(d)** the destruction rate of CO + OH ⇄ CO_2 + H for LPG and DME flame at $\varphi = 0.5$, and Q_{th} = 5.0 kW.

In addition, higher radical pool concentration for DME flame leads to an increase in burner temperature as compared to LPG flame. At a given φ and Q_{th}, lower CO emission

in the case of DME flame is also due to the higher combustion temperature inside the PIB, which ultimately increases the oxidation rate of CO to produce CO_2 through the reaction CO + OH ⇄ CO_2 + H. Figure 5.1d support this claim where the destruction rate of the reaction CO + OH ⇄ CO_2 + H is shown for the combustion of DME-air and LPG-air mixture under the same input operating condition. Although the peak CO mole fractions attained by both LPG and DME flames are of the same magnitude (Fig. 5.1c), the combined effect of higher oxidation rate of the reaction CO + OH ⇄ CO_2 + H and longer residence time of hot DME-air combustion products leads to the reduction of CO emission.

5.1.3. Heat recirculation mechanism of the PIB

The heat recirculation mechanism in the highly radiative and conductive PM of the burner permits the stove to operate in excess enthalpy mode, which subsequently increases the combustion efficiency of the burner. The energy feedback in the preheat zone (Al_2O_3 section) is instigated by the combined effect of conduction and radiation heat transfer from the solid-phase of the PIB. In order to demonstrate the heat recirculation phenomena within the PIB, the comparisons of percentage preheat conduction efficiency $\left(\eta_{pc}\right)$, preheat radiation efficiency $\left(\eta_{pr}\right)$ and total heat recirculation efficiency $\left(\eta_{hr}\right)$ due to the combustion of DME/LPG-air mixtures inside the PIB stove are reported in Table 5.3 and are defined as,

$$\eta_{pc} = \frac{\text{conduction heat transfer into preheat zone}}{\dot{m}_{fuel} \times Q_{LHV}} \tag{5.1}$$

$$\eta_{pr} = \frac{\text{radiative heat transfer into preheat zone}}{\dot{m}_{fuel} \times Q_{LHV}} \tag{5.2}$$

$$\eta_{hr} = \frac{\text{convective heat transfer from solid- to gas-phase in preheat zone}}{\dot{m}_{fuel} \times Q_{LHV}} \tag{5.3}$$

Upon inspection of Table 5.3 it can be seen that at the same input operating condition of $\varphi = 0.5$, and Q_{th} = 5.0 kW, a higher fraction of heat is recirculated to the reactants for the DME-air combustion than the LPG-air combustion inside the PIB. For the DME-air case, 32.9% of the heat is recirculated to the incoming air-fuel mixture, while for the LPG-air mixture 30.6% of the total heat is recirculated. Furthermore, the preheat conduction

efficiency and preheat radiation efficiency are also more for DME-air flame within the PIB stove, which consequently increases the total *HRR* and thus the combustion temperature of the PIB. Figure 5.1b shows that at $\varphi = 0.5$ the peak temperatures estimated and measured at the location T_3 for combustion of both the fuels inside the PIB are more than their corresponding adiabatic FF temperature values, which ensures that the excess enthalpy combustion mode is achieved within the stove.

Table 5.3. Comparisons of preheating efficiencies at $\varphi = 0.5$, and Q_{th} = 5.0 kW

	Preheat efficiency (η)	
	DME-air	LPG-air
Heat recirculation efficiency (η_{hr})	32.9	30.6
Preheat conduction efficiency (η_{pc})	17.3	16.6
Preheat radiation efficiency (η_{pr})	15.6	14

It is also observed that the maximum temperature obtained in the PIB due to the combustion of DME-air mixture is higher than the LPG-air combustion. This is attributed to the fact that, for a constant φ and Q_{th} the overall heat release rate (*THRR*) is more in the case of DME flame, as seen in Fig. 5.2b. Figure 5.2b shows the heat release rate of the most important reactions responsible for the increase in *THRR* for the DME flame inside the PIB. At Q_{th} = 5.0 kW the *THRR* for LPG-air combustion inside the PIB is 2520 J/cm^3 s, while for the DME-air combustion the same is 3288 J/cm^3 s.

The influence of equivalence ratio and input thermal load on the radiant efficiency and thermal efficiency of the burner are shown in Fig. 5.3. Here for a given equivalence ratio, the thermal load is fixed within their corresponding stability limit and the relevant radiant efficiency and thermal efficiency are reported for the combustion of DME-air and LPG-air mixture in the PIB stove. In this study, the radiant efficiency (η_{rad}) is calculated through the following formula:

$$\eta_{rad} = \frac{Q_R}{\dot{m}_{fuel} \times Q_{LHV}} \tag{5.4}$$

where, $Q_R = q_{wall} + \sigma\varepsilon A_c(T_s^4 - T_o^4)$, with T_s is the temperature of the top surface of the SiC matrix, T_o is the ambient temperature and q_{wall} is calculated from Eq. (2.17). The results obtained indicate that for a given fuel-air mixture the η_{rad} and η_{th} are higher for low equivalence ratio. This effect is caused by the higher combustion efficiency of lean fuel-air mixture compared to the rich fuel-air mixture. In addition, at a given equivalence ratio φ, η_{rad}, and η_{th} of the PIB stove are observed to be more at lower Q_{th} value for both DME and LPG combustion.

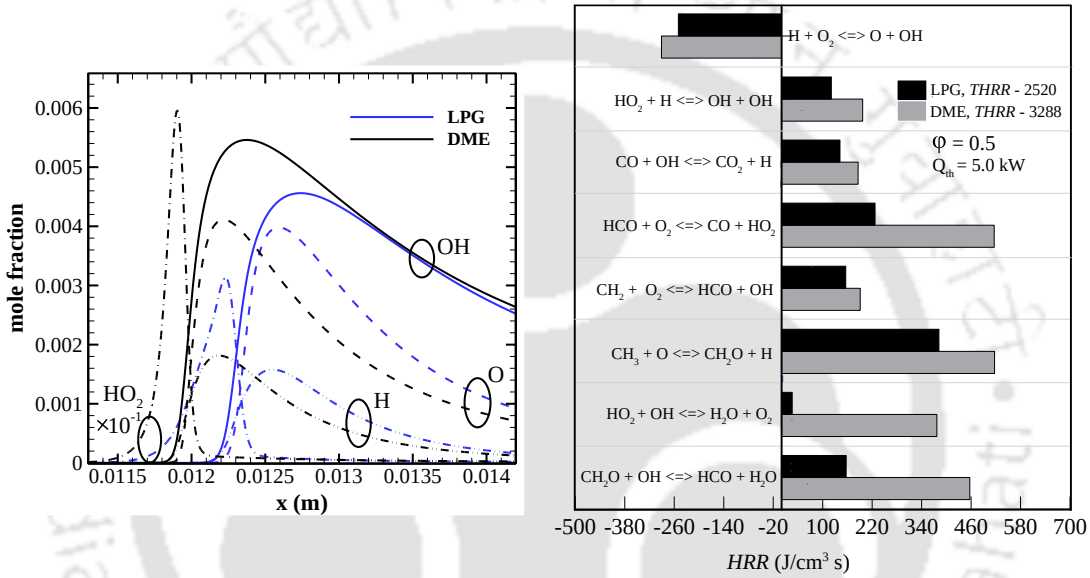

(a) (b)

Fig. 5.2. (a) Comparisons of concentrations of active free radicals along the PIB for LPG and DME flames, **(b)** The *HRR* of the most important reactions responsible for the increase in *THRR* for the DME flame inside the burner.

With reference to Fig. 5.3a, for $\varphi = 0.4$ the measured radiant efficiency varies from 19% - 23% for DME flame and from 17.5% - 21% for LPG fired PIB. While for $\varphi = 0.5$ radiant efficiency is in the range of 16.1% - 19% and 14.6% - 16.8% for DME and LPG fired PM respectively. Moreover, for all cases, the η_{rad} of the PIB with the DME-air flame is found to be higher than that of LPG fired PIB stove. A maximum radiation efficiency of $\eta_{rad} = 23\%$ has been measured for the DME combustion inside PIB at the fuel-lean condition, $\varphi = 0.4$ and Q_{th} = 1.4 kW, while for LPG-air combustion this value is $\eta_{rad} = 21\%$. This indicates that higher radiant efficiency can be achieved in the PIB stove

by using DME instead of LPG. Whereas, not much improvement in η_{th} is observed for DME flame compared to the LPG flame inside the PIB as shown in Fig. 5.3b.

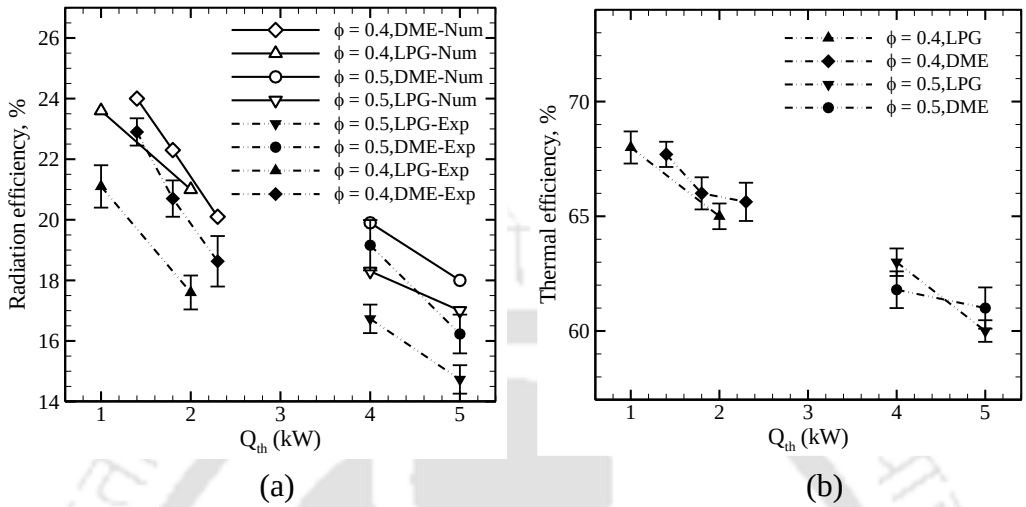

(a) (b)

Fig. 5.3. The comparisons of the influence of φ and Q_{th} on the **(a)** η_{rad} and **(b)** η_{th} of the PIB for LPG and DME fuels.

5.1.4. Chemical structure of DME flames in the PIB under ultra-lean conditions

From the above experimental and numerical investigations, it can be established that from the viewpoint of higher η_{rad} and lower CO emission, ultra-fuel-lean DME-air mixture with $\varphi = 0.4$ is the most desirable operating condition for the PIB stove. It is also observed that, on the basis of η_{rad} the PIB yields better performance at lower thermal load Q_{th} = 1.4 kW for the same equivalence ratio $\varphi = 0.4$. Thus in the following, to assess the superiority of ultra-lean DME-air combustion within the PIB under lower thermal load condition, comprehensive kinetic structure of the flame through reaction path, heat release rate and rate of product analysis are compared at two different power input conditions Q_{th} = 1.4 kW and Q_{th} = 2.28 kW for the same equivalence ratio $\varphi = 0.4$.

For lower thermal load Q_{th} = 1.4 kW the flame is stabilized at the upstream section of the interface of the PIB and located closer to the upstream end of the Al_2O_3 section as compared to higher thermal load case as seen in Fig. 5.4a. Figure 5.4c shows the heat recirculated to the incoming DME-air mixture in the preheat zone via convection h_v (T_g – T_s) from the solid-phase to the gas-phase of the PIB, while Fig. 5.4d illustrates the various

preheat efficiencies at $\varphi = 0.4,$ under thermal load input of Q_{th} = 1.4 kW and 2.28 kW. It can be seen from the figure that the preheat conduction efficiency, preheat radiation efficiency and thus the heat recirculation efficiency is more at lower Q_{th}. This leads to an increase in conduction and radiation feedback from the combustion zone to the Al_2O_3 region, which ultimately increases the combustion efficiency that leads to a higher η_{rad} (Fig. 5.3) for Q_{th} = 1.4 kW.

Figure 5.4a compares the measured and computed temperature profiles of DME fired PIB stove at $\varphi = 0.4,$ and under thermal load input of Q_{th} = 1.4 kW and 2.28 kW, while their respective overall heat release rates are illustrated in Fig. 5.4b as a function of axial distance. With reference to Fig. 5.4a, at higher thermal power input (Q_{th} = 2.28 kW), both experiment and the numerical results show higher temperature values at the combustion zone (T_3) and at the post-flame zone (T_4 and T_5) of the PIB burner. Whereas, in the preheat region (T_2) higher temperature is observed at the lower thermal load Q_{th} = 1.4 kW. Furthermore, from Fig. 5.4b it is seen that heat release rate profile attains two peaks when the PIB is operated under lower thermal load (Q_{th} = 1.4 kW). A minor heat release rate peak (Peak-$I_{1.4\ kW}$) in the preheat section (Al_2O_3) and a major heat release rate peak (Peak-$II_{1.4\ kW}$) at the interface of the two sections of the burner are observed in the figure. Whereas only one peak (Peak-$II_{2.28\ kW}$) can be seen for the heat release rate at the interface of the PIB under high thermal load condition (Q_{th} = 2.28 kW). It follows from Fig. 5.4a and 5.4b that, the higher preheat temperature in case of the lower thermal load is due to the existence of minor heat release rate peak (Peak-$I_{1.4\ kW}$) in the preheating region, which is absent for the high thermal load condition.

In order to explore the important reactions responsible for the formation of heat release rate peaks at various locations along the PIB, the percentage contributions of the major reactions to the total heat release rate are presented in Fig. 5.5a. In addition, Fig. 5.5b compares the concentration profiles of highly active free radicals produced at the preheat zone (Al_2O_3 section) and combustion zone (SiC section) of the PIB for Q_{th} = 1.4 kW and Q_{th} = 2.28 kW. From Fig. 5.5b it can be seen that, when the PIB is operated at Q_{th} = 1.4 kW, large parts of methoxymethyl radical (CH_3OCH_2) and Hydroperoxyl (HO_2) radicals are formed in the preheating region, while OH and H free radicals are produced in the

combustion zone. Whereas for Q_{th} = 2.28 kW, all free radicals (CH_3OCH_2, HO_2, OH and H) are manifested in the combustion zone of the PIB.

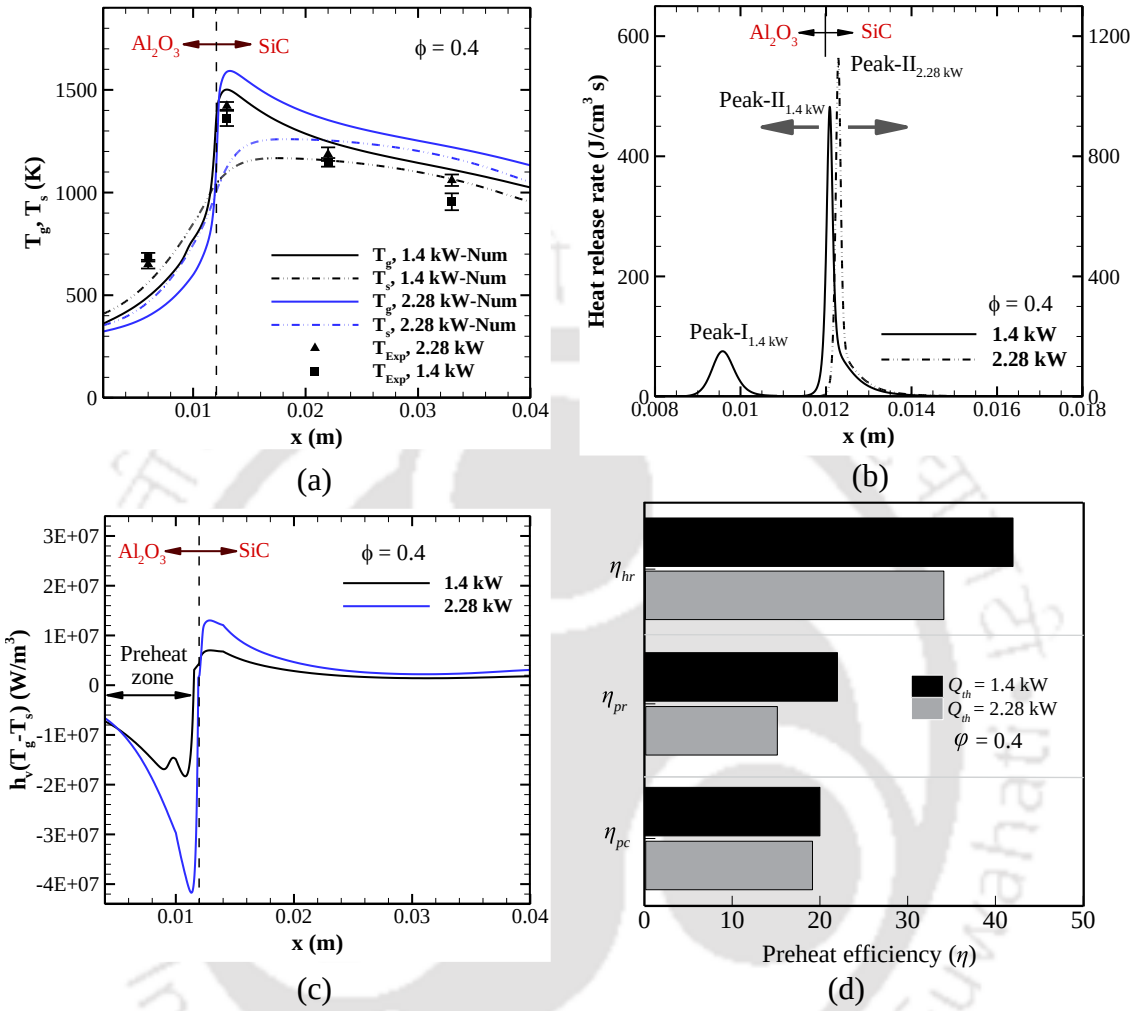

Fig. 5.4. (a) The comparisons of the measured and computed temperature profiles of DME fired PIB stove, **(b)** overall heat release rate profiles, **(c)** convective heat transfer rate between the solid and gas-phase of the burner and their **(d)** preheat efficiencies at $\varphi = 0.4$, under thermal load of Q_{th} = 1.4 kW and 2.28 kW.

For lower thermal load, in the preheat region CH_3OCH_2 and HO_2 radicals attain their peak values at the same location where the heat release rate achieves Peak-$I_{1.4\ kW}$. At this location, the low-temperature reactions $CH_3OCH_2 + O_2 \rightleftarrows CH_3OCH_2O_2$, $CH_3OCH_3 + OH \rightleftarrows CH_3OCH_2 + H_2O$ and $CH_2OCH_2O_2H \rightleftarrows CH_2O + CH_2O + OH$ are found to contribute significantly to the resultant heat release (Peak-$I_{1.4\ kW}$) within the Al_2O_3 section. Here almost 32% of the total heat is released due to the contribution of CH_3OCH_2 radical through the reaction $CH_3OCH_2 + O_2 \rightleftarrows CH_3OCH_2O_2$. In the preheat section HO_2 reacts

with H atom to produce hydroxyl radicals, via $HO_2 + H \rightleftarrows OH + OH$, which in turns undergoes H-abstraction reaction with DME generating methoxymethyl radical, through $CH_3OCH_3 + OH \rightleftarrows CH_3OCH_2 + H_2O$, which is also responsible for 19% of the total heat release generated at this location. In addition, 19.5% of the resultant heat is released during the β-scission reaction $CH_2OCH_2O_2H \rightleftarrows CH_2O + CH_2O + OH$ in the preheating region. Whereas the isomerization reaction $CH_3OCH_2O_2 \rightleftarrows CH_2OCH_2O_2H$ is the most endothermic reaction absorbing almost 12% of the released heat in the Peak-$I_{1.4\ kW}$ region for lower thermal load input. For Q_{th} = 2.28 kW, in the combustion zone peak mole fractions of all the intermediate radicals exhibit higher values than that of lower thermal load case (Q_{th} = 1.4 kW), thus increasing the total heat release rate at the interface of the PIB (Peak-$II_{2.28\ kW}$) for higher wattage, through the high temperature combustion reactions $CH_3 + O \rightleftarrows CH_2O + H$, $HCO + O_2 \rightleftarrows CO + HO_2$, $HO_2 + OH \rightleftarrows H_2O + O_2$ and $CH_2O + OH \rightleftarrows HCO + H_2O$, as seen in Fig. 5.5.

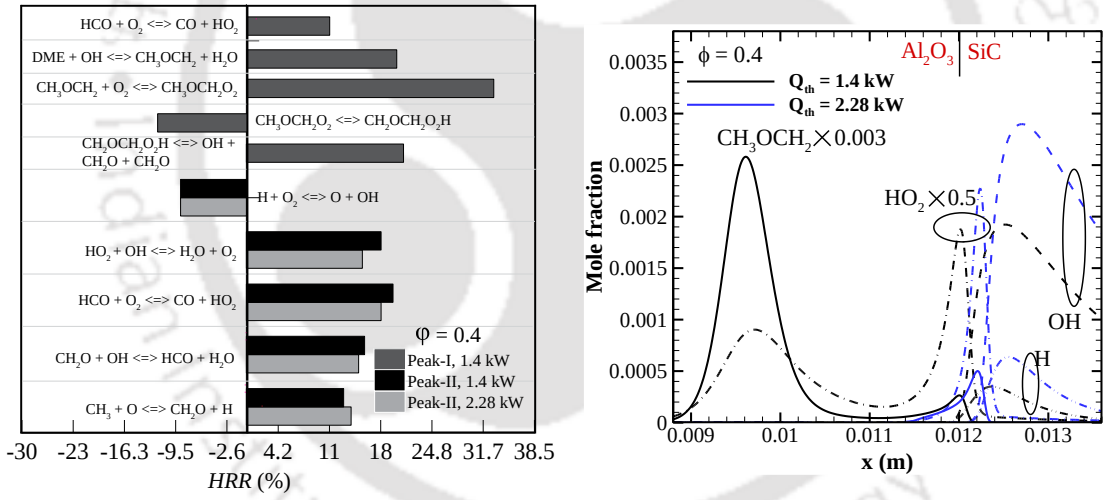

Fig. 5.5. (a) The percentage contributions of the major reactions to the total heat release rate and **(b)** the concentration profiles of free radicals formed in the Al_2O_3 and SiC section of the burner for Q_{th} = 1.4 kW and Q_{th} = 2.28 kW.

From the above investigation of heat release rate and the radical pool concentration profiles, it is quite evident that the formation of various low and high-temperature reactions depend on the availability of highly active free radicals in the preheating zone and combustion zone of the PIB stove. Thus in order to gain insight into the major reactions that are being developed at a different region of the PIB, Figs. 5.6 and 5.7 illustrate the main reaction pathways of the DME-air combustion under ultra-lean

condition $(\varphi = 0.4)$. In Fig. 5.6, for Q_{th} = 1.4 kW the reaction path analyses of the DME-air mixture are studied at burner location of x = 0.00959 m in the preheat section Al_2O_3, where the heat release rate profile achieves Peak-$I_{1.4kW}$ at a gas-phase temperature of T_g =733K. Figure 5.7 compares the reaction pathway of DME decomposition in the combustion zone (SiC) of the PIB stove, at the location where the heat release rate profiles attain Peak-$II_{2.28\ kW}$, corresponding to the gas-phase temperature of T_g = 1357K and T_g = 1440K, for the thermal load inputs Q_{th} = 1.4 kW and Q_{th} = 2.28 kW respectively.

For Q_{th} = 1.4 kW, the DME oxidation starts inside the preheater section 2.41 mm further from the interface of the PIB at a gas-phase temperature of T_g =733K. With reference to the Fig. 5.6, the decomposition process of the DME is initiated by hydrogen abstraction reaction primarily through OH radicals (90%) producing methoxymethyl radical (CH_3OCH_2), via $CH_3OCH_3 + OH \rightleftarrows CH_3OCH_2 + H_2O$. Here a large part of CH_3OCH_2 is consumed by O_2 molecules via $CH_3OCH_2 + O_2 \rightleftarrows CH_3OCH_2O_2$, yielding methoxymethyl-peroxy ($CH_3OCH_2O_2$), while the remaining CH_3OCH_2 radicals decompose through β-scission reaction to form formaldehyde (CH_2O) and methyl (CH_3) radicals through $CH_3OCH_2 \rightleftarrows CH_2O + CH_3$. At this location, the resultant $CH_3OCH_2O_2$ radical undergoes isomerization to generate hydroperoxy-methoxymethyl ($CH_2OCH_2O_2H$) radical, via $CH_3OCH_2O_2 \rightleftarrows CH_2OCH_2O_2H$, which in turn, is consumed by the β-scission reaction $CH_2OCH_2O_2H \rightleftarrows CH_2O + CH_2O + OH$. Some of the $CH_2OCH_2O_2H$ radicals also react with O_2 forming $O_2CH_2OCH_2O_2H$ radical. The resultant $O_2CH_2OCH_2O_2H$ radical subsequently decomposes to produce CO via the pathways; $O_2CH_2OCH_2O_2H \rightarrow HO_2CH_2OCHO \rightarrow OCH_2OCHO \rightarrow HOCH_2OCO \rightarrow HOCH_2O \rightarrow HCOOH \rightarrow CO$. The CH_2O radical formed in this preheat region mainly reacts with OH (88%) to produce Formyl radical (HCO), which in turns reacts with O_2 generating CO, through $HCO + O_2 \rightleftarrows CO + HO_2$. From the above mentioned pathways, only the reactions containing the intermediates CH_3OCH_2, $CH_3OCH_2O_2$, $CH_2OCH_2O_2H$, and CH_2O are important, contributing significantly to the net heat release rate in the preheat region as discussed before. Whereas, contributions of other intermediate species are nominal.

From Fig. 5.7 it is observed that the low-temperature reaction paths are completely vanished in the combustion zone of the PIB stove at a gas-phase temperature of T_g = 1357K and T_g = 1440K, for Q_{th} = 1.4 kW and Q_{th} = 2.28 kW respectively. At this location,

DME undergoes hydrogen abstraction reaction by H, OH, O, and CH_3 radicals to produce CH_3OCH_2. All the resultant CH_3OCH_2 radicals are decomposed here by β-scission reaction $CH_3OCH_2 \rightleftarrows CH_2O + CH_3$ generating CH_2O and CH_3 radicals. Then the resultant CH_3 recombines to produce ethane (C_2H_6) or reacts with CH_2O, HO_2, and DME to generate methane (CH_4) in this region of the PIB. Some of the CH_3 are also consumed by O, HO_2 and OH free radicals yielding formaldehyde via $CH_3 + O \rightleftarrows CH_2O + H$, methoxy via $CH_3 + HO_2 \rightleftarrows CH_3O + OH$, and singlet methylene ($CH_2(s)$) through $CH_3 + OH \rightleftarrows CH_2(s) + H_2O$ respectively. The resultant $CH_2(s)$ is then converted to more stable triplet methylene (CH_2), which in turns reacts with O_2 molecule to generate Formyl radical (HCO). HCO is also formed due to the H-atom abstraction reaction $CH_2O + (H, OH) \rightleftarrows HCO + (H_2, H_2O)$. This HCO is subsequently consumed by O_2 and is decomposed to generate CO, via $HCO + O_2 \rightleftarrows CO + HO_2$ and $HCO + M \rightleftarrows H + CO + M$ respectively.

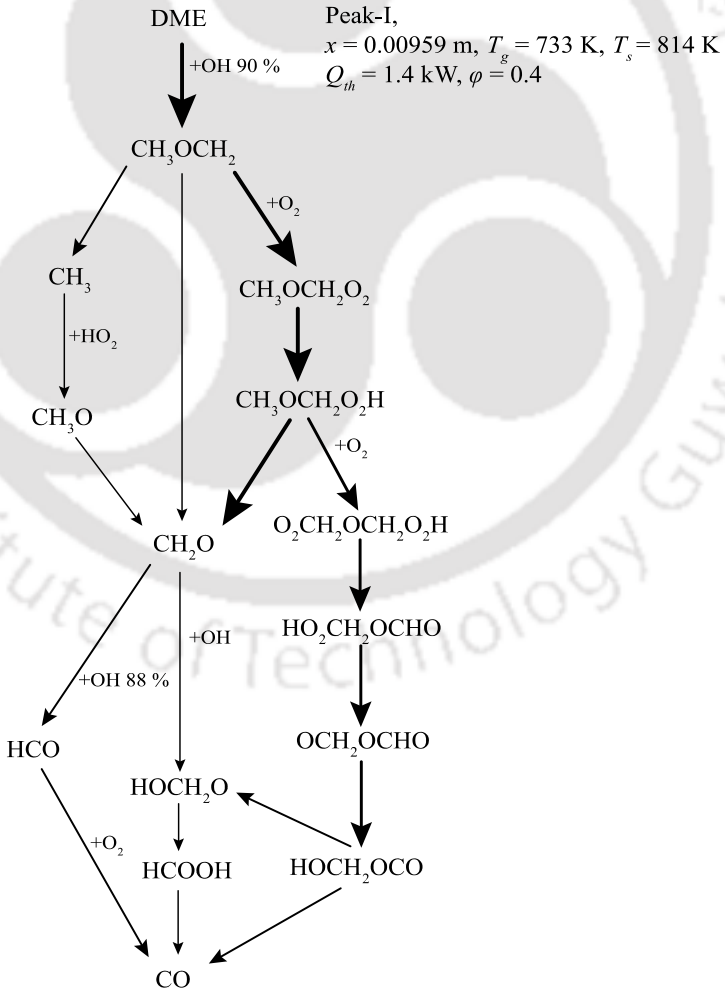

Fig. 5.6. The main reaction pathway of the ultra-lean DME flame in the Al_2O_3 section.

Ultimately CO is consumed by the reaction CO + OH ⇄ CO_2 + H producing CO_2 in the downstream section of the PIB burner. At this region CO_2 is also produced from formaldehyde through the pathway $CH_2O \rightarrow HOCH_2O \rightarrow HCOOH \rightarrow CO_2$, as shown in Fig. 5.7. With reference to Fig. 5.7, the fraction of intermediate species that are being consumed by OH, O_2 and HO_2 radicals exhibits higher value at the lower thermal load condition Q_{th} = 1.4 kW, whereas percentage contributions of H, O and CH_3 radicals are observed to be more in the case of higher thermal load input Q_{th} = 2.28 kW.

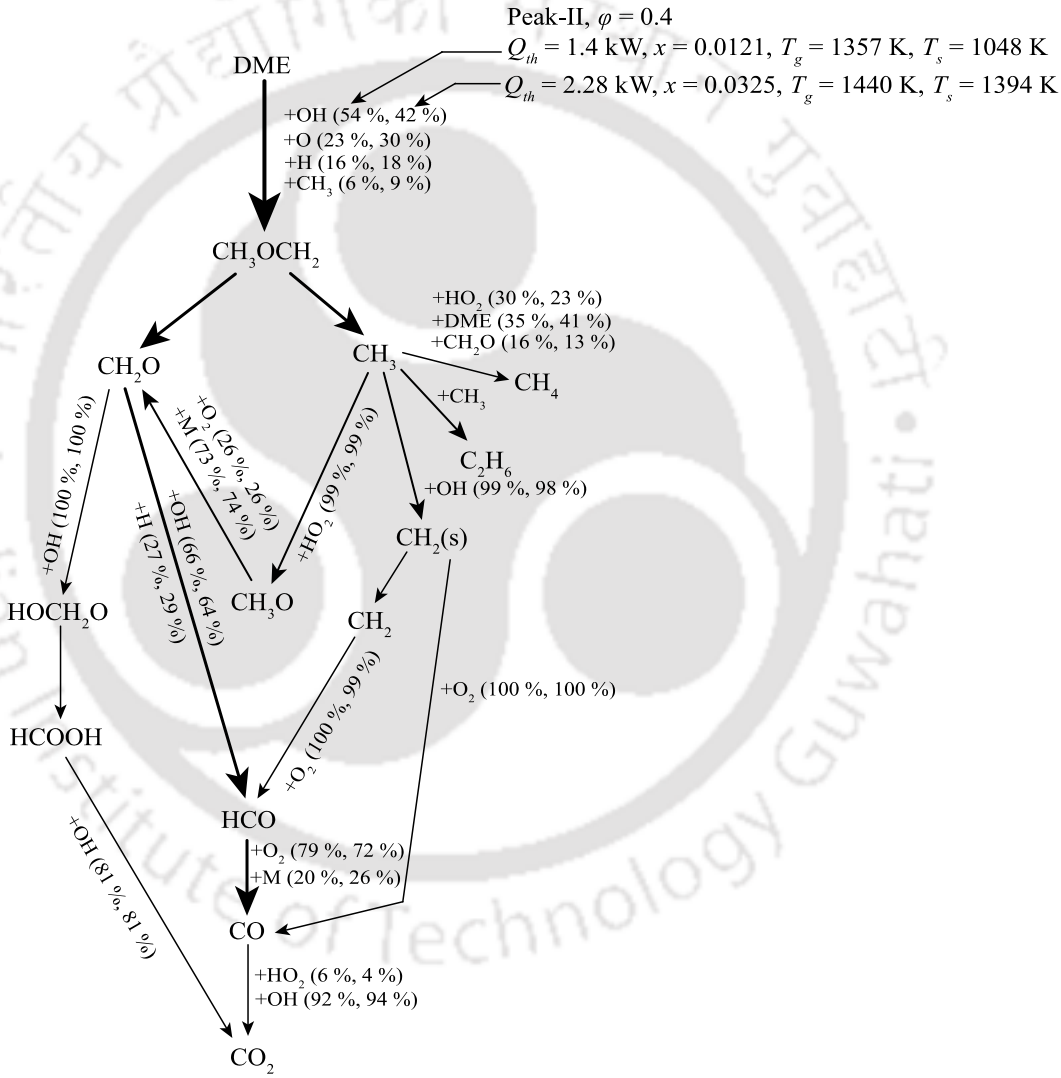

Fig. 5.7. The main reaction pathways of DME-air combustion under ultra-lean condition $(\varphi = 0.4)$ in the SiC section for Q_{th} = 1.4 kW and Q_{th} = 2.28 kW. The percentage values above the arrows indicate the fraction of parent species that are being consumed by various radicals.

5.2. Summary

To establish the advantage of the DME combustion than the LPG combustion in the PIB integrated stove, the thermal performances in terms of radiative efficiency, thermal efficiency, recirculation efficiency as well as CO emissions of the burner were compared for various equivalence ratios and thermal load input conditions. Both the experimental measurements and the numerical predictions showed lower CO emissions for DME flame than that of LPG flame inside the PIB. Moreover, the total heat generation rate, recirculation and radiant efficiencies of the burner with DME flame were found to be higher than that of the LPG. Two peaks for heat release rate profiles were observed when the PIB was operated under lower thermal load at the ultra-fuel-lean condition, whereas only one peak was observed for the heat release rate profile at the interface of the two-layer burner under high thermal load condition. In order to explore the important reactions responsible for the formation of heat release rate peaks at various locations along the burner, reaction pathway analyses were carried out through detail kinetic mechanism.

CHAPTER 6

SOOT FORMATION IN PIB

Despite the increasingly wide application of PMC technique, its effect on soot formation and growth mechanism remains unclear. This is due to the difficulties arises in performing experiments for visualizing and measuring the soot particle evolution inside the PM, as well as because of challenges in numerical simulation associated to the complication in interpreting the soot formation mechanism in such highly conducting and radiating environment of the PIB. Indeed, in FF combustion soot is known to be generated near the reaction zone of flame through the nucleation and then by surface growth, and subsequently, it grows in the post-flame zone forming aggregates, via coalescence and particle agglomeration mechanism.

To demonstrate the effect of PIB on soot evolution process, in this Chapter the variations of soot volume fraction, particle number density, soot particle diameter, and concentration profiles of some important soot precursors such as benzene, naphthalene and pyrene generated inside the PM due to combustion of a simple unsaturated hydrocarbon fuel C_2H_4 are investigated. In the following, production of various PAHs and soot particulates along the burner axis and at the burner exit are compared to that of FF case at the same operating conditions. The conceptual schematic of the analyses is illustrated in Fig. 6.1. The dependence of equivalence ratio, flame speed and temperature of PIB on the soot formation behavior and its precursors are also extensively scrutinized in this Chapter. Furthermore, the sensitivities of soot volume fraction, number density,

particle diameter and PAHs concentration to various thermal and optical properties of the porous burner are investigated.

6.1. Numerical Method and Kinetic Model Selection

As schematically illustrated in Fig. 6.1, the computational domain consists of a 1-D planer PM with a thickness equal to L=0.03 m. Fuel-rich C_2H_4-air mixture stream is injected into the porous burner inlet at a pressure of 1 atm and temperature of 298.15 K. In no time the combustion spreads throughout the PIB, and eventually, depending on the velocity and equivalence ratio of the incoming C_2H_4-air mixture the flame stabilizes at a particular location inside the burner.

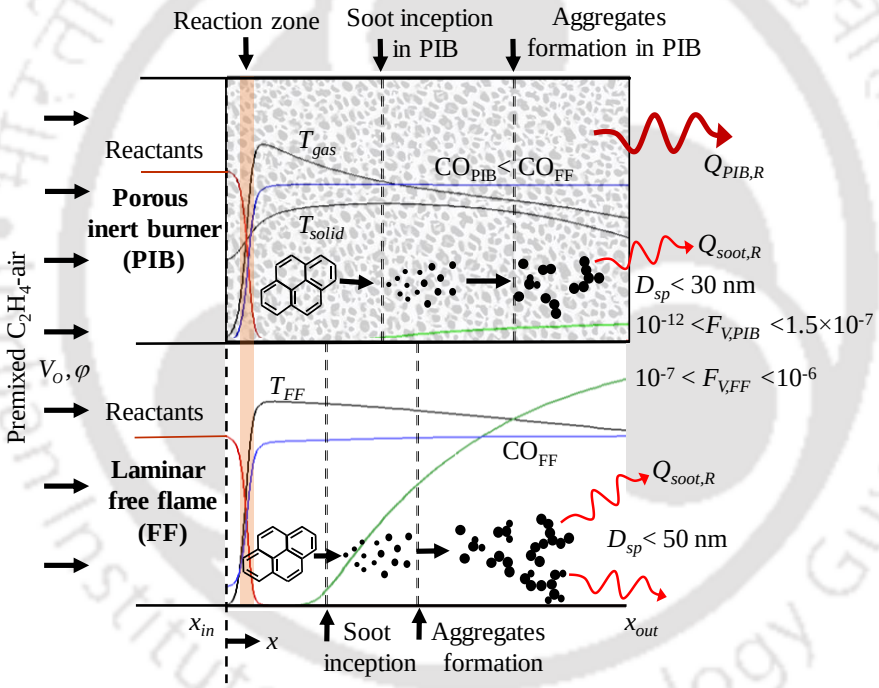

Fig. 6.1. Conceptual illustration of the comparisons of soot growth process within PIB and FF combustion.

The present model solves the RTE solver to account for the volumetric radiation from the solid phase of the PIB, and the effect of radiation from H_2O, CO_2 species, and soot particles are computed considering optical thin model and grey gas approximation [118]. To interpret the effect of the PIB on soot evolution, in this Chapter a comprehensive kinetic mechanism [119] consisting of 156 chemical species and 5600 different reactions is used. The discrete sectional method (DSM) based soot kinetic model used in this study

couples a gas-phase mechanism [120], which contains 97 species including PAHs up to pyrene ($C_{16}H_{10}$) and heavy PAHs, and a detailed soot chemistry [121] consisting of 59 pseudo species (BINs) for describing the soot growth process.

The energy equation for the gas-phase of the PIB is governed by,

$$\xi\rho_g C_g\left(\frac{\partial T_g}{\partial t}+u\frac{\partial T_g}{\partial x}\right)+\sum_{k=1}^{K}\xi\rho_g Y_k C_{g,k} V_k\frac{\partial T_g}{\partial x}+\sum_{k=1}^{K}\xi\dot{\omega}_k h_k W_k+h_V(T_g-T_s) = \frac{\partial}{\partial x}\left(\xi\lambda_g\frac{\partial T_g}{\partial x}\right)+\frac{\partial \dot{Q}_{g,R}}{\partial x}+\frac{\partial \dot{Q}_{soot,R}}{\partial x} \tag{6.1}$$

where the last two term represent the volumetric radiation heat losses due to the gas species and soot particles. Under the optical thin and grey gas approximation, considering radiative heat transfer only from major radiating chemical species like H_2O, and CO_2, as well as from soot particles, the radiative source terms is given by,

$$\frac{\partial \dot{Q}_{g,R}}{\partial x}+\frac{\partial \dot{Q}_{soot,R}}{\partial x}=2\sigma\left(T^4-T_0^4\right)\sum_k p_k\kappa_{p,k} \tag{6.2}$$

where $\sigma=5.67\times10^{-8}\,\mathrm{W\cdot m^{-2}\cdot K^{-4}}$ represents the Stefan-Boltzmann constant, T_0 is the ambient temperature, p_k is the partial pressure, and $\kappa_{p,k}$ is the Planck mean absorption coefficient for the k^{th} species. At every grid point, the temperature dependent Planck mean absorption coefficient for all species is computed by,

$$\sum_k p_k\kappa_{p,k}=p\left[X_{CO_2}\kappa_{p,CO_2}(T)+X_{H_2O}\kappa_{p,H_2O}(T)+F_V\kappa_{p,soot}(T)\right] \tag{6.3}$$

where X_k is the mole fraction of k^{th} species and F_V is the soot volume fraction. In Eq. 6.3 the $\kappa_{p,k}$ of each species is estimated based on polynomial lines as adapted from [122], and $\kappa_{p,soot}(T)$ is calculated as [123],

$$\kappa_{p,soot}(T)=\left[-3.75\times10^5+1735T(x)\right]\ \mathrm{m^{-1}} \tag{6.4}$$

6.2. Model Results and Discussions

In this section, first the soot growth process including the soot volume fraction, particle number density, soot particle diameter distributions and PAHs concentration profiles as a function of the burner axis of the PIB are compared to that of premixed FF combustion at the same input conditions. Moreover, the rate of production analyses of various soot components along the flame axis are carried out to show the distinction between FF and PMC for different soot evolution mechanisms. Following this, the effect of equivalence ratio, flame speed, and gas-phase temperature of the PIB on different soot growth-related parameters are also reported. Finally, the influence of different thermal-physical and optical properties of the SiC PM on the soot evolution dynamics are discussed through sensitivity analyses.

6.2.1. Soot inception within the PIB

The computed axial gas and solid-phase temperature profiles of the PIB for the combustion of the rich premixed C_2H_4-air mixture are reported in Fig. 6.2a, where the steep decrease in gas temperature can be observed in down-stream section of the burner caused by the radiation losses primarily from the highly radiating SiC PM and secondary from the soot particles. In addition, the sooting behavior of the flame inside the PIB in terms of soot volume fraction (F_V) is provided in Fig. 6.2a as a function of the axial distance of the burner. Further, for the sake of comparison, the FF temperature profile and F_V distribution of the premixed C_2H_4-air combustion in the gaseous environment are shown along with its combustion inside the PIB at the same equivalence ratio of $\varphi = 2.4$, and input cold gas flow velocity of V_{0L} = 0.1198 m/s. The gas-phase temperature falls more rapidly inside the PIB as compared to its FF temperature, which in turns slows the increase in soot volume fraction along the burner axis. Moreover, the lower temperature at the post-flame region of the PIB is responsible for the later manifestation of the soot volume fraction which is regulated by larger BINs generation, that starts at ≈ 4.0 mm further down-stream from the soot inception region of the FF case.

In aerosol dynamics, at first small soot particles are formed from the higher PAH species through nucleation mechanism, followed by surface growth, dehydration, oxidation and in the later stage of the soot evolution process, larger particles are formed due to

agglomeration. From these mechanisms, only soot nucleation increases the soot number density (N_D) at the initial stage and the other processes progressively decrease the number density and favor the increment of average soot particle sizes in the post-flame region. Figure 6.2b supports these observations, where the number densities and soot particle diameter $\left(D_{SP} = \left(\frac{6F_V}{\pi N_D \times 10^6} \right)^{1/3} \text{nm} \right)$ are plotted along the burner axis for the combustion of the rich C_2H_4-air mixture inside the PIB and in FF condition at $\varphi = 2.4$ and V_{0L} = 0.1198 m/s. In the case of PIB, the prominent decline in N_D profile and slower growth of particle size D_{sp} along the burner axis than that of FF mode is evident from the Fig. 6.2b. It is also observed that within the PIB the N_D attains its peak value more quickly as compared to the FF case. This is owing to the fact that, the earlier termination of nucleation process inside the PIB caused by the lower gas-phase temperature, subsequently decreases the growth rate of soot number density, as shown in Fig. 6.2b.

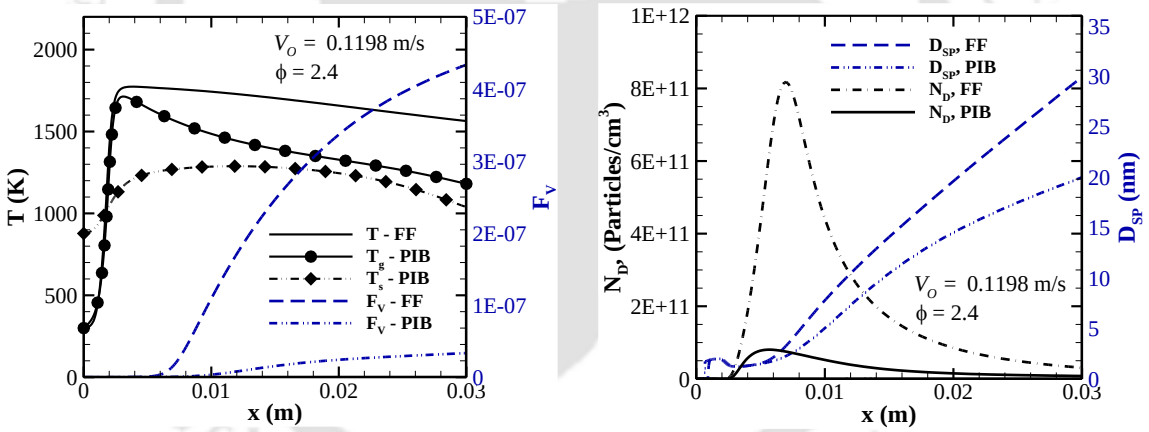

Fig. 6.2. Comparisons of axial **(a)** gas and solid-phase temperature profiles, soot volume fractions **(b)** particle number densities and soot diameters as a function of burner distance for $\varphi = 2.4$ and V_{0L} = 0.1198 m/s.

As mentioned in previous Chapters, porous burners are usually characterized by their ability to reduce CO emission as compared to conventional burners. Figure 6.3b confirms this claim, where the CO concentration profile for C_2H_4-air combustion inside the PIB is compared with its combustion in FF mode at $\varphi = 2.4$, and V_{0L} = 0.1198 m/s. In addition, to explore the effect of PIB on PAH and soot formation, the mole fraction profiles of some major soot precursors such as benzene (C_6H_6), Naphthalene ($C_{10}H_8$), Pyrene

($C_{16}H_{10}$), and the concentration profiles of various BINs produced along the burner axis for both PIB and FF are compared in Figs 6.3c and 6.3d respectively. It can be seen from Fig 6.3c that, the C_2H_4 flame inside the PIB generates higher amount of PAHs (C_6H_6, $C_{10}H_8$, $C_{16}H_{10}$) than that of FF combustion under the examined input condition.

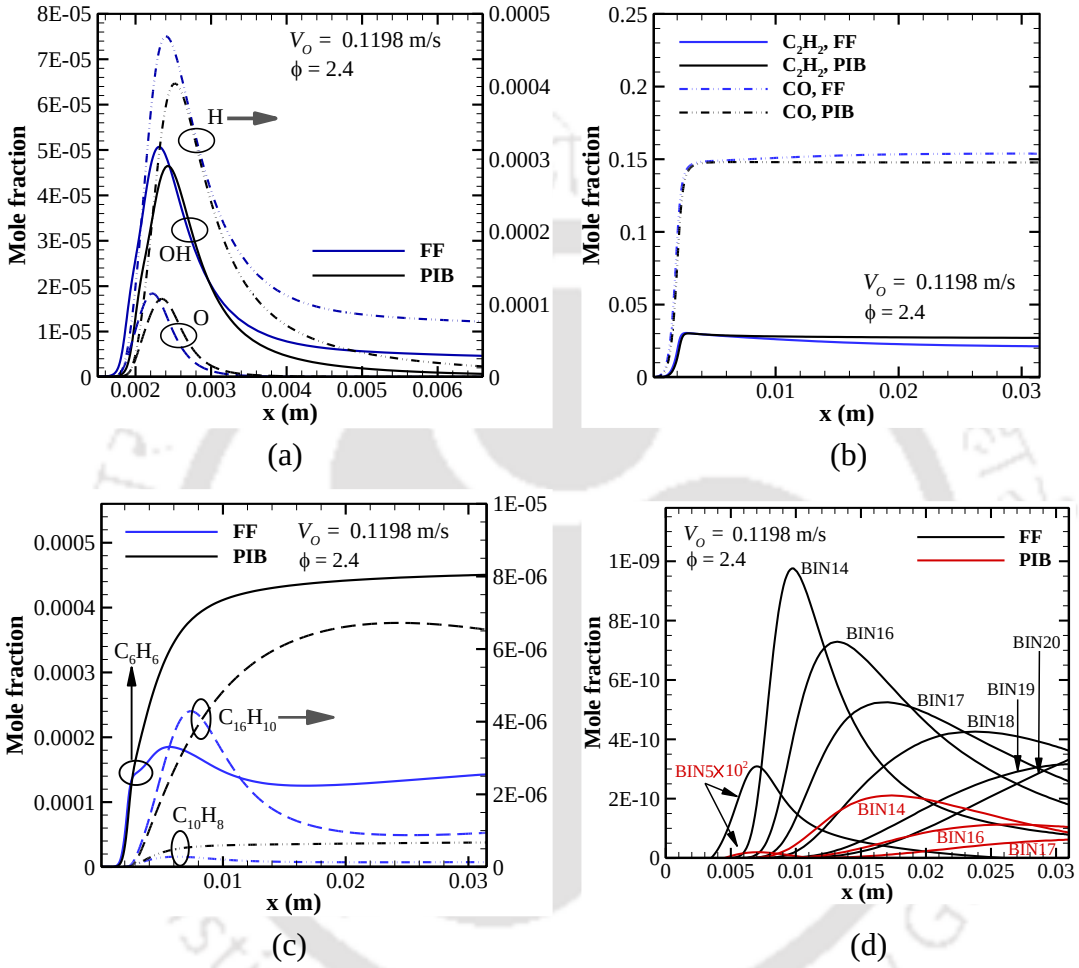

Fig. 6.3. Comparisons of concentration profiles of (a) free radicals (O, OH, H), (b) CO, C_2H_2 species, (c) major PAHs (C_6H_6, $C_{10}H_8$, $C_{16}H_{10}$), (d) soot particles and aggregates in terms of various BIN classes along the flame axis inside PIB and in FF condition.

The larger concentration of PAHs in the PIB results from the presence of higher concentration of C_2H_2 in the downstream region of the burner (Fig. 6.3b), which is responsible for the formation of first aromatic ring formation. Moreover, Fig. 6.3c shows that, mole fractions of all the PAHs follow rise-decay profile during combustion of C_2H_4-air mixture in the FF mode, whereas, in the case of PIB, after attaining the peak values

the concentrations of PAHs is observed to remain almost constant throughout the burner. This is attributed to the fact that, the lower peak and post-flame temperature and less abundances of highly active free radicals (OH, H and O) in the post-flame region (Fig. 6.3a) of the PIB prevent further oxidation of PAHs and favors the accumulation of the PAHs downstream of the burner increasing their concentration as compared the FF case.

The coagulation and agglomeration process of PAHs to form large soot particles are also depressed by the lower temperature distribution (Fig. 6.2a) and less prolonged presence of the free radicals (Fig. 6.3a) in the post-flame region of the PIB, that eventually results in lower amount soot formation in the PIB than that of FF case. To support this conclusion, in Fig. 6.3d the mole fractions of different soot particles (BIN5 - BIN13) and aggregates (BIN14 - BIN20) in terms of various BIN classes are presented for both PIB and FF combustion under the same input condition of $\varphi = 2.4$ and V_{0L} = 0.1198 m/s. The mole fractions of all the BINs formed inside the PIB along the burner axis are found to be very much less than that of the FF values. Fig. 6.3d also shows that with the combustion of the rich C_2H_4-air mixture within the PIB instead of its combustion in FF mode, the formation of the large aggregates beyond BIN17 totally disappear. Moreover, in case of PIB, the soot particles and the aggregates are evolved at a higher height above the burner, and they achieve their peak at the further downstream side of the burner as compared to the FF combustion.

To gain insight into the soot evolution mechanism within the PIB, in Figs. 6.4-6.6 the production rate analyses of soot particles BIN5, BIN10, and aggregate BIN17 are illustrated for the combustion of C_2H_4 in the PIB and FF condition, as well as the dominant reactions responsible for soot formation such as nucleation, surface growth, coalescence, agglomeration and oxidation of these BINs are summarized in the figures. From these figures, it is apparent that the production rate of all the BINs and the progress rate of major reactions associated with the formation of the BINs inside the PIB are orders of magnitude lower than that of FF case. BIN5 is considered as the smallest soot particle, that governs the particle nucleation in the soot evolution process. With C_2H_4 flame inside the PIB, the production rate profile of BIN5 and the progress rate profile of the reactions responsible for the nucleation (4.2a-4.2c), HACA mechanism (4.1a, b) and dehydration process (4.4) exhibit narrower domain width than the laminar FF, as shown

in Fig. 6.4. This is due to the presence of lower amount of H and H_2 species at this region of the PIB, which subsequently reduces the progress rate and reaction zone thickness of the H atom abstraction reaction BIN5C + H => H_2 + BIN5CJ (4.1a) and nucleation reactions H + BIN5CJ => BIN5C (4.2b) and H_2 + BIN5CJ => BIN5C + H (4.2c). The lower post flame temperature in the downstream section of the PIB reduces the consumption rate of dehydrogenation reaction BIN5C => H + BIN5CJ (4.4), leading to a decrease in soot radical (BIN5CJ) production that eventually hinders the growth process of soot within the PIB, via reactions 4.1b, 4.2a-c, and 4.3.

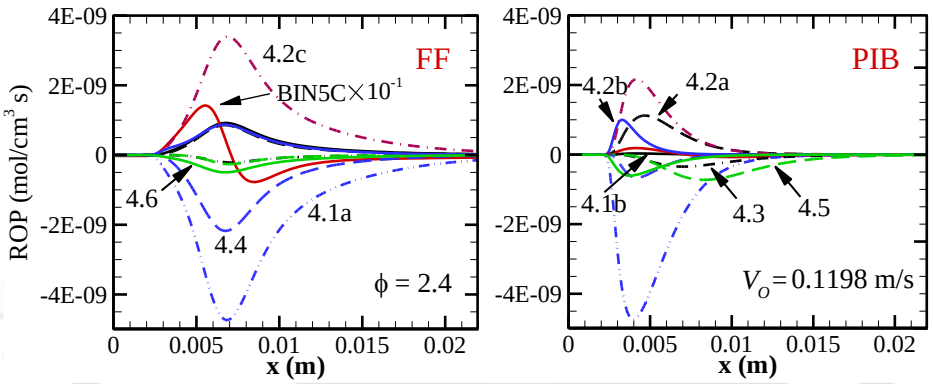

4.1. HACA Mechanism:

a. BIN5C + H => H_2 + BIN5CJ

b. C_2H_2 + BIN5CJ => 0.994 BIN5C + 0.0047 BIN6C + 0.0015 BIN6B + 0.61 H

4.2. Nucleation:

a. C_6H_6 + BIN5CJ => 0.93 BIN5C + 0.056 BIN5B + 0.013 BIN6C + 0.0055 BIN6B + H

b. H + BIN5CJ => BIN5C

c. H_2 + BIN5CJ => BIN5C + H

4.3. Surface growth/PAH condensation:

BIN5C + $C_{12}H_7$ => 0.892 BIN5C + 0.0695 BIN5B + 0.026 BIN6C + 0.0114 BIN6B + H

4.4. Dehydrogenation:

BIN5C => H + BIN5CJ

4.5. Coalescence:

BIN1B + BIN5C => 0.83 BIN5C + 0.11 BIN5B + 0.041 BIN6C + 0.021 BIN6B

4.6. Oxidation:

BIN5C + OH => H_2O + BIN5CJ

Fig. 6.4. ROP analyses of BIN5C along the flame axis of the PIB and FF combustion.

It can be seen from Fig. 6.5 that the production rate of surface growth and coalescence reactions (5.1a - 5.2f) which lead to the formation of larger soot particles BIN10B,

decrease inside the PIB, because of its lower flame temperature as compared to FF combustion. it is further observed that the thickness of surface growth and coalescence regions is broader within the PIB caused by the diminished reactivity of this zone due to the presence of low concertation of H, OH, O and BINs radicals than the FF case.

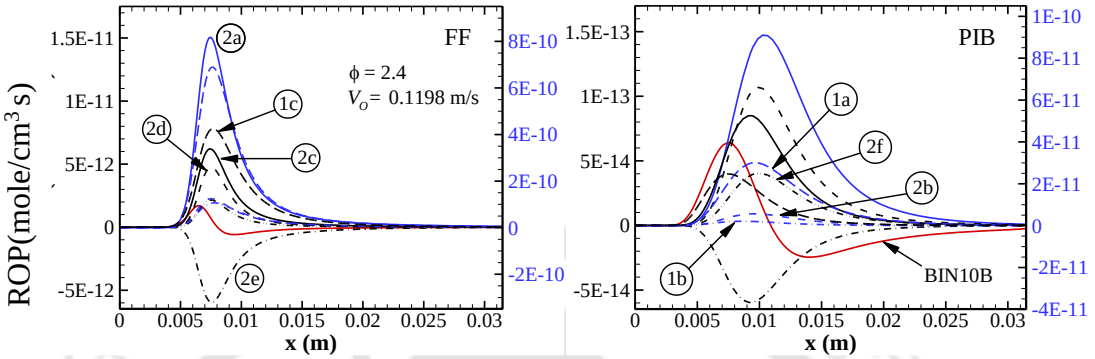

5.1. Surface growth/PAH condensation:

a. BIN9B + $C_{12}H_7$ => 0.99 BIN9B + 0.0028 BIN9A + 0.0019 BIN10B + 0.0004 BIN10A + H
b. BIN10C + $C_{12}H_7$ => 0.99 BIN10C + 0.0096 BIN10B + 0.0012 BIN11B + H
c. BIN10C + $C_{16}H_9$ => 0.986 BIN10C + 0.013 BIN10B + 0.0016 BIN11B + H

5.2. Coalescence:

a. BIN1B + BIN9B => 0.99 BIN9B + 0.0048 BIN9A + 0.0032 BIN10B + 0.00082 BIN10A
b. BIN1B + BIN10C => 0.98 BIN10C + 0.016 BIN10B + 0.002 BIN11B
c. BIN5C + BIN9B => 0.936 BIN9B + 0.051 BIN10B + 0.013 BIN10A
d. BIN5C + BIN10A => 14.02 H_2 + 0.024 BIN10B + 0.944 BIN10A + 0.032 BIN11A
e. BIN5C + BIN10B => 0.962 BIN10B + 0.006 BIN10A + 0.025 BIN11B + 0.0066 BIN11A
f. BIN6C + BIN9B => 0.0495 BIN9C + 0.82 BIN9B + 0.105 BIN10B + 0.023 BIN10A

Fig. 6.5. ROP analyses of BIN10B along the flame axis of the PIB and FF combustion. Blue colored plots are labeled on the right-hand side of the graphs.

In order to demonstrate the effect of PIB on soot agglomeration, Fig. 6.6 compares the production rates of BIN17B along the burner axis for the PIB and FF case, which represents the formation of large aggregate inside the burner. It can be seen that the production rate of large aggregate slows down and is not consumed inside the PIB. This is attributed to the less abundance of the free radicals at the downstream region of the PIB, which ultimately depresses the oxidation of soot aggregates by OH radicals through the reaction 6.4. Thus, depletion in mole fraction profile of BIN17B is not prominent in the case of PIB as observed in Fig. 6.3d.

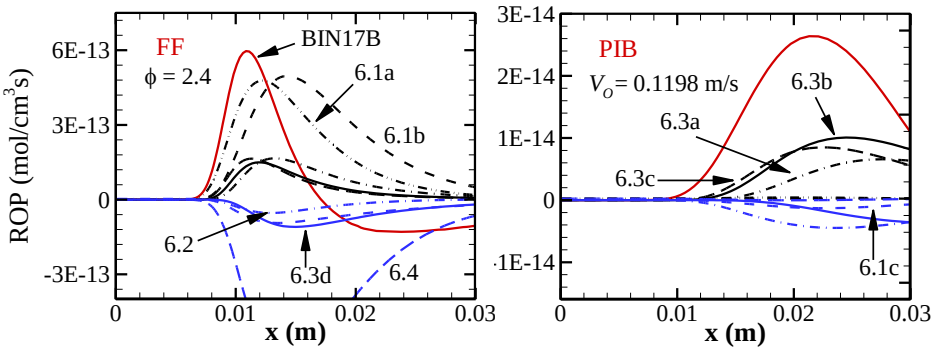

6.1. Surface growth/PAH condensation:

a. C_6H_6 + BIN16BJ => 0.999 BIN16B + 3.85e-05 BIN16A + 9.83e-06 BIN17B + 3.79e-10 BIN17A + H

b. C_6H_6 + BIN17BJ => 0.999 BIN17B + 1.97e-05 BIN17A + 4.8e-06 BIN18B + 9.5e-11 BIN18A + H

c. BIN17B + $C_{12}H_7$ => 0.999 BIN17B + 2.88e-05 BIN17A + 9.59e-06 BIN18B + 2.76e-10 BIN18A + H

6.2. Coalescence:

BIN1B + BIN17BJ => 0.99 BIN17B + 3.73e-05 BIN17A + 1.59e-05 BIN18B + 5.97e-10 BIN18A + H

6.3. Aggregation/Agglomeration:

a. BIN14B + BIN16B => 0.689 BIN16B + 0.049 BIN16A + 0.245 BIN17B + 0.017 BIN17A

b. BIN15B + BIN16B => 0.42 BIN16B + 0.053 BIN16A + 0.466 BIN17B + 0.058 BIN17A

c. 2 BIN16B => 0.976 BIN17B + 0.024 BIN18B

d. BIN16B + BIN17B => 0.488 BIN17B + 0.512 BIN18B

6.4. Oxidation:

BIN17B + OH => 1.64e-06 BIN16B + 0.999 BIN17B + 2.7e-07 BIN17A + HCO

Fig. 6.6. ROP analyses of BIN17B along the flame axis of the PIB and FF.

6.2.2. Influence of equivalence ratio on soot formation

The influence of φ on the final soot volume fraction, particle number density, average particle diameter, and the equilibrium concentrations of PAHs (C_6H_6, $C_{10}H_8$, and $C_{16}H_{10}$) has been studied at the surface of the PIB in Figs. 6.7a-c, by varying the φ from 2.1-3.0, correspond to the FF laminar velocity V_{0L} in the range of 0.1898 m/s - 0.068 m/s respectively. Further, to assess the advantage of PIB over FF combustion towards soot suppression, the computed F_V, $T_{g,max}$, N_D, D_{SP}, and equilibrium mole fraction values of PAHs for the combustion of C_2H_4-air mixtures within the PIB and FF mode are also compared at the same input conditions of φ and V_{0L}. As seen in Fig. 6.7a, the maximum predicted gas temperature, $T_{g,max}$ inside the PIB yields a lower value compared to the FF case for all equivalence ratios examined. With the C_2H_4 flame inside PIB, the final F_V and N_D are observed to be more than one order of magnitude lesser than their respective FF values, as illustrated in Figs. 6.7a, b. Moreover, the average diameter of soot particles at

the burner exit is also found to be less than half of that predicted in FF mode over the entire range of φ studied. In case of PIB the computed F_V and D_{SP} ranged from 5×10^{-10} to 3.4×10^{-8} and 2 nm to 22 nm, respectively, while for FF case the same are in range 10^{-7} - 10^{-6} and 4 nm - 51 nm, respectively, when operated under same input conditions. For PIB the maximum soot number density, N_D is found to be 8.12×10^{11} particles/cm^3, whereas for FF combustion the same is 1.13×10^{11} particles/cm^3 (see Fig. 6.7b).

Upon inspection of $F_V \sim \varphi$ plot from Fig. 6.7a, it is observed that for the combustion of the rich C_2H_4-air mixture inside PIB and FF, the F_V rises with increasing φ and attains the maximum value near $\varphi = 2.5$ and $\varphi = 2.8$, respectively, corresponding to the maximum gas temperature of about $T_{g,max} \approx 1660$ K.

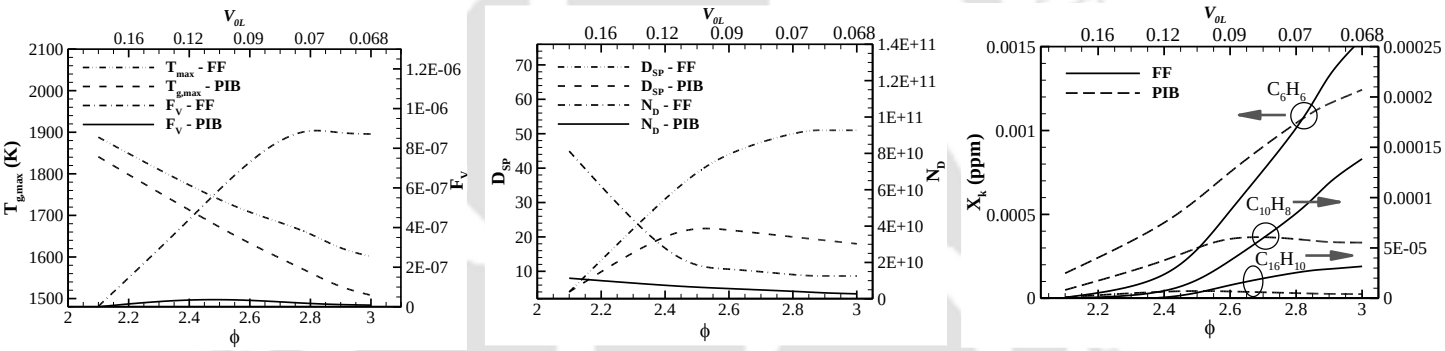

Fig. 6.7. (a) Comparisons of evolution of F_V with $T_{g,max}$, **(b)** variations of soot diameter (D_{sp}), number density (N_D), and **(c)** mole fraction distributions of C_6H_6, $C_{10}H_8$ and $C_{16}H_{10}$ for combustion of C_2H_4 inside PIB and FF mode as a function of φ. For all φ their respective laminar FF velocities (V_{0L}) are labelled on top side of the graphs.

In the case of PIB, for φ higher than 2.5 the F_V profile declines with decreasing $T_{g,max}$, while for FF mode the F_V is observed to be less sensitive to equivalence ratio towards the fuel-rich side of $F_V \sim \varphi$ curve $(\text{for}\,\varphi \geq 2.8)$. As seen in Fig. 6.7b, the $D_{SP} \sim \varphi$ curve displays the trends consistent with $F_V \sim \varphi$, that is, for PIB case D_{sp} exhibits bell-shaped profile, while in the FF case it becomes almost constant for higher φ values. Whereas, the soot number density decreases continuously with increasing φ in the examined range of $\varphi = 2.1-3.0$, for both PIB and FF mode combustion as shown in Fig. 6.7b. The decrease

in N_D can be explained by the drop in surface growth rate and aggregation rate due to the lower gas phase temperature for higher φ values.

Also reported in Fig. 6.7c are the equilibrium concentrations for three of the major PAHs, that include C_6H_6, $C_{10}H_8$, and $C_{16}H_{10}$, at the exit of burner domains as a function of φ for both PIB and FF cases. With the increase in φ the increment of the PAHs mole fractions in PIB becomes less steep as compared to the corresponding FF values and in between the studied equivalence ratio range of φ = 2.1 to φ = 3.0, there exist a critical equivalence ratio (φ_c) for each PAH, at which the PIB and FF combustion exhibit same equilibrium concentration value. These critical φ_c values for C_6H_6, $C_{10}H_8$, and $C_{16}H_{10}$ and their corresponding flame velocities (V_{0LC}) are summarized in Table 6.1. For equivalence ratios lower than the φ_c values, the PIB emits higher amount of PAHs emissions than the FF case. Conversely, for φ higher than the φ_c values, PIB yields lower PAHs pollutants than that of FF combustion. From Fig. 6.7c it is also worth noting that for higher carbon-containing PAHs the φ_c shift towards the fuel-lean side of $X_k \sim \varphi$ curve.

Table 6.1. Critical φ_c and V_{0LC} values for $X_k \sim \varphi$ curve (Fig. 6.7c)

PAHs	critical equivalence ratio (φ_c)	critical FF velocity (V_{0LC}), m/s
C_6H_6	2.8	0.07
$C_{10}H_8$	2.7	0.08
$C_{16}H_{10}$	2.5	0.105

6.2.3. Influence of flame velocity on soot evolution

Unlike the FF combustion where the flame stabilizes only for the burning velocity of the fuel-air mixture that exactly matches the laminar premixed velocity V_{0L}, owing to the improved heat transfer by conduction, convection, and radiation within the PM a wide range of fuel-air mixture velocities (filtration velocities V_0) can be attained in the PIB at a particular φ. To study the effect of filtration velocities on soot evolution inside the PIB, with C_2H_4 flames stabilized at their respective operating limits, Figs. 6.8a-c provide the F_V, N_D and D_{SP} at the burner exit as a function of V_0 for different φ in the range of 2.1-

3.0. In addition, the equilibrium concentrations of C_6H_6, $C_{10}H_8$, and $C_{16}H_{10}$ in the PIB for various φ are also investigated in Figs. 6.8d-f as a function of V_0.

Upon observation and analysis of Figs. 6.8a-f, it is evident that for all the cases, at a given V_0 the values of F_V, N_D, D_{SP}, and mole fractions for C_6H_6, $C_{10}H_8$ and $C_{16}H_{10}$ at the burner exit increases with increasing φ, and within the stable filtration velocity limits the peaks of the plots attain their maximum at $\varphi = 3.0$, with the exception of $N_D \sim V_0$ curve that exhibits maximum value at $\varphi = 2.6$ corresponding to V_0 = 0.3 m/s. Fig. 6.8a reports the final F_V along with the $T_{g,max}$ of the PIB as a function of V_0 for different φ. It indicates that for all equivalence ratios the soot volume fraction rises with increasing V_0 until it reaches the peak at $V_0 \approx$ 0.16 m/s where the $F_V \sim V_0$ plot approaches the maximum gas-phase temperature in the range of about $T_{g,max} \approx$ 1705 K - 1770 K, and at flame velocities higher than $V_0 \approx$ 0.16 m/s the F_V start to decline for a given φ. From Fig. 6.8a it is also observed that the final F_V at the PIB exit varies in the range of 10^{-12} - 1.5×10^{-7} under all the input conditions studied here, while for FF combustion the final soot volume fractions are more than that of PIB and are predicted to be in the range of 10^{-7} - 10^{-6} (see Fig. 6.7a). Moreover, as seen in Fig. 6.8c, the maximum soot particle diameter computed at the PIB exit is found to be D_{SP} =30 nm, whereas for the FF condition the same is 51 nm (Fig. 6.7b). These results suggest that combustion of the C_2H_4-air mixture inside the PIB could reduce the soot volume fraction and particles diameter at the burner exit.

As shown in Figs. 6.8b-f, the $N_D \sim V_0, D_{SP} \sim V_0, X_{C_{10}H_8} \sim V_0$ and $X_{C_{16}H_{10}} \sim V_0$ plots display similar trends to that of $F_V \sim V_0$ curve, that is, for a given φ within their stable filtration velocity limits the curves increase for mixture flame velocities lower than a critical velocity, and at higher filtration velocities they start to fall. These critical filtration velocities, comprehended from Figs. 6.8a-f are termed as V_{0C} in this paper and are reported in Table 6.2. However, this same trend is not observed in Fig. 6.8d for $X_{C_6H_6} \sim V_0$ plot. It can be seen that irrespective of the equivalence ratio the C_6H_6 mole fraction decreases continuously when filtration velocity increases. From Figs. 6.8c and 6.8f it can be observed that D_{SP} and $C_{16}H_{10}$ follow similar trends consistent with that of F_V, yielding the same critical filtration velocities of $V_{0C} \approx$ 0.16 m/s. For $N_D \sim V_0$, the soot number density exhibits the critical filtration velocities at $V_{0C} \approx$ 0.3 m/s corresponding to the

$T_{g,max}$ in the range about ≈ 1895 K – 1950 K, while for $X_{C_{10}H_8} \sim V_0$ curve, the critical filtration velocities is V_{0C} ≈ 0.12 m/s at which the PIB attains peak gas temperatures in the range of around $T_{g,max}$ ≈ 1650 K – 1722 K.

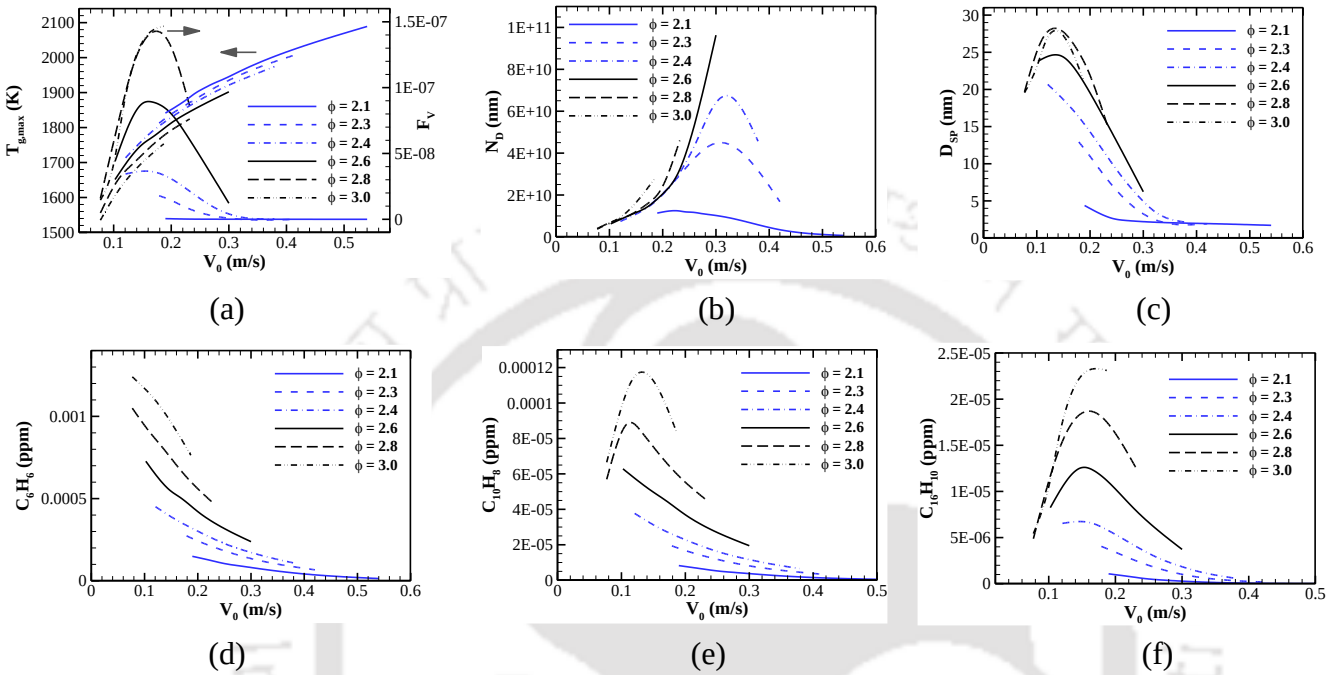

Fig. 6.8. Variations of final **(a)** $T_{g,max}$, F_V, **(b)** N_D, **(c)** D_{SP}, and equilibrium concentrations of **(d)** C_6H_6, **(e)** $C_{10}H_8$, and **(f)** $C_{16}H_{10}$ at the PIB exit as a function of V_0 for different φ.

Table 6.2. Critical filtration velocities (V_{0C}) for $F_V \sim V_0, N_D \sim V_0, D_{SP} \sim V_0$ and $X_k \sim V_0$ curves (Fig. 6.8a-f)

Plot	V_{0C} (m/s)
$F_V \sim V_0$	0.16
$N_D \sim V_0$	0.3
$D_{SP} \sim V_0$	0.16
$X_{C_6H_6} \sim V_0$	-
$X_{C_{10}H_8} \sim V_0$	0.12
$X_{C_{16}H_{10}} \sim V_0$	0.16

6.2.4. Effects of thermo-physical and optical properties on soot production

Performance of the PIB strongly depends on the structural, thermal and optical properties such as burner porosity (ξ), pore diameter (d_p), scattering albedo (ω), extinction coefficient (Γ) and conductivity (λ_s) of the porous matrix. In order to investigate their influence on soot formation behavior, in the following sensitivity analyses of different soot growth related parameters like F_V, N_D, D_{SP}, and X_{PAHs} are performed by perturbing the burner properties. Figs. 6.10a-f show the sensitivities of F_V, N_D, D_{SP} and X_{PAHs} to ten different test cases (Cases: Ia-Vb), as listed in Table 6.3, obtained by perturbing the original PIB properties (base case) independently. In addition, because of the great dependency of the burner temperature distribution on the soot behavior, the gas-phase and solid-phase temperature profiles within the PIB are also reported in Figs. 6.9a-e for the different test cases presented in Table 6.3. From the assessment of Figs. 6.9 and 6.10, it is apparent that, even slight changes in the gas- and solid-phase temperature profiles due to the perturbation of the burner properties results in significant variations in sensitivities of the soot aerosol governing parameters F_V, D_{SP} and $X_{C_{16}H_{10}}$ as illustrated in Figs. 6.10a, 6.10b and 6.10f. Whereas, other parameters such as N_D, $X_{C_6H_6}$ and $X_{C_{10}H_8}$ are mildly sensitive (see Figs. 6.10c-e) to the properties of the PIB.

Table 6.3. Different test cases examined for the sensitivity analyses

Case No.	Burner Properties				
	ω	ξ	λ_s	Γ (m^{-1})	d_p (m)
Base	0.8	0.9	0.1	270	0.00134
Ia	0.5	0.9	0.1	270	0.00134
Ib	0.9	0.9	0.1	270	0.00134
IIa	0.8	0.8	0.1	270	0.00134
IIb	0.8	0.95	0.1	270	0.00134
IIIa	0.8	0.9	0.05	270	0.00134
IIIb	0.8	0.9	0.2	270	0.00134
IVa	0.8	0.9	0.1	135	0.00134
IVb	0.8	0.9	0.1	540	0.00134
Va	0.8	0.9	0.1	270	0.00268
Vb	0.8	0.9	0.1	270	0.00067

To interpret the effect of thermal conductivity (λ_s) of the burner on the soot formation, the reference value (Base Case) of λ_s is increased and decreased by a factor of 2 (Case-IIIa and-IIIb). With the increases of burner conductivity to $2\lambda_s$ (Case-IIIb), the heat recirculation from the post flame region to the pre flame region increases, leading to a decrease in post flame temperature within the PIB than that of the base case (Fig. 6.9c), which subsequently suppresses the soot volume fraction (Fig. 6.10a), reduces the particle size diameter and number density (Fig. 6.10b, c), as well as lower the equilibrium concentrations of C_6H_6, $C_{10}H_8$ and $C_{16}H_{10}$ at the PIB exit (Figs. 6.10 d-f). Similarly, as it is seen, the reduction in thermal conductivity of the PIB enhances the soot formation process. On the contrary, the effect of increased radiative properties like ω and Γ (Case-Ib and-IVb) augments the soot and PAHs generation inside the PIB. This is attributed to the fact that, burner with higher ω and Γ value scatters more radiative energy, and thus by increasing the gas-phase and solid-phase temperatures of the PIB (see Figs. 6.9a,d) it enhances the final F_V, N_D, D_{SP} and X_{PAHs} values, as seen in and Figs 6.10. A similar trend is observed for ξ and d_p.

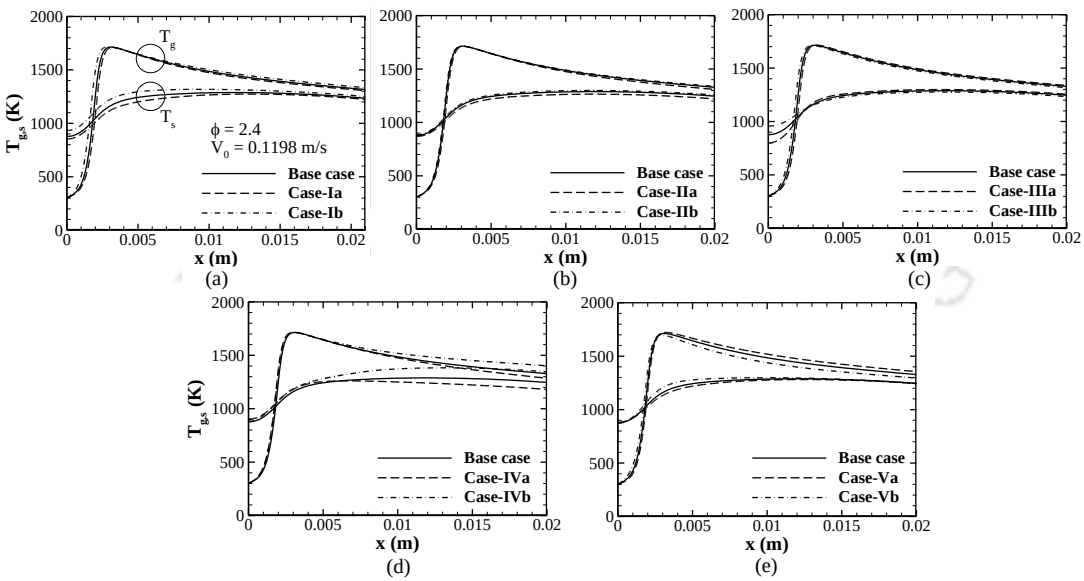

Fig. 6.9. Gas-phase and solid-phase temperature profiles within the PIB for the different test cases presented in Table 6.3.

Any change in d_p affects the convective heat transfer between gas- and solid-phase through the Eq. 2.18, which scales inversely proportional to the h_V. As the d_p reduces (Case-Vb) the volumetric heat transfer between gas- and solid-phase surges, that leads to

an increase in solid-phase temperature profile and a decrease in gas-phase temperature in the post-flame zone of the PIB (Fig. 6.9e), which consequently inhibits the soot growth process resulting lower F_V, N_D, D_{SP} and X_{PAHs} values as compared to the reference base case as shown in Figs. 6.10. Moreover, the PIB with lower porosity matrix (Case-IIa) reduces the soot evolution, due to the lower gas temperature inside the burner caused by the faster heat transfer through conduction and radiation in the solid matrix of the PIB. Thus, on the basis of above discussion, it can be concluded that a PIB with high λ_s, and low ω, Γ, d_p and ξ values should be preferred for reducing the PAHs and soot formation.

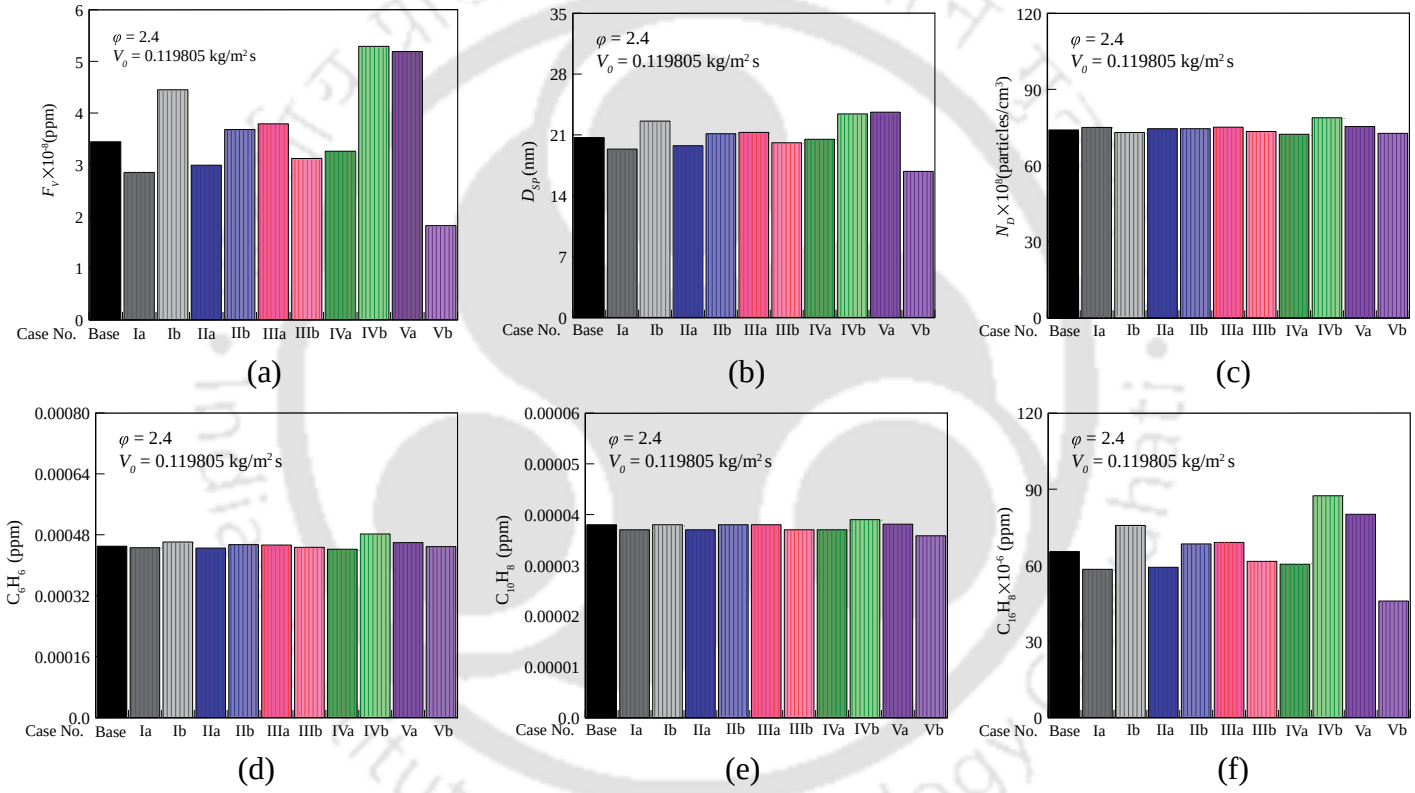

Fig. 6.10. Sensitivity analyses of F_V, N_D, D_{SP} and X_{PAHs} to different test cases for perturbed PIB properties as listed in Table 3.

6.3. Summary

The formation and growth mechanism of soot particles due to the combustion of the ethylene-air mixture within the SiC PIB was investigated numerically. The influence of equivalence ratio, flame speed and temperature of the PIB on soot volume fraction, particle number density, soot particle size and PAHs concentration were studied. To assess the advantage of PMC towards soot suppression, the results for FF combustion

were also compared to that of PIB. Furthermore, the effects of various thermo-physical and optical properties of PIB on the soot growth parameters were investigated. Sensitivity analyses of different thermal and optical properties of the PM indicated that a PIB with low porosity, scattering albedo, extinction coefficient, pore diameter and high thermal conductivity could reduce the PAHs and soot formation. The results from this Chapter showed that PIB not only reduced the CO emission but also could suppress the soot formation and delayed the soot inception process. The present study opens up the possibility to consider the application of PMC to soot-producing thermal devices.

CHAPTER 7

LIQUID FUEL COMBUSTION WITHIN PIB

In practice, combustion of liquid fuels in conventional burners lead to the formation of soot particulates. Based on the results obtained in the previous Chapter, it is clear that PIB is an effective technology for the mitigation of soot formation in a combustor. The aim of the present Chapter is, therefore, to examine the behavior of soot generation due to the combustion of kerosene in a PIB integrated stove. In the previous Chapter, soot evolution in the PIB was studied by integrating DSM based model to the core computational solver described in Chapter 2. In this Chapter, these models are brought together to simulate the combustion characteristics of kerosene in the PIB. The PIB is made up of highly conducting and radiating SiC PM. The PM contributes to the vaporization of the kerosene by radiative heat transfer from the combustion zone to the vaporizer. In the numerical analysis, a 1-D planar model is used assuming complete vaporization of kerosene before its entry to the PIB.

The experimental setup used in this Chapter is same as described in more detail by Mishra et al. [124]. The numerical model is utilized to evaluate the thermal performance of the kerosene-fired PIB. Furthermore, the model provides a comprehensive understanding of the soot and other pollutants formation from the burner that have not previously been widely disseminated. In this study, n-decane ($C_{10}H_{22}$) is used to simulate kerosene combustion within the PIB. The maximum temperature distributions of the gas- and solid-phases of the PM obtained from the numerical analysis with detailed kinetics

mechanisms are validated against the experimentally measured results. Numerical and experimental results are found to have a quite good comparison. In addition, the flammability range, thermal efficiency and CO emissions from the kerosene-fired PIB are investigated for various equivalence ratios. To study the influence of excess enthalpy combustion mode attained in the PIB on the soot evolution process, the variations of soot governing parameters as well as concentration profiles of some important soot precursors are analyzed along the burner axis for different thermal load inputs. The results show that with the incorporation of the PM in the kerosene pressure stove, soot emissions go drastically down.

7.1. Experimental Setup

Figure 7.1 illustrates the PIB-based kerosene stove setup used in the present investigation. It comprises of a SiC PM, vaporizer, needle valve regulator and fuel tank with a hand-operated plunger pump. Initially, kerosene is pressurized in the fuel tank by the hand operated plunger up to a 2 bar pressure and monitored by the pressure gauge mounted over the kerosene tank. Air is supplied to the burner housing from a compressor and monitored by a Coriolis mass flow meter. To achieve the required equivalence ratio, the flow rate of kerosene and air are regulated by needle valves. In order to initiate the vaporization of the liquid fuel, the vaporizer has to be preheated using little oil which burns for 2-3 minutes in the mixing chamber casing below the vaporizer. Then air mixes with the kerosene vapor and the preheated kerosene-air mixture enters the porous burner where the flame is stabilized within the SiC matrix. Once the combustion is stabilized inside the PIB, the vaporization process of kerosene continues because of the radiative heat transfer from the highly radiating SiC medium to the vaporizer, and the combustion mechanism of the kerosene-air mixture is self-sustained inside the PIB without the use of any external heat source for the vaporization.

The temperature distributions inside the PIB were measured using chromel-alumel and *Pt-Pt*/10%*Rh* thermocouples, which were connected to a data acquisition system, as illustrated in Fig. 7.1. One chromel-alumel thermocouple was inserted near the inlet of the burner (T_1) to measure the incoming air-fuel mixture temperature, while two *Pt-Pt*/10%*Rh* thermocouples were located at 1.0 cm intervals along the SiC section (T_2, and T_3) to measure the temperature of the combustion region inside the PIB. It should be

noted that for a given input condition of φ and Q_{th}, the measured temperature of the incoming air-fuel mixture at T_1 location of the burner is used as the boundary condition for the computational model.

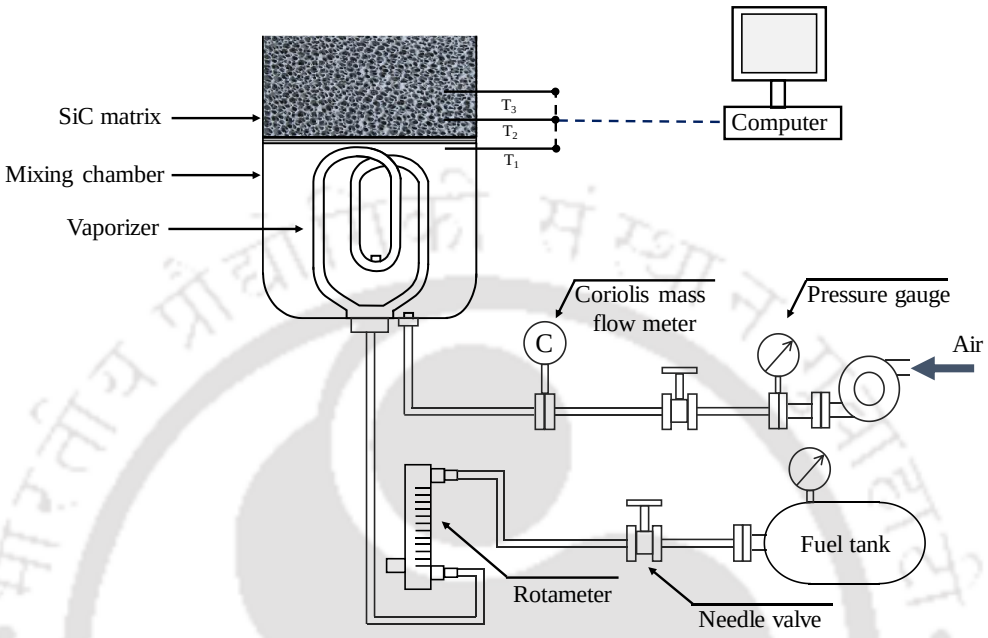

Fig. 7.1. Schematic of the PIBS.

7.2. Results and Discussions

Figure 7.2a reports the experimentally obtained stable flammability ranges of the PIB integrated kerosene stove in terms of input firing rate (kW/m^2) for equivalence ratios in the rage of $\varphi = 0.5-1.8$. For a given equivalence ratio, the stable kerosene-air flame inside the PIB can be obtained when the input firing rate lies within the flammability region, as shown in Fig. 7.2a. Whereas, for a certain equivalence ratio if the firing rate exceeds the flammability zone limit, the kerosene flame will experience blow off. When the PIB is operated at firing rate and equivalence ratio values positioned in the non-flammable region below the flammability zone limit, the flame cannot be self-sustained inside the burner.

The effect of firing rate on the maximum temperature observed inside the PIB is demonstrated in Fig. 7.2b. Here the maximum temperature of the burner measured using the thermocouple is compared to the numerically predicted gas- and solid-phase

temperatures for $\varphi = 0.5$ and $\varphi = 1.8,$ at firing rates corresponding to their respective stability limits. It can be seen that for all the cases, the numerically computed maximum gas-phase temperatures ($T_{g,max}$) agree reasonably good with the experimental measurements. Moreover, for all the examined cases the experiment data lies within the range of predicted maximum gas-phase ($T_{g,max}$) and solid-phase temperatures ($T_{s,max}$). From Fig. 7.2b it is observed that for a given φ both the maximum measured and predicted gas temperatures are more than their respective adiabatic laminar FF temperatures, which ensures that the PIB with kerosene fuel operates in excess enthalpy combustion mode under both fuel-lean $(\varphi = 0.5)$ and fuel-rich conditions $(\varphi = 1.8)$. It is also seen that as expected, for a certain equivalence ratio, with the increase of firing rate the peak temperature of the PIB increases.

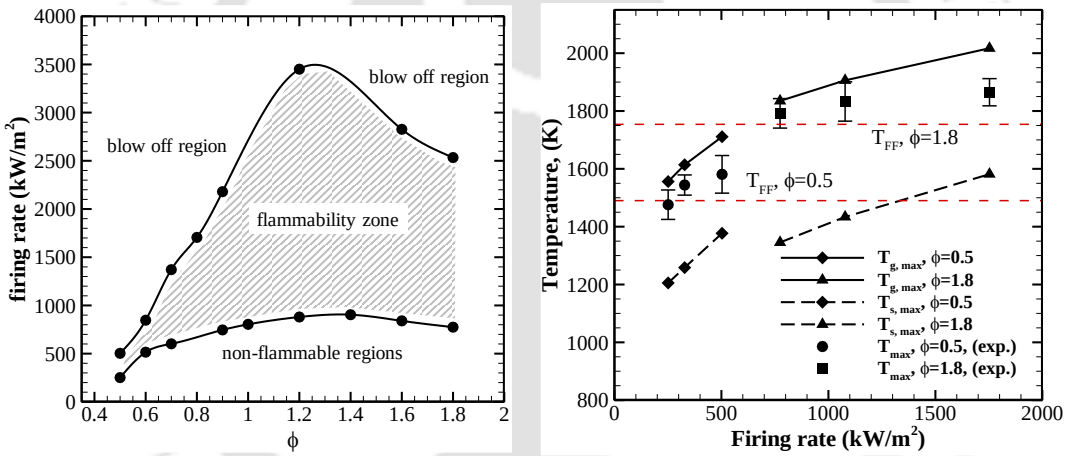

(a) (b)

Fig. 7.2. (a) Stable flammability ranges of the PIB with kerosene fuel, **(b)** comparisons of the maximum temperature measured and computed within the PIB as a function of firing rate.

The influence of input operating conditions on the CO emissions and η_{th} are shown in Figs. 7.3a, b. Both CO emissions and η_{th} results show same trends that were observed with the combustion of gaseous fuels inside the PIB. Nevertheless, in case of kerosene flame, the production of CO pollutant is quite high as compared to the LPG and DME flames inside the PIB (Fig. 5.1a) at the same input conditions. Furthermore, the η_{th} of the PIB with kerosene combustion is found to be lower than that achieved with gaseous fuels combustion (Fig. 5.3b).

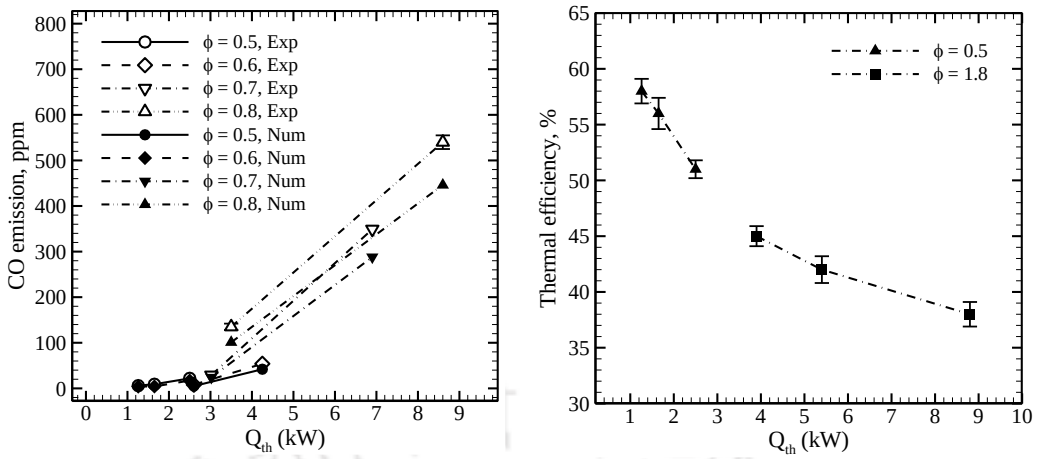

(a) (b)

Fig. 7.3. (a) CO emissions and **(b)** η_{th} of the kerosene-fired PIB for various operating conditions of φ and Q_{th}.

In Fig. 7.4a the numerically predicted axial gas- and solid-phase temperatures of the PIB are presented at input operating condition of $\varphi = 1.8$, and thermal load of Q_{th} = 2.57 kW. Furthermore, the soot evolution in the kerosene flame within the PIB is demonstrated in terms of soot volume fraction, particle diameter, and soot particle density as a function of burner axis. In addition, the FF temperature profiles and the soot growth parameters are also presented at the same equivalence ratio. As shown in Fig. 7.4a, the lower post flame temperature in PIB causes slower growth of soot particle diameter D_{SP} as compared to the FF case. The size of the soot particle formed at the exit of PIB is D_{SP} = 2.9 nm, while for premixed FF condition the computed particle diameter is around D_{SP} = 8 nm under the same φ. In addition, the lower temperature at the downstream section of the SiC PM hinders the soot growth mechanism resulting decrease in particle number density (N_D) and soot volume fraction F_V. This conclusion can be confirmed from Fig. 7.3b where the N_D and F_V profiles as a function of PIB axial distance is compared to the results of FF combustion.

In Fig. 7.5 the influence of the input thermal load on the final soot volume fraction, particle number density and average particle diameter has been investigated at the exit of the PIB under fuel rich condition at $\varphi = 1.8$. As seen in the figure, the D_{SP}, N_D and F_V decrease continuously with increasing thermal load of the burner.

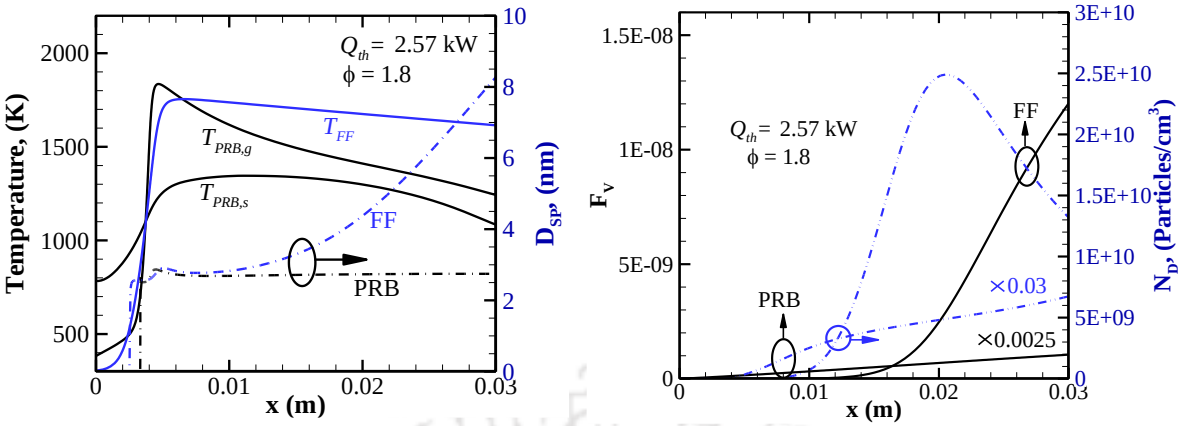

Fig. 7.4. (a) The comparisons of the FF and PIB temperature profiles and soot particle size variations along the burner **(b)** F_V and N_D distribution of the burner at $\varphi = 1.8$, under thermal load of Q_{th} = 2.57 kW.

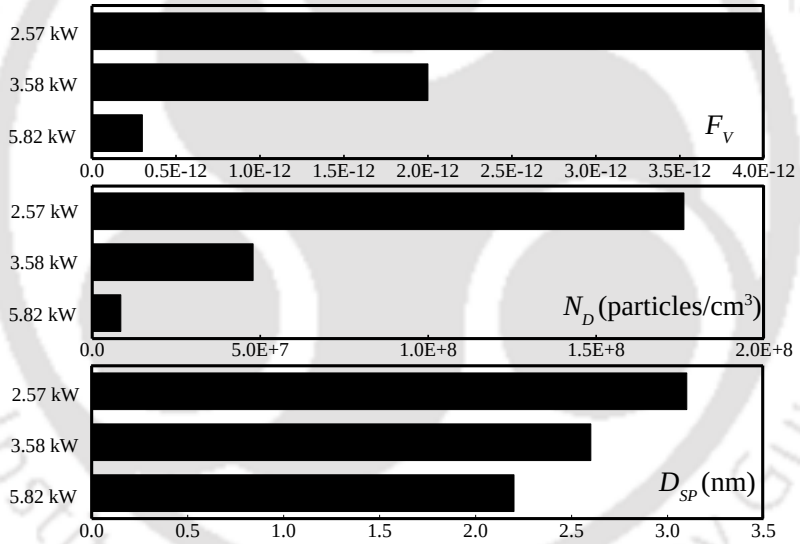

Fig. 7.5. Effects of thermal load inputs on the final D_{SP}, N_D and F_V at the burner exit.

Furthermore, to assess the effects of input thermal load on the major soot precursors in Figs. 7.6a-c the concentration profiles of PAHs (C_6H_6, $C_{10}H_8$, and $C_{16}H_{10}$) have been plotted along the PIB axis at $\varphi = 1.8$. In addition, in Fig. 7.6d the mole fraction distribution of the smallest soot particle BIN5c has been compared to that of FF conditions at various thermal loads. It can be observed from the figures that for all the operating conditions, kerosene flame inside the PIB produces lower amount of PAHs as compared to the FF combustion. Furthermore, it is also worth noting that the peak, as

well as the equilibrium concentration of all the PAHs decreases monotonically with the increase of input thermal load at a constant equivalence ratio.

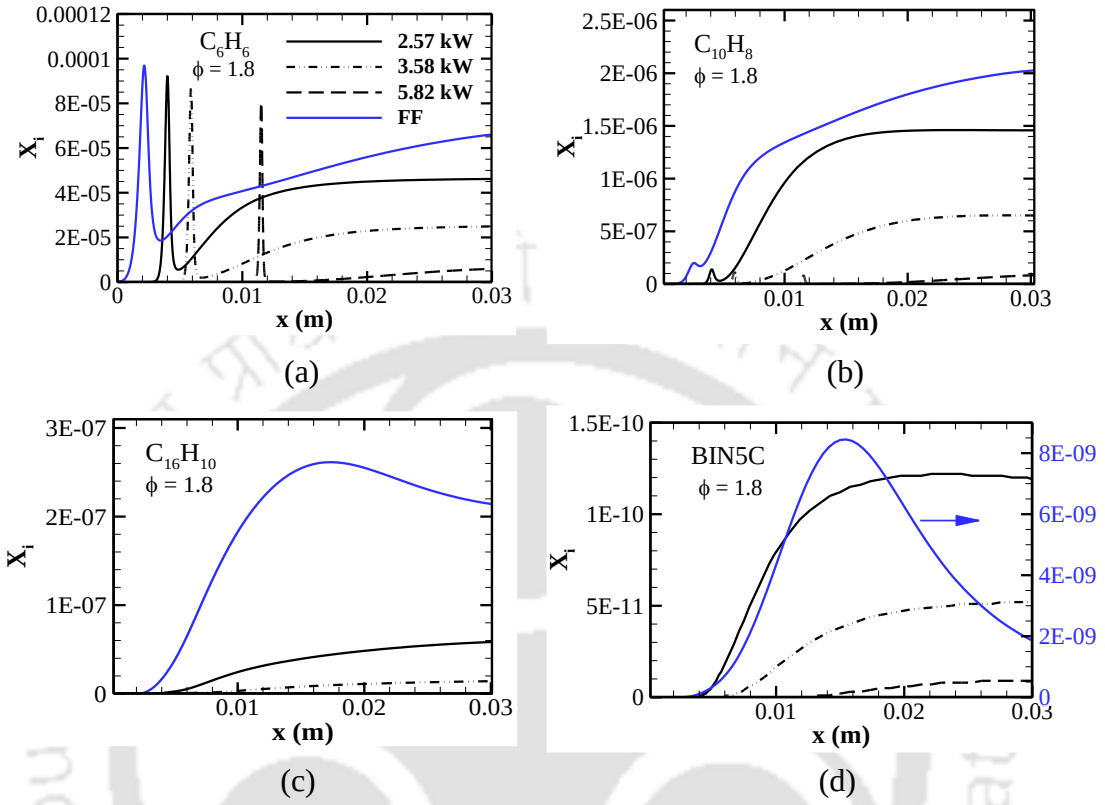

Fig. 7.6. Influence of thermal load inputs on the concentrations of major soot precursors and soot particles at $\varphi = 1.8$.

7.3. Summary

The combustion of kerosene within a PIB integrated pressure stove was investigated. The highly radiating SiC matrix contributed to the vaporization of the kerosene so that self-sustained combustion of the liquid fuel could be attained inside the PIB. The stable flammability ranges of the PIB was reported in terms of input firing rate for equivalence ratios in the rage of $\varphi = 0.5 - 1.8$. The effect of firing rate on the temperature distribution of the PIB was also demonstrated. Furthermore, to assess the advantage of PIB the soot generation due to the combustion of fuel-rich kerosene inside the PIB was investigated. Overall, the results from this study suggested that a reduction in PAHs and soot emissions could be realized from the kerosene stove through the use of PIB.

CHAPTER 8

CONCLUSIONS AND FUTURE SCOPE

The present thesis investigated experimentally and numerically the combustion of LPG, DME as well as kerosene within the PIB under various equivalence ratios and thermal load input conditions. The heat recirculation mechanism instigated by the conduction and radiation feedback in the PM allowed the burner to operate in excess enthalpy combustion condition. In the light of this, an extensive study was performed to assess the applicability of the PIB for the fuel-efficient cooking stoves that produced minimal level of CO and soot emissions. The following summarises the major finding of this research:

The first part of this thesis aimed at developing a numerical solver to predict the combustion of air-fuel mixture inside a single-layer PIB considering detailed chemical kinetics. In particular, the performance of LPG-fueled PIB was evaluated based on comparisons to CH_4 flame inside the PIB as well as to the combustion of LPG in FF mode. LPG combustion in the PIB was found to have a higher operating range than that of CH_4. The LFL of LPG combustion in the PIB was found to be less than that of CH_4 combustion in the PIB, and FF combustion of LPG. Radiant heat flux and the total heat flux were more with LPG combustion in the PIB. For the same equivalence ratio, CO emission of the PIB with LPG was much lower than with its combustion in the FF mode. However, it was higher than that for CH_4 combustion in the PIB.

After the detailed parametric study of the single-layer PIB, the second part of this thesis was devoted to the analyses of combustion characteristics of LPG in a two-layer PIB

using both computational and experimental techniques. Thermal performance of the burner was investigated for various geometric and operating parameters such as equivalence ratio, thermal load, and thickness of the PM. Five different burners (CB1-CB5) with different thicknesses of Al_2O_3 and SiC sections were considered. CO emissions of all the burners operating at $\varphi = 0.4$ or below were found to be lower than 5.0 ppm and were below the emission standard prescribed by WHO. The preheating temperature was increased by 60.7 K using a thicker SiC PM integrated PIB. The LFL was extended to 0.31 with CB3 and CB4 burners. The LFL of $\varphi = 0.37$ was found for the CB1 burner. CO emissions of CB3 and CB4 burners were found to be less than that of CB1 and CB2 burners for all thermal loads. With the use of CB3 burner instead of CB1 burner, an average reduction of 67.7% and 69.6% was achieved in CO emission for $\varphi = 0.6$ and 0.7, respectively. In all cases, CO emissions of CB3 burner and the CB4 burner were nearly identical. To meet the accepted indoor air quality norms, the LPG stove had to be operated below $\varphi = 0.8$. Thickness of the Al_2O_3 section had insignificant effect on CO emissions, preheating temperature and LFL. For $\varphi \le 0.4$, LPG stove with CB1 burner was found to be most effective considering high thermal efficiency and CO emission standard limits permitted by WHO. However, for $\varphi > 0.4$, stove with CB3 burner was found to be more appropriate. The sensitivity of CO emission to the burner ω and λ_s was also studied. Decreasing ω by 50% and increasing λ_s by 10 times of the base value, the CO emissions from the CB3 burner was found to follow the WHO guideline.

One of the objectives of this thesis was to study the effect of DME addition on LPG-air flame inside the PIB. The reaction pathway and flux analyses were performed by using an extended USC-Zhao kinetic mechanism to gain insights into the combustion chemistry of various LPG-DME-air flames within the PIB. The analyses revealed that for all values of φ, combustion of fuel-air mixture inside PIB with higher DME level was found to have a higher filtration velocity than that of pure LPG combustion. Sensitivity analyses of filtration velocity demonstrated that ω and Γ displayed negative sensitivity, whereas ξ and λ_s exhibited positive sensitivity. However, the filtration velocity was found to be insensitive to the density and specific heat capacity of the PIB material. For a fixed input operating condition, with the increase of α, the peak radical pool concentration

increased and the flame location moved to the upstream region of the intersection of the PIB. In addition, the maximum measured and predicted gas temperatures observed in the burner were higher than their respective adiabatic FF temperatures and excess enthalpy combustion was achieved in the PIB. Furthermore, the reaction zone thicknesses of DME flames within PIB were found to be thinner than that of LPG flames.

In the work presented here, the mole fraction profiles, heat release rate and the production rate of dominant reactions responsible for the generation of major chemical species inside the PIB were also investigated for various LPG-DME blends. The results showed that fuel-lean and fuel-rich flames with higher DME fractions generated highest CH_3 and CH_2O radicals within the PIB. For the combustion of LPG inside the PIB, the peak concentrations of soot precursors such as (C_2H_2, C_3H_3, C_6H_6, C_6H_5, C_5H_5 and C_5H_6) were found to be more than their corresponding FF values, however the peak values of these soot precursors and CH_3CHO mole fractions decreased monotonically when DME was added to the LPG-air mixture in the PIB. With $\alpha = 0.5,$ 19.0% reduction in C_2H_2 formation and 21.0% reduction in C_3H_3 formation was achieved as compared to pure LPG combustion. In case of $\alpha = 1.0,$ an order of magnitude decrease in C_2H_2 and C_3H_3 was observed than that of LPG flame. The reactions involving CH_3, HCO and CH_2O were found to be dominant contributors to the overall heat release rate for DME combustion inside the PIB. The flux analyses revealed that for the LPG flame, the C_3H_3 formation pathways through aC_3H_4 and pC_3H_4 species were found to be major contributors in the aromatic ring formation and, with the addition of the DME, these pathways completely vanished.

In the third part of this study, ultra-lean DME flame was used to evaluate the performance of the PIB. From the stand point of higher η_{rad} and lower CO emission, the PIB showed better performance at the ultra-fuel-lean condition, and DME-air mixture with $\varphi = 0.4$ and Q_{th} = 1.4 kW was found to be the most desirable operating condition for the burner. Further analyses highlighted the advantage of the pure DME flame over LPG flame inside the PIB. When DME was used instead of LPG in the PIB integrated stove, the maximum allowable equivalence ratio could be extended from $\varphi = 0.4$ to $\varphi = 0.5,$ and the thermal load from Q_{th} = 4.0 kW to Q_{th} = 5.0 kW, to meet the permitted CO emission limit prescribed by WHO. It was found that with the use of DME instead of LPG, an

average reduction of 47.1% and 27% was achieved in the CO emission for $\varphi = 0.5$ and $\varphi = 0.6,$ respectively. Moreover, for all cases, the radiant efficiency of the PIB with DME flame was found to be higher than the LPG flame.

Another important novelty introduced in the present thesis is to address the soot formation and particle growth process inside the SiC-based PIB. In order to accomplish this purpose, a comprehensive soot kinetic mechanism based upon DSM has been incorporated into the core numerical model, taking into account the radiative heat losses from the gas species and soot particles. It was revealed that the PIB suppressed the soot formation and delayed the manifestation of the soot particulates as compared to the FF case. Moreover, along the PIB axis prominent decline in particle density profile and slower growth of soot particle size were observed. It was shown that the coagulation and agglomeration process of small particles to form large soot aggregates were also depressed by the less prolonged presence of free radicals in the post-flame region of the PIB. When operated under the same input conditions, the computed F_V and D_{SP} values for the PIB ranged from 5×10^{-10} - 3.4×10^{-8} and 2 nm - 22 nm, respectively, while in case of the FF the same were in the range of 10^{-7} - 10^{-6} and 4 nm - 51 nm, respectively. For the PIB the maximum N_D was found to be 8.12×10^{11} particles/cm^3, while for the FF combustion the same was 1.13×10^{11} particles/cm^3. The results showed that the soot particles and the aggregates were evolved at a higher height above the PIB, and they achieved their peak values at the further downstream side of the burner as compared to the FF case.

Sensitivity analyses of various soot-governing parameters revealed that slight changes in gas- and solid-phase temperature profiles due to the perturbation of different thermal and optical properties of the burner resulted in significant variations in sensitivities of F_V, D_{SP} and $X_{C_{16}H_{10}}$, while N_D, $X_{C_6H_6}$ and $X_{C_{10}H_8}$ were found to be mildly sensitive towards the properties of the SiC matrix. It was further demonstrated that a burner with high λ_s, and low ω, Γ, d_p and ξ values should be preferred for the further reduction of PAHs and soot production from the PIB. Eventually, once the numerical model had been developed to interpret the soot evolution phenomenon for PMC, this model was used to demonstrate the soot suppression effect within the kerosene flame inside the PIB.

8.1. Future Scope

The numerical model developed as part of this thesis provides valuable insight in improving the thermal performance of gaseous- and liquid-fuelled PIBs, as well as it permits constructive theoretical guidance for the experimental analysis. Based on the current research, more studies could be conducted in the future for the further improvement of the PIB. The following are the recommendation for the future study:

- In this study, ceramic foam (SiC) and alumina beds have been used as burner materials for the two-layer PIB. To enhance the durability of the burner, a higher resistant material to thermal cycles needs to be explored.
- The present work predicts the suppression effect of soot formation with the use of PMC technique. More research is recommended to confirm this prediction through experimental investigations.
- In the mathematical analysis, the modeling of evaporation mechanism was neglected assuming complete vaporization of the liquid fuel before its entry to the PIB. In this regard, to obtain a close approximation for the combustion of liquid fuels inside the PIB, a complete numerical model including the evaporation process need to be developed.
- Though, the current thesis has mainly focused on the in-depth study of PIB with particular emphasis on lower and medium-scale cooking stoves, the applicability of the PMC can be extended to other relevant domestic as well as industrial purposes.

References

[1] F.J. Weinberg, Combustion temperatures: The future?, Nature 233 (1971) 239-241.

[2] S.B. Sathe, R.E. Peck, T.W. Tong, Flame stabilization and multimode heat transfer in inert porous media: A numerical study, Combust. Sci. Technol. 70 (1990) 93-109.

[3] S.B. Sathe, M.R. Kulkarni, R.E. Peck, T.W. Tong, An experimental and theoretical study of porous radiant burner performance, International Symposium on Combustion 34 (1990) 1011-1018.

[4] T.W. Tong, S.B. Sathe, Heat transfer characteristics of porous radiant burners, J. Heat Transfer 113 (1991) 423-428.

[5] P.-F. Hsu, R.D. Matthews, The necessity of using detailed kinetics in models for premixed combustion within porous media, Combust. Flame 93 (1993) 457-466.

[6] P.-F. Hsu, W.D. Evans, J.R. Howell, Experimental and numerical study of premixed combustion within nonhomogeneous porous ceramics, Combust. Sci. Technol. 90 (1993) 149-172.

[7] X.Y. Zhou, J.C.F. Pereira, Numerical study of combustion and pollutants formation in inert nonhomogeneous porous media, Combust. Sci. Technol. 130 (1997) 335-364.

[8] G. Brenner, K. Pickenäcker, O. Pickenäcker, D. Trimis, K. Wawrzinek, T. Weber, Numerical and experimental investigation of matrix-stabilized methane/air combustion in porous inert media, Combust. Flame 123 (2000) 201-213.

[9] I. Malico, J.F. Pereira, Numerical study on the influence of radiative properties in porous media combustion, J. Heat Transfer 123 (2001) 951-957.

[10] D.J. Diamantis, E. Mastorakos, D.A. Goussis, Simulations of premixed combustion in porous media, Combust. Theor. Model. 6 (2002) 383-411.

[11] P. Talukdar, S.C. Mishra, D. Trimis, F. Durst, Heat transfer characteristics of a porous radiant burner under the influence of a 2-D radiation field, J. Quant. Spectrosc. Radiat. Transfer 84 (2004) 527-537.

[12] S.C. Mishra, M. Steven, S. Nemoda, P. Talukdar, D. Trimis, F. Durst, Heat transfer analysis of a two-dimensional rectangular porous radiant burner, Int. Commun. Heat Mass Transfer 33 (2006) 467-474.

[13] R.M.N. Muhad, M.Z. Abdullah, A. A. Mohamad, M. A. Mujeebu, M. Z. Abu Bakar, R. Zakaria, 3-D Numerical modeling and experimental investigation of a partial premix-type porous medium burner using liquefied petroleum gas fuel, J. Porous Media 13 (2010) 655-669.

[14] J.-R. Shi, M.-Z. Xie, H. Liu, G. Li, L. Zhou, Numerical simulation and theoretical analysis of premixed low-velocity filtration combustion, Int. J. Heat Mass Transfer 51 (2008) 1818-1829.

[15] K. Hanamura, R. Echigo S.A. Zhdanok, Superadiabatic combustion in a porous medium, Int. J. Heat Mass Transfer 36 (1993) 3201-3209.

[16] N.O. Moraga, C.E. Rosas, V.I. Bubnovich, N.A. Solari, On predicting two-dimensional heat transfer in a cylindrical porous media combustor, Int. J. Heat Mass Transfer 51 (2008) 302-311.

[17] F.M. Pereira, A. Oliveira, F. Fachini, Maximum superadiabatic temperature for stabilized flames within porous inert media, Combust. Flame 158 (2011) 2283-2288.

[18] T.K. Kayal, M. Chakravarty, Combustion of liquid fuel inside inert porous media: an analytical approach, Int. J. Heat Mass Transfer, 48 (2005) 331-339.

[19] S. Voss, M.A.A. Mendes, J.M.C. Pereira, S. Ray, J.C.F. Pereira, D. Trimis, Investigation on the thermal flame thickness for lean premixed combustion of low calorific H2/CO mixtures within porous inert media, Proc. Combust. Inst. 34 (2013) 3335-3342.

[20] N. Djordjevic, P. Habisreuther, N. Zarzalis, Porous burner for application in stationary gas turbines: an experimental investigation of the flame stability, Emissions and temperature boundary condition, Flow Turbulence Combust. 89 (2012) 261-274.

[21] V.K. Pantangi, S.C. Mishra, P. Muthukumar, R. Reddy, Studies on porous radiant burners for LPG (liquefied petroleum gas) cooking applications, Energy 36 (2011) 6074-6080.

[22] R.S. Dhamrat, J.L. Ellzey, Numerical and experimental study of the conversion of methane to hydrogen in a porous media reactor, Combust. Flame 144 (2006) 698-709.

[23] S.G. Kim, T. Yokomori, N.I. Kim, S. Kumar, S. Maruyama, K. Maruta, Flame behavior in heated porous sand bed, Proc. Combust. Inst. 31 (2007) 2117-2124.

[24] A. Loukou, I. Frenzel, J. Klein, D. Trimis, Experimental study of hydrogen production and soot particulate matter emissions from methane rich-combustion in inert porous media, Int. J. Hydrogen Energy 37 (2010) 16686-16696.

[25] D. Trimis, F. Durst, Combustion in a porous medium – advances and applications, Combust. Sci. Technol. 121 (1996) 153-168.

[26] J.R. Howell, M.J. Hall, J.L. Ellzey, Combustion of hydrocarbon fuels within porous inert media, Prog. Energy Combust. Sci. 122 (1996) 121-145.

[27] V.K. Pantangi, S.C. Mishra, Combustion of gaseous hydrocarbon fuels within porous media – a review, Advances in Energy Research 8 (2006) 455-461.

[28] M.M. Kamal, A.A. Mohamad, Combustion in porous media, Int. J. Power Energy Syst. 220 (2006) 487-508.

[29] S. Wood, A.T. Harris, Porous burners for lean-burn applications, Prog. Energy Combust. Sci. 34 (2008) 667-684.

[30] M.A. Mujeebu, M.Z. Abdullah, A.A. Mohamad, M.Z. Abu Bakar, Trends in modeling of porous media combustion, Prog. Energy Combust. Sci. 36 (2010)

627-650.

[31] M.A. Mujeebu, M.Z. Abdullah, A.A. Mohamad, Development of energy efficient porous medium burners on surface and submerged combustion modes, Energy 36 (2011) 5132-5139.

[32] B. Yu, S-M. Kum, C-E. Lee, S. Lee, Combustion characteristics and thermal efficiency for premixed porous-media types of burners, Energy 53 (2013) 343-350.

[33] C. Keramiotis, B. Stelzner, D. Trimis, M. Founti, Porous burners for low emission combustion: An experimental investigation, Energy 45 (2012) 213-219.

[34] M.D. Robayo, B. Beaman, B. Hughes, B. Delose, N. Orlovskaya, R-H. Chen, Perovskite catalysts enhanced combustion on porous media, Energy 76 (2014) 477-486.

[35] D.M. Sowards, High intensity radiant gas burner, United States Patent 3751213 (1973).

[36] K. Hanamura, K. Bohda, Y. Miyairi, A study of super-adiabatic combustion engine, Energy Convers. Manage 38 (1997) 1259-1266.

[37] C.W. Park, M. Kaviany, Evaporation–combustion affected by in-cylinder, reciprocating porous regenerator, J. Heat Transfer 124 (2002) 184-194.

[38] F. Durst, M. Weclas, A new type of internal combustion engine based on the porous-medium combustion technique, Proceedings of the Institution of Mechanical Engineers, Part D: Journal of Automobile 215 (2001) 63-81.

[39] N. Delalic, D. Mulahasanovic, E.N. Ganic, Porous media compact heat exchanger unit – experiment and analysis, Exp. Therm Fluid Sci. 28 (2004) 185-192.

[40] L. Malico, X.Y. Zhou, J.C.F. Pereira, Two-dimensional numerical study of combustion and pollutants formation in porous burners, Combust. Sci. Technol. 152 (2000) 57-79.

[41] E. Noordally, J.M. Przybylski, J.J. Witton, Porous media combustors for clean gas turbine engines. Technical report, Cranfield University (2004) United Kingdom.

[42] K. Hanamura, R. Echigo, An analysis of flame stabilization mechanism in radiation burners, Wärme-und Stoffübertragung 26 (1991) 377-383.

[43] M. Bidi, M.R.H. Nobari, M. Saffar Avval, A numerical evaluation of combustion in porous media by EGM (Entropy Generation Minimization), Energy 35 (2010) 3483-3500.

[44] A.C. Ratzel, J.R. Howell, Two-dimensional radiation in absorbing-emitting media using the P-N approximation, J. Heat Transfer 105 (1983) 333-340.

[45] J.C. Chai, H.S. Lee, S. Patankar, Finite volume method for radiation heat transfer, J. Thermophys Heat Transfer 8 (1994) 419-425.

[46] T.J. Hendricks, J.R. Howell, Absorption/Scattering coefficients and scattering phase function in reticulated porous ceramics, J. Heat Transfer 118 (1996) 79-87.

[47] R. Mital, J.P. Gore, R. Viskanta, A study of the structure of submerged reaction in porous ceramic radiant burners, Combust. Flame 11 (1997) 175-184.

[48] V. Khanna, R. Goel, J.L. Ellzey, Measurements of emissions and radiation for methane combustion within a porous medium burner, Combust. Sci. Technol 99 (1994) 133-142.

[49] T-Y. Xiong, J.K. Mark, F. F. Ferol, Experimental study of a high-efficiency, low emission porous matrix combustor-heater, Fuel 74 (1995) 1641-1647.

[50] G. Scribano, G. Solero, A. Coghe, Pollutant emissions reduction and performance optimization of an industrial radiant tube burner, Exp. Therm Fluid Sci 30 (2006) 605-612.

[51] S. Jugjai, N. Rungsimuntuchart, High efficiency heat-recirculating domestic gas burners, Exp. Therm Fluid Sci. 26 (2002) 581-592.

[52] P. Muthukumar, P. Shyamkumar, Development of novel porous radiant burners for LPG cooking applications, Fuel 112 (2013) 562-566.

[53] Z. Dongbin, L. Jinsheng, L. Guangchuan, D. Yan, X. Gang, L. Lihua, Effects on combustion of liquefied petroleum gas of porous ceramic doped with rare earth elements, J. Rare Earths 25 (2007) 212-225.

[54] Mortality from household air pollution 2012 - summary of results, World Health Organization,(2014) http://www.who.int/phe/health_topics/outdoorair/databases.

[55] R. Junus, J.F. Stubington, G.D. Sergeamt, The effects of design factors on emissions from natural gas cooktop burners, Int. J. Environ. Stud, 45 (1994) 101-121.

[56] J.F. Stubington, G. Reashel, T. Murphy, R. Junus, P.J. Ashman, G.D. Sergeamt, Emissions and efficiency from production cooktop burners firing natural gas, J Inst Energy 67 (1994) 143-155.

[57] S.S. Hou, Y.C. Ko, Influence of oblique angle and heating height on flame structure, temperature field and efficiency of an impinging laminar jet flame, Energy Convers. Manage. 46(6) (2005) 941-958.

[58] S.S. Hou, Y.C. Ko, Effects of heating height on flame appearance, temperature field and efficiency of an impinging laminar jet flame used in domestic gas stoves, Energy Convers. Manage. 45(9-10) (2004) 1583-1595.

[59] V.K. Pantangi, A.S.S.R.K. Kumar, S.C. Mishra, N. Sahoo, Performance analysis of domestic LPG cooking stoves with porous media, International Energy Journal 8 (2007) 139-144.

[60] M. Sharma, P. Mahanta, S.C. Mishra, Usability of porous burner in kerosene pressure stove: An experimental investigation aided by energy and exergy analyses, Energy 103 (2016) 251-260.

[61] K.H. Song, P. Nag, T.A. Litzinger, D.C. Haworth, Effects of oxygenated additives on aromatic species in fuel-rich, premixed ethane combustion: a

modeling study, Combust. Flame 135 (2003) 341-349.

[62] S.S. Yoon, D.H. Anh, S.H. Chung, Synergistic effect of mixing dimethyl ether with methane, ethane, propane, and ethylene fuels on polycyclic aromatic hydrocarbon and soot formation, Combust. Flame 154 (2008) 368-377.

[63] W. Ying, L. Genbao, Z. Wei, Z. Longbao, Study on the application of DME/diesel blends in a diesel engine, Fuel Process. Technol. 89 (2008) 1272-1280.

[64] S. Lee, S. Oh, Y. Choi, K. Kang, Performance and emission characteristics of a CI engine operated with n-Butane blended DME fuel, Appl. Therm. Eng. 31 (2011) 1929-1935.

[65] I. Gökalp, E. Lebas, Alternative fuels for industrial gas turbines (AFTUR), Appl. Therm. Eng. 24 (2004) 1655-1663.

[66] M.C. Lee, S.B. Seo, J.H. Chung, Y.J. Joo, D.H. Ahn, Industrial gas turbine combustion performance test of DME to use as an alternative fuel for power generation, Fuel 88 (2009) 657-662.

[67] M. Marchionna, R. Patrini, D. Sanfilippo, G. Migliavacca, Fundamental investigations on di-methyl ether (DME) as LPG substitute or make-up for domestic uses, Fuel Process. Technol. 89 (2008) 1255–1261.

[68] P. K. Arya, S. Tupkari, K. Satish, G.D. Thakre, B.M. Shukla, DME blended LPG as a cooking fuel option for Indian household: A review, Renewable Sustainable Energy Rev. 53 (2016) 1591-1601.

[69] R. Anggarani, C.S. Wibowo, D. Rulianto, Application of dimethyl ether as LPG substitution for household stove, Energy Procedia 47 (2014) 227-234.

[70] T.H. Fleisch, A. Basu, R.A. Sills, Introduction and advancement of a new clean global fuel: The status of DME developments in China and beyond, J. Nat. Gas Sci. Eng. 9 (2012) 94-107.

[71] T.G. Benish, A.L. Lafleur, K. Taghizadeh, J.B. Howard, C_2H_2 and PAH as soot

growth reactants in premixed C_2H_4-air flames, Proc. Combust. Inst. 26 (1996) 2319-2326.

[72] M. Bonig, C. Feldermann, H. Jander, B. Luers, G. Rudolph, H.G. Wagner, Soot formation in premixed C_2H_4 flat flames at elevated pressure, Proc. Combust. Inst. 23 (1990) 1581-1587.

[73] F. Mauss, T. Schaafer, H. Bockhorn, Inception and growth of soot particles in dependence on the surrounding gas phase, Combust. Flame 99 (1994) 697-705.

[74] A. Ciajolo, A. D'Anna, R. Barbella, A. Tregrossi, A. Violi, The effect of temperature on soot inception in premixed ethylene flames, Proc. Combust. Inst 26 (1996) 2327-2333.

[75] H. Böhm, D. Hesse, H. Jander, B. Luers, J. Pietscher, H.G.G. Wagner et al, The influence of pressure and temperature on soot formation in premixed flames, Proc. Combust. Inst. 22 (1988) 403-411.

[76] C. Saji, C. Balaji, T. Sundararajan, Investigation of soot transport and radiative heat transfer in an ethylene jet diffusion flame, Int. J. Heat Mass Transfer 51 (2008) 4287-4299.

[77] H. Guo, G. Smallwood, The interaction between soot and NO formation in a laminar axisymmetric coflow ethylene/air diffusion flame, Combust. Flame 149 (2007) 225-233.

[78] B. Zamuner, F. Dupoirieux, Numerical simulation of soot formation in a turbulent flame with a Monte-Carlo PDF approach and detailed chemistry, Combust. Sci. Technol. 158 (2000) 407-438.

[79] H. El-Asrag, T. Lu, C. Law, S. Menon, Simulation of soot formation in turbulent premixed flames, Combust. Flame 150 (2007) 108-126.

[80] M.D. Domenico, P. Gerlinger, M. Aigner, Development and validation of a new soot formation model for gas turbine combustor simulations, Combust. Flame 157 (2010) 246-258.

[81] F.E. Kruis, J.Wei, T.V.D. Zwaag, S. Haep, Computational fluid dynamics based stochastic aerosol modeling: combination of a cell-based weighted random walk method and a constant-number Monte-Carlo method for aerosol dynamics, Chem. Eng. Sci. 70 (2012) 109-120.

[82] E. Debry, B. Sportisse, B. Jourdain, A stochastic approach for the numerical simulation of the general dynamics equation for aerosols, J. Comput. Phys. 184 (2003) 649-669.

[83] A. D'Anna, J.H. Kent, A model of particulate and species formation applied to laminar, nonpremixed flames for three aliphatic-hydrocarbon fuels, Combust. Flame 152 (2008) 573-587.

[84] H. Richter, S. Granata, W.H. Green, J.B. Howard, Detailed modeling of PAH and soot formation in a laminar premixed benzene/oxygen/argon low-pressure flame, Proc. Combust. Inst. 30 (2005) 1397-1405.

[85] S.B. Dworkin, Q. Zhang, M.J. Thomson, N.A. Slavinskaya, U. Riedel, Application of an enhanced PAH growth model to soot formation in a laminar coflow ethylene/air diffusion flame, Combust. Flame. 158 (2011) 1682-1695.

[86] S.C. Mishra, M.Y. Kim, S. Maruyama, Performance evaluation of four radiative transfer methods in solving multi-dimensional radiation and/or conduction heat transfer problems, Int. J. Heat Mass Transfer 55 (2012) 5819-5835.

[87] X. Fu, R. Viskanta, J.P. Gore, Measurement of volumetric heat transfer coefficient of cellular ceramics, Exp. Therm Fluid Sci. 17 (1998) 285-293.

[88] D. Goodwin, N. Malaya, H. Moffat, R. Speth, Cantera: An object-oriented software toolkit for chemical kinetics, thermodynamics, and transport processes. Version 2.1, available at https://code.google.com/p/cantera/.

[89] R.J. Kee, M.E. Coltrin, P. Glarborg, Chemically reacting flow: theory & practice. John Wiley & Sons (2005).

[90] C.T. Bowman, R.K. Hanson, D.F. Davidson, W.C. Gardiner, V. Lissianski, G.P. Smith et al., GRI 2.11 Detailed Mechanism, http://www.me.berkeley.edu/gri

mech/, Berkeley, CA, USA (1996).

[91] H. Wang, X. You, A.V. Joshi, S.G. Davis, A. Laskin, F. Egolfopoulos et al., USC Mech Version II. High-Temperature Combustion Reaction Model of H2/CO/C1-C4 Compounds. http://ignis.usc.edu/USC_Mech_II.htm.

[92] P.F. Hsu, J.R. Howell, R.D. Matthews, A numerical investigation of premixed combustion within porous inert media, J. Heat Transfer 115(3) (1993) 744-750.

[93] N. Wakao, S. Kaguei, Heat and mass transfer in packed beds, London: Gordon and Breach Science Publisher, (1982).

[94] M. Fay, R. Dhamrat, J.L. Ellzey, Effect of porous reactor design on conversion of methane to hydrogen, Combust. Sci. Technol. 177 (2005) 2171-2189.

[95] P.F. Hsu, J.R. Howell, Measurements of thermal conductivity and optical properties of porous partially stabilized zirconia, Exp. Heat Transfer 5 (1992) 293-313.

[96] World Health Organization. WHO guidelines for indoor air quality: Selected pollutants. Geneva, Switzerland World Health Organization; (2010).

[97] Z. Zhao, A. Kazakov, F.L. Dryer, Measurements of dimethyl ether/air mixture burning velocities by using particle image velocimetry, Combust. Flame 139 (2004) 52-60.

[98] A. Frassoldati, T. Faravelli, E. Ranzi, K. Kohse-Höinghaus, P.R. Westmoreland, Kinetic modeling study of ethanol and dimethyl ether addition to premixed low-pressure propene–oxygen–argon flames, Combust. Flame 158 (2011) 1264-1276.

[99] W.B. Lowry, Z. Serinyel, M.C. Krejci, H.J. Curran, G. Bourque, E.L. Petersen, Effect of methane-dimethyl ether fuel blends on flame stability, laminar flame speed, and Markstein length, Proc. Combust. Inst. 33 (2011) 929-937.

[100] B.A.V. Bennett, C.S. McEnally, L.D. Pfefferle, M.D. Smooke, M.B. Colket, Computational and experimental study of the effects of adding dimethyl ether

and ethanol to nonpremixed ethylene/air flames, Combust. Flame 156 (2009) 1289-1302.

[101] S. Ravi, E.L. Petersen, Laminar flame speed correlations for pure-hydrogen and high-hydrogen content syngas blends with various diluents, Int. J. Hydrogen Energy 37 (2012) 19177-19189.

[102] T. Bekat, F. Inal, Effects of dimethyl ether on n-butane oxidation, Fuel 115 (2014) 861-869.

[103] H. Wu, E. Hu, H. Yu, Q. Li, Z. Zhang, Y. Chen et al., Experimental and numerical study on the laminar flame speed of n-butane/dimethyl ether-air mixtures, Energy Fuels 28 (2014) 3412-3419.

[104] C.A. Frye, A.L. Boehman, P.J.A. Tjim, Comparison of CO and NO emissions from propane, n-butane, and dimethyl ether premixed flames, Energy Fuel 13 (1999) 650-654.

[105] W.K. Metcalfe, S.M. Burke, S.S. Ahmed, H.J. Curran, A hierarchical and comparative kinetic modeling study of C_1-C_2 hydrocarbon and oxygenated fuels, Int. J. Chem. Kinet. 45 (2013) 638-675.

[106] Z. Zhao, M. Chaos, A. Kazakov, F.L. Dryer, Thermal decomposition reaction and a comprehensive kinetic model of dimethyl ether, Int. J. Chem. Kinet. 40 (2008) 1-18.

[107] M. Akram, S. Kumar, P. Saxena, Experimental and computational determination of laminar burning velocity of liquefied petroleum gas-air mixtures at elevated temperatures, J. Eng. Gas Turbines Power 135 (2013) 091501-1.

[108] R.J. Varghese, V.R. Kishore, M. Akram, Y. Yoon, S. Kumar, Burning velocities of DME (dimethyl ether)-air premixed flames at elevated temperatures, Energy 126 (2017) 34-41.

[109] S.J. Kline, F.A. McClintock, Describing uncertainties in single-sample experiments, Mechanical Engineering 75 (1953) 3-8.

[110] H. Richter, J.B. Howard, Formation of polycyclic aromatic hydrocarbons and their growth to soot-a review of chemical reaction pathways, Prog Energy Combust Sci. 26 (2000) 565-608.

[111] C. Arcoumanis, C. Bae, R. Crookes, E. Kinoshita, The potential of di-methyl ether (DME) as an alternative fuel for compression-ignition engines: A review, Fuel 87 (2008) 1014-1030.

[112] C. Zheng, L. Cheng, J.P. Bingue, A. Saveliev, K. Cen, Partial oxidation of methane in porous reactor: Part I. Unidirectional flow, Energy Fuels 26 (2012) 4849-4856.

[113] M. Toledo, K. Utria, A.V. Saveliev, Ultrarich filtration combustion of ethane, Energy Fuels 28 (2014) 1536-1540.

[114] T. Carvalho, M. Costa, C. Casaca, R.C. Catapan, A.A.M. Oliveira, Destruction of the tar present in syngas by combustion in porous media, Energy Fuels 29 (2015), 1130-1136.

[115] K. Araus, F. Reyes, M. Toledo, Syngas production from wood pellet using filtration combustion of lean natural gas–air mixtures, Int J Hydrogen Energy 39 (2014) 7819-7825.

[116] H. Pedersen-Mjaanes, L. Chan, E. Mastorakos, Hydrogen production from rich combustion in porous media, Int J Hydrogen Energy 30 (2005), 579-592.

[117] E.L. Belmont, S.M. Solomon, J.L. Ellzey, Syngas production from heptane in a non-catalytic counter-flow reactor, Combust Flame 159 (2012) 3624-3631.

[118] Y. Liu, B. Rogg, Modelling of thermally radiating diffusion flames with detailed chemistry and transport, EUROTHERM Seminars 17 (1991) 114-127.

[119] B. Franzelli, A. Cuoci, A. Stagni, M. Ihme, T. Faravelli, S. Candel, Numerical investigation of soot-flame-vortex interaction, Proc. Combust. Inst. 36 (2017) 753-761.

[120] E. Ranzi, A. Frassoldati, R. Grana, A. Cuoci, T. Faravelli, A.P. Kelleyet et al.,

Hierarchical and comparative kinetic modeling of laminar flame speeds of hydrocarbon and oxygenated fuels, Prog. Energy Comb. Sci. 38 (2012) 468-501.

[121] C. Saggese, S. Ferrario, J. Camacho, A. Cuoci, A. Frassoldati, E. Ranzi et al., Kinetic modeling of particle size distribution of soot in a premixed burner-stabilized stagnation ethylene flame, Combust. Flame 162 (2015) 3356-3369.

[122] Cosilab Documentation, 1D premixed flames and counterflow diffusion flames, Section B.1. (2017).

[123] G.L. Hubbard, C.L. Tien, Infrared mean absorption coefficients of luminous flames and smoke, J. Heat Transfer 100 (1978) 235-239.

[124] S.C. Mishra, P. Muthukumar, G.S. Sinha, M. Sharma, N.K. Mishra, Self aspirated pressurized kerosene cooking stove with a porous radiant burner, Indian Patent 201631037245 (2016).

APPENDIX A

Uncertainty and Error Analyses

The experimental measurement uncertainties were assessed using the root sum square method of Klein and McClintock [109]. The uncertainties in mass flow rates of DME, LPG, kerosene, and air were 0.001 g/s, 0.001 g/s, 0.02 g/s and 0.015 g/s respectively. The total uncertainty of input power load (Q_{th}) and equivalence ratio were estimated from,

$$E_{Q_{th}} = \left[\left(\frac{\partial FR}{\partial m_f} \partial m_f \right)^2 + \left(\frac{\partial FR}{\partial A_c} \partial A_c \right)^2 \right]^{1/2} \frac{1}{Q_{th}}$$

$$E_{\varphi} = \left[\left(\frac{\partial \varphi}{\partial m_f} \partial m_f \right)^2 + \left(\frac{\partial \varphi}{\partial m_{air}} \partial m_{air} \right)^2 \right]^{1/2} \frac{1}{\varphi}$$

where ∂m_f, ∂m_{air}, and ∂A_c are the uncertainty of the mass flow rates of fuel, mass flow rates of air and cross-sectional area of the PIB respectively. In the present experiments, the maximum uncertainties for firing rate and equivalence ratio were found to be ± 1.45% and ±1.1% respectively. The experimental uncertainty of the thermocouple is about ± 1%, while flue gas analyzer has an uncertainty of about ± 5% for CO emission measurement according to the manufacturer. The uncertainty in the estimation of thermal efficiency was found to be ± 1.3%. Moreover, the thermocouple measurements were corrected for errors caused by convective and radiation heat losses from the thermocouple junction. The difference between measured and corrected value of temperature was estimated to be less than 9% of the measured value. Furthermore, the standard error in the CO emission and temperature measurements analyses remained below ± 11% and ± 4% respectively.

APPENDIX B

Grid Independent Test

In this study, adaptive mesh strategy is used to create a grid independent and accurate numerical solution. With the effect of number of grid points (obtained by varying the grid refinement criterion) on the axial gas temperature profiles of the PIB is shown in the following figure. In this work the grid refinement parameters are set to; ratio = 2, slope = 0.05 and curve = 0.1 (refinement criterion correspond to grid number (x_p) = 530) to obtain mesh independent solution.

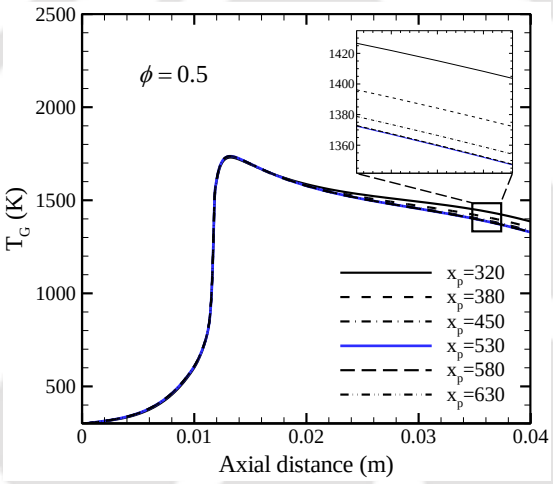

Grid-independent test for temperature profile inside the porous burner.

In addition, the grid-independent test for CO emissions from the porous burner at $\varphi = 0.5$ and $Q_{th} = 5\,\text{kW}$ is reported in the following table. It shows that no significant change in CO emission is observed due to the change of grid numbers.

Grid-independent test for CO emissions at $\varphi = 0.5$ and $Q_{th} = 5\,\text{kW}$

Grid numbers (x_p)	CO emission
320	4.68
380	4.73
450	4.92
530	5.09
580	5.1
630	5.12

APPENDIX C

Technical Specifications of the Instruments Used in the Experiments

1. Digital pressure gauges:

P1		**P2**	
Make	: DWYER (U.S.A.)	Make	: DWYER (U.S.A.)
Fluid	: LPG, DME	Fluid	: Air
Models	: DPG-003	Models	: DPG-006
Range	: 0-2 bar	Range	: 0-13.8 bar
Accuracy	: ±0.05% full scale	Accuracy	: ±0.05% full scale
Pressure Limit	: 2 x FS range	Pressure Limit	: 2 x FS range
Temperature Limits	: -18 to 66°C	Temperature Limits	: -18 to 66°C
Power requirements	: 3 AAA batteries.	Power requirements	: 3 AAA batteries.

2. Pressure regulator

Make	: SKN Pvt. Ltd.
Maximum pressure	: 2 bar gauge
Temperature Limits	: -20°C to 50°C

3. Compressor

Make	: Ingersoll Rand
Type	: Reciprocating
Maximum Pressure	: 12 kg/cm^2
Free air delivery	: 400-450 lpm
Type	: 2 stage
Tank capacity	: 250 liters

4. Pressure regulator (Compressed air)

Make	: Norgren
Model	: R73G-2GK-RMN
Fluid	: Compressed air
Maximum pressure	: 10 bar

5. Weighing balance (WB)

Make	: SARTORIUS COMBICS LITE
Model	: CLWP1 – 30ED-I
Capacity	: 30kg
Platform size	: 400X300mm
Readability	: 1g
Power Supply	: 90 to 260V AC & DC
Indicator	:18mm LCD 7 segment backlit

6. Mass flow meter

Type	: Coriolis mass flow meter
Make	: Emerson Process Management Pvt. Ltd.
Model	: CMF010P323NQB2E222
Flow range	: 0 to 50 g/min
Flow accuracy	: ± 0.35% of full scale
Sensitivity	: 0.001g
Temperature range	: -10 to 100 °C
Operating pressure range	: 0 to 150 bar

7. Rotameter

Make	**:**	Flow tech engineers
Operating fluid	**:**	Kerosene
Pressure	**:**	Atmospheric
Measuring range	**:**	0-10 mlpm
Least count	**:**	0.2 mlpm
Accuracy	**:**	±3% FS

8. Portable gas analyser

Make	: GreenLine
Model	: 8000
O_2	: 0 – 25 Vol%
Resolution	: 0.1 Vol%
Accuracy	: <0.1 Vol%
CO	: 0 – 20000 ppm
Accuracy	: <10 ppm (0 – 300 ppm)
Resolution	: 1 ppm

9. Data acquisition unit (DAQ)

Make	: Agilent Technologies
Model	: 34970A
Scan rate	: 60 to 250 channels/second
Scan intervals	: 0 to 99 hours; 1 ms time step
Accuracy	: 6 digits of resolution with 0.004%

10. IR camera

Make	: InfraTec
Spectral range	: (7.5 – 14) μm
Temperature measuring range	: (-40 – 1,200) °C, optional > 2,000 °C

Temperature resolution at 30 °C	: better than 0.05 K, up to 0.03 K
Measurement accuracy	: ± 1.5 K (0 - 100) °C; ± 2 % (< 0 and > 100) °C
Emissivity	: Adjustable from 0.1 to 1.0
IR frame rate	: 50/60 Hz
Zoom function	: Up to 8 times digital, infinitely variable
Power supply	: mains adapter, FireWire (IEEE 1394)
Operation temperature	: (-15 - 50) °C
Dimensions (complete system)	: (133 x 106 x 110) mm
Weight (complete system)	: approx. 1.3 kg